Coalescence times and gravitational wave signals of supermassive black holes in cosmological galaxy mergers.

CAS PIFI
2021 July -2022 March

11 referred + 2 in progress
(2021 – 2022):
MNRAS – 8; A&A – 4; ApJ – 1
~100 citations…

Dr. Sci. Peter Berczik

MAO, National Academy of Sciences of Ukraine, Kiev

2022 May 26.

Already Published Papers with NAOC first affiliation under my current PIFI:

1) Khoperskov, S., Zinchenko, I., Avramov, B., Khrapov, S., Berczik, P., Saburova, A., Ishchenko, M., Khoperskov, A., Pulsoni, C., Venichenko, Y., Bizyaev, D., Moiseev, A., Extreme kinematic misalignment in IllustrisTNG galaxies: the origin, structure, and internal dynamics of galaxies with a large-scale counterrotation, (2021), MNRAS, 500, 3870.

2) Khoperskov, S., Haywood, M., Snaith, O., Di Matteo, P., Lehnert, M., Vasiliev, E., Naroenkov, S., Berczik, P., Bimodality of [alfa/Fe]-[Fe/H] distributions are a natural outcome of dissipative collapse and disc growth in Milky Way-type galaxies, (2021), MNRAS, 501, 5176.

3) Avramov, B., Berczik, P., Meiron, Y., Acharya, A., Just, A., Properties of loss cone stars in a cosmological galaxy merger remnant, (2021), Astronomy and Astrophysics, 649, A41.

4) Bannikova, E. Y., Sergeyev, A. V., Akerman, N. A., Berczik, P. P., Ishchenko, M. V., Capaccioli, M., Akhmetov, V. S., Dynamical model of an obscuring clumpy torus in AGNs - I. Velocity and velocity dispersion maps for interpretation of ALMA observations, (2021), MNRAS, 503, 1459.

5) Sobolenko, M., Berczik, P., Spurzem, R., Merging timescale for the supermassive black hole binary in interacting galaxy NGC 6240, (2021), Astronomy and Astrophysics, 652, A134.

6) Gualandris, A., Khan, F. M., Bortolas, E., Bonetti, M., Sesana, A., Berczik, P., Holley-Bockelmann, K., Eccentricity evolution of massive black hole binaries from formation to coalescence, (2022), MNRAS, 511, 4753.

Published Papers during the last year which have not directly related to my current PIFI grant:

1) Rizzuto, F. P., Naab, T., Spurzem, R., Giersz, M., Ostriker, J. P., Stone, N. C., Wang, L., Berczik, P., Rampp, M., Intermediate mass black hole formation in compact young massive star clusters, (2021), Monthly Notices of the Royal Astronomical Society, 501, 5257.

2) Meiron, Y., Webb, J. J., Hong, J., Berczik, P., Spurzem, R., Carlberg, R. G., Mass-loss from massive globular clusters in tidal fields, (2021), Monthly Notices of the Royal Astronomical Society, 503, 3000.

3) Shukirgaliyev, B., Otebay, A., Sobolenko, M., Ishchenko, M., Borodina, O., Panamarev, T., Myrzakul, S., Kalambay, M., Naurzbayeva, A., Abdikamalov, E., Polyachenko, E., Banerjee, S., Berczik, P., Spurzem, R., Just, A., Bound mass of Dehnen models with a centrally peaked star formation efficiency, (2021), Astronomy and Astrophysics, 654, A53

4) Kovaleva, D., Ishchenko, M., Postnikova, E., Berczik, P., Piskunov, A. E., Kharchenko, N. V., Polyachenko, E., Reffert, S., Sysoliatina, K., Just, A., Borodina, O., The system of open star clusters Collinder 135 and UBC 7, (2021), Star Clusters: the Gaia Revolution. Online workshop, 17.

5) Kamlah, A. W. H., Leveque, A., Spurzem, R., Arca Sedda, M., Askar, A., Banerjee, S., Berczik, P., Giersz, M., Hurley, J., Belloni, D., Kühmichel, L., Wang, L., Preparing the next gravitational million-body simulations: evolution of single and binary stars in NBODY6++GPU, MOCCA, and MCLUSTER, (2022), Monthly Notices of the Royal Astronomical Society, 511, 4060.

BH’s in galaxies (MW - Sgr A*)

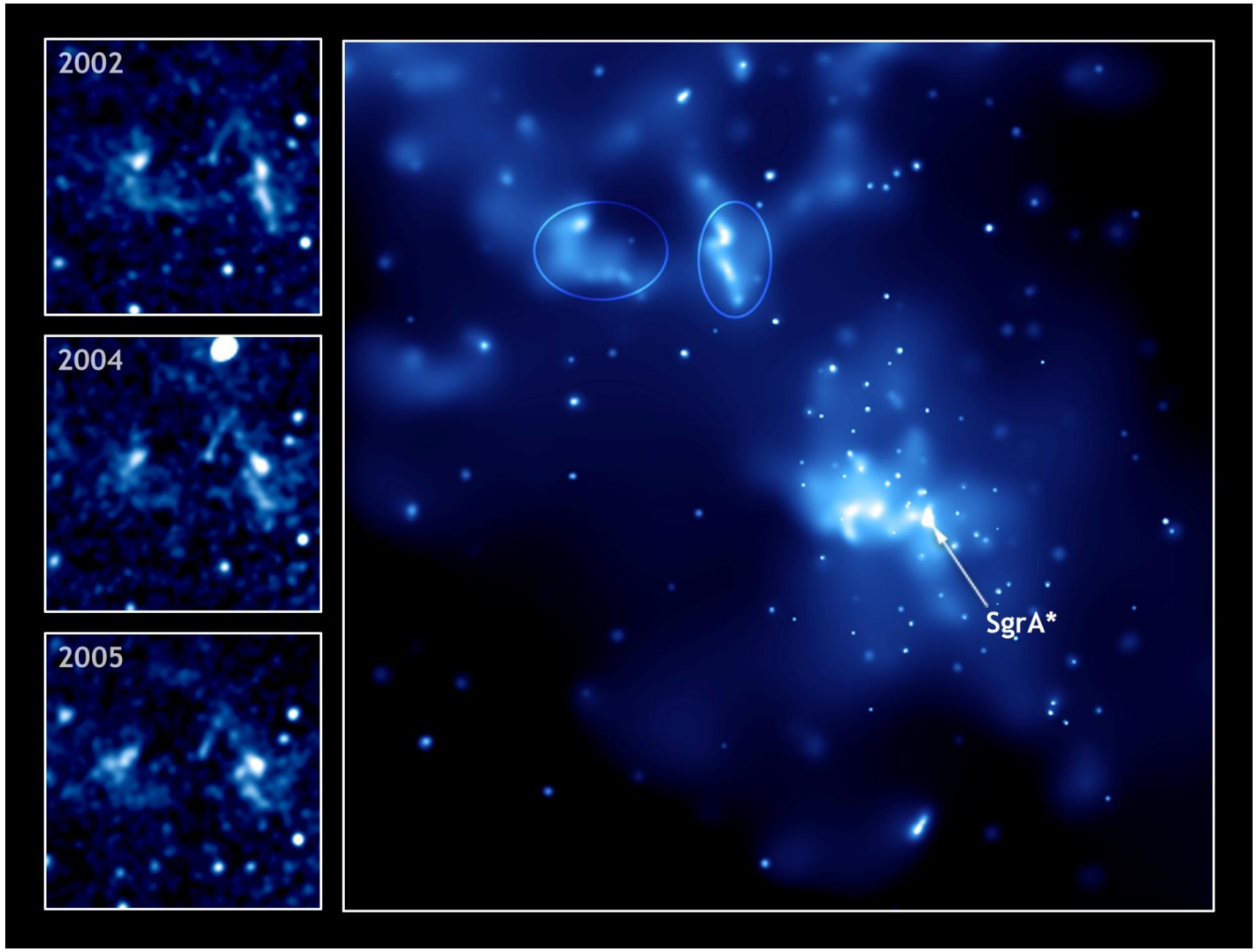

BH's in galaxies (MW - Sgr A*)

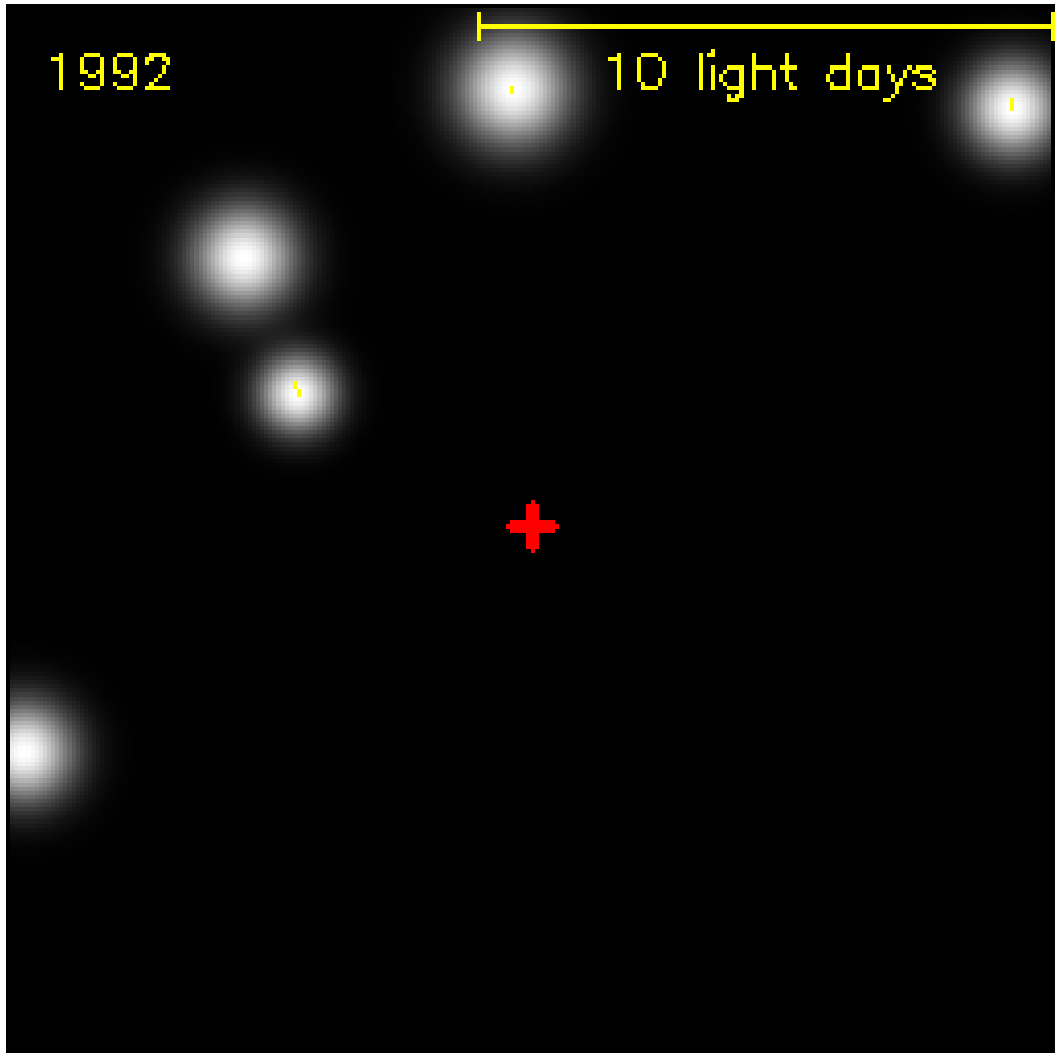

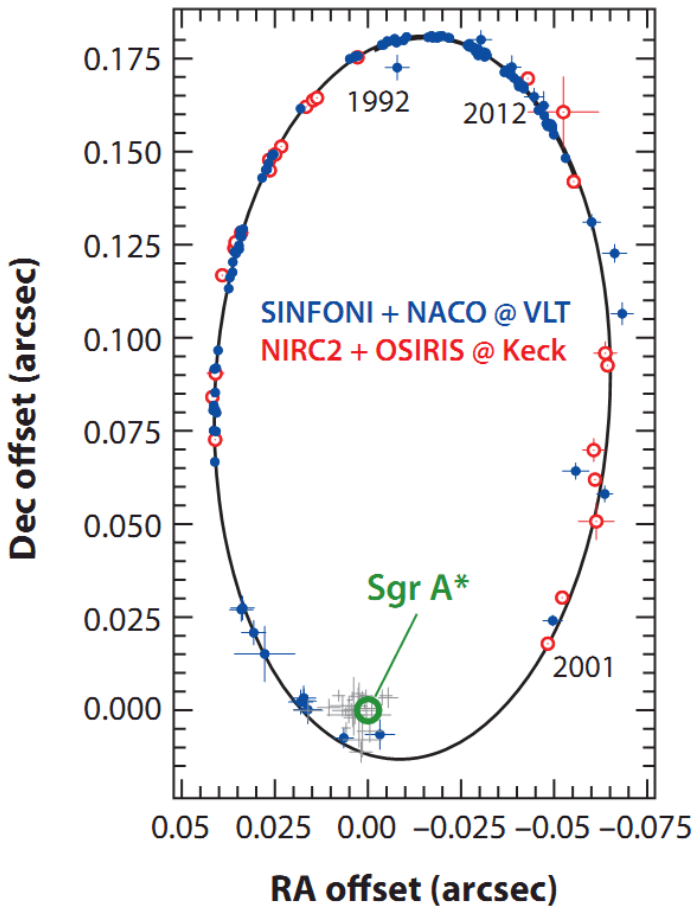

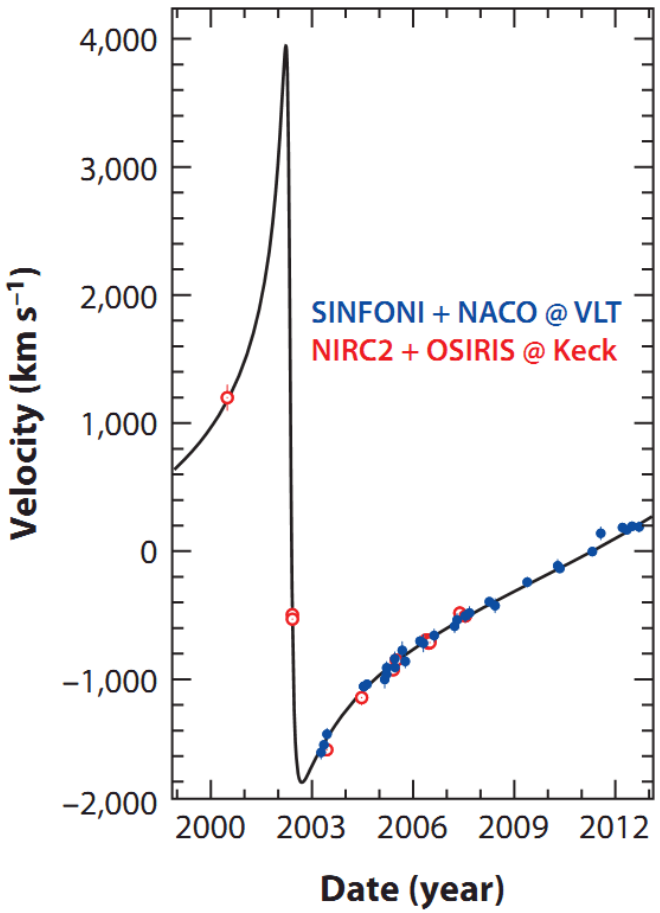

BH's in galaxies (MW - Sgr A*)

The Nobel Prize in Physics 2020

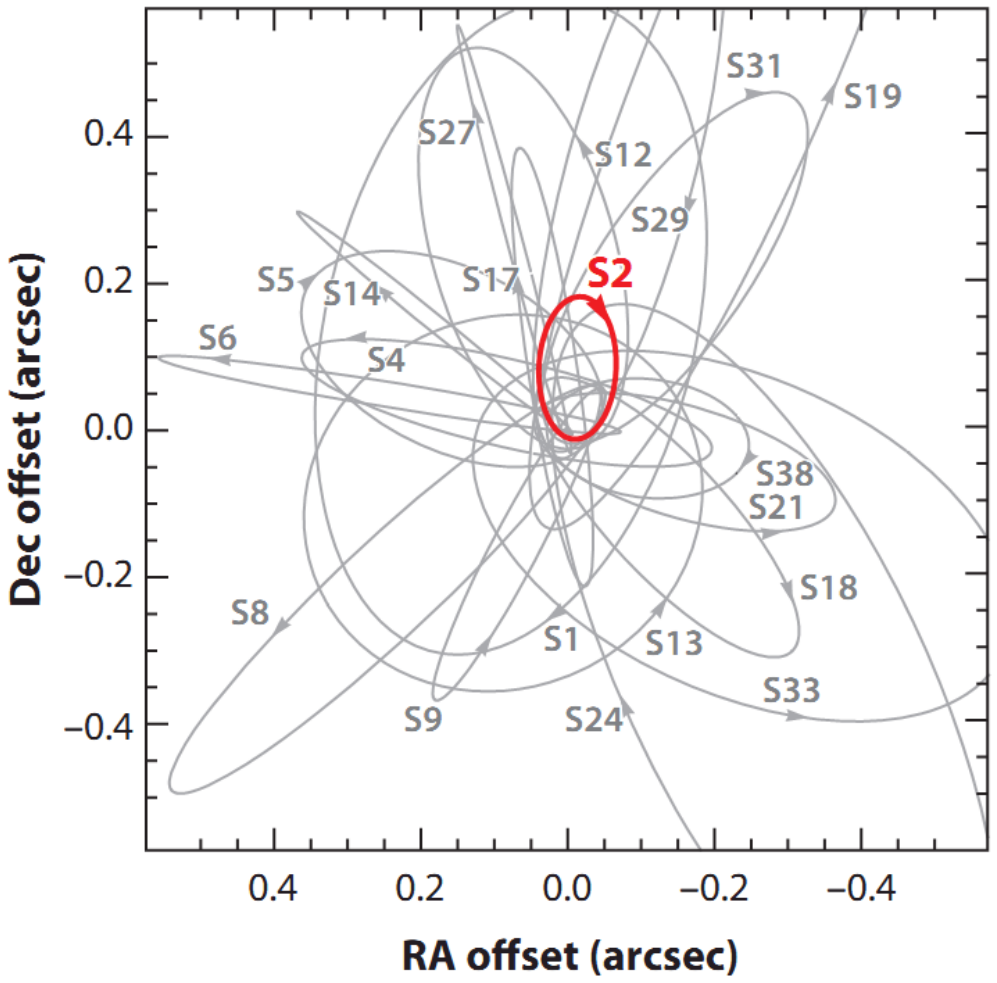

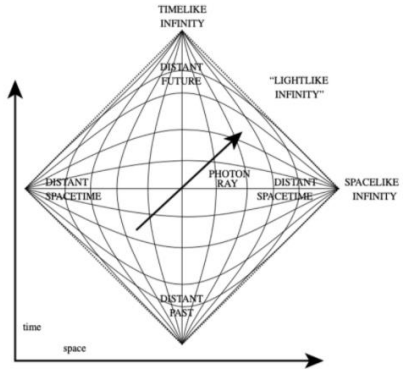

$M_\bullet = 4.30 \pm 0.20(\text{stat}) \pm 0.30(\text{sys}) \times 10^6\ M_\odot$

$R_0 = 8.28(\pm 0.15)_{\text{stat}}(\pm 0.29)_{\text{sys}}$ kpc

$\rho_\bullet > 10^{19.5}\ M_\odot\ \text{pc}^{-3}$

$M_{\text{extended}}/M_\bullet <$ a few $\times\ 10^{-2}$

L-R: Roger Penrose, Reinhard Genzel, Andrea Ghez

John Kormendy and Luis C. Ho,
Annu. Rev. Astron. Astrophys. 2013. 51:511–653

BH's in galaxies

Supermassive black holes (BHs) have been found in 85 galaxies by dynamical modeling of spatially resolved kinematics. The *Hubble Space Telescope* revolutionized BH research by advancing the subject from its proof-of-concept phase into quantitative studies of BH demographics. Most influential was the discovery of a tight correlation between BH mass $M_\bullet$ and the velocity dispersion σ of the bulge component of the host galaxy. Together with similar correlations with bulge luminosity and mass, this led to the widespread belief that BHs and bulges coevolve by regulating each other's growth. Conclusions based on one set of correlations from $M_\bullet \sim 10^{9.5}\,M_\odot$ in brightest cluster ellipticals to $M_\bullet \sim 10^{6}\,M_\odot$ in the smallest galaxies dominated BH work for more than a decade.

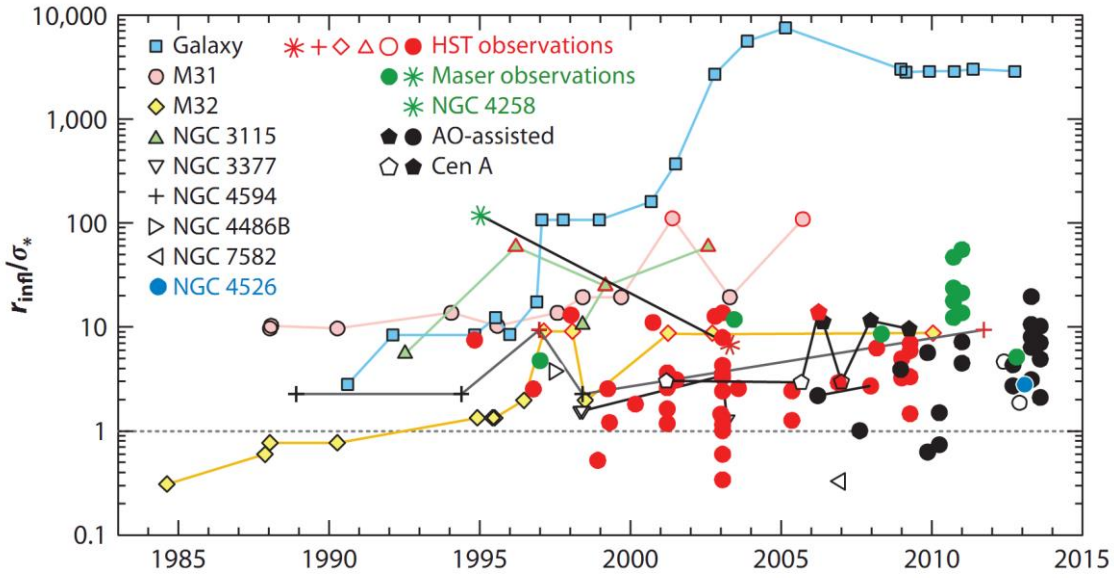

M32 (Tonry 1984, 1987)

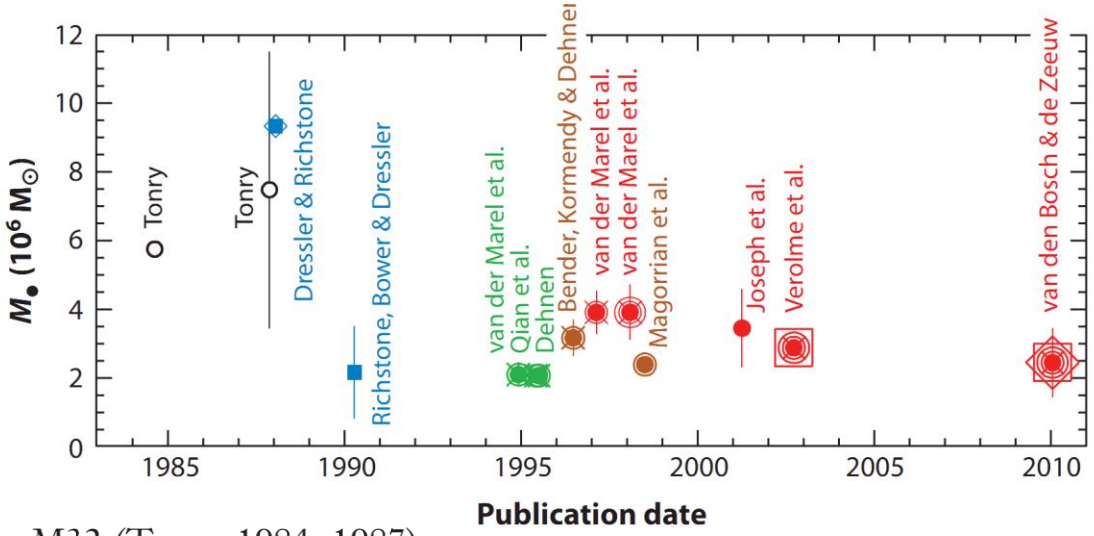

M32 (Tonry 1984, 1987)

New results are now replacing this simple story with a richer and more plausible picture in which BHs correlate differently with different galaxy components. A reasonable aim is to use this progress to refine our understanding of BH-galaxy coevolution. BHs with masses of 10^5–$10^6\,M_\odot$ are found in many bulgeless galaxies. Therefore, classical (elliptical-galaxy-like) bulges are not necessary for BH formation. On the other hand, although they live in galaxy disks, BHs do not correlate with galaxy disks. Also, any $M_\bullet$ correlations with the properties of disk-grown pseudobulges and dark matter halos are weak enough to imply no close coevolution.

John Kormendy and Luis C. Ho,
Annu. Rev. Astron. Astrophys. 2013. 51:511–653

BH's in galaxies

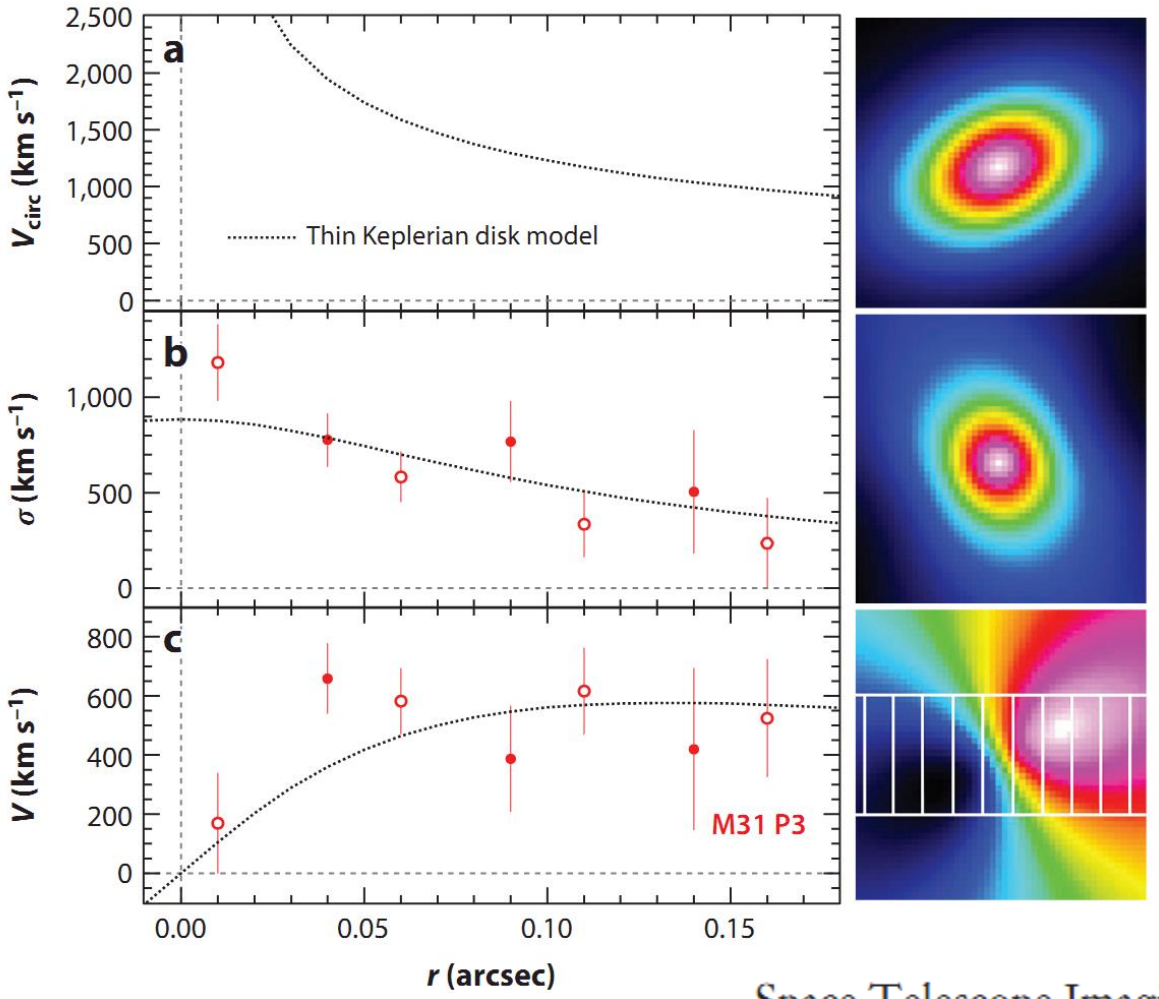

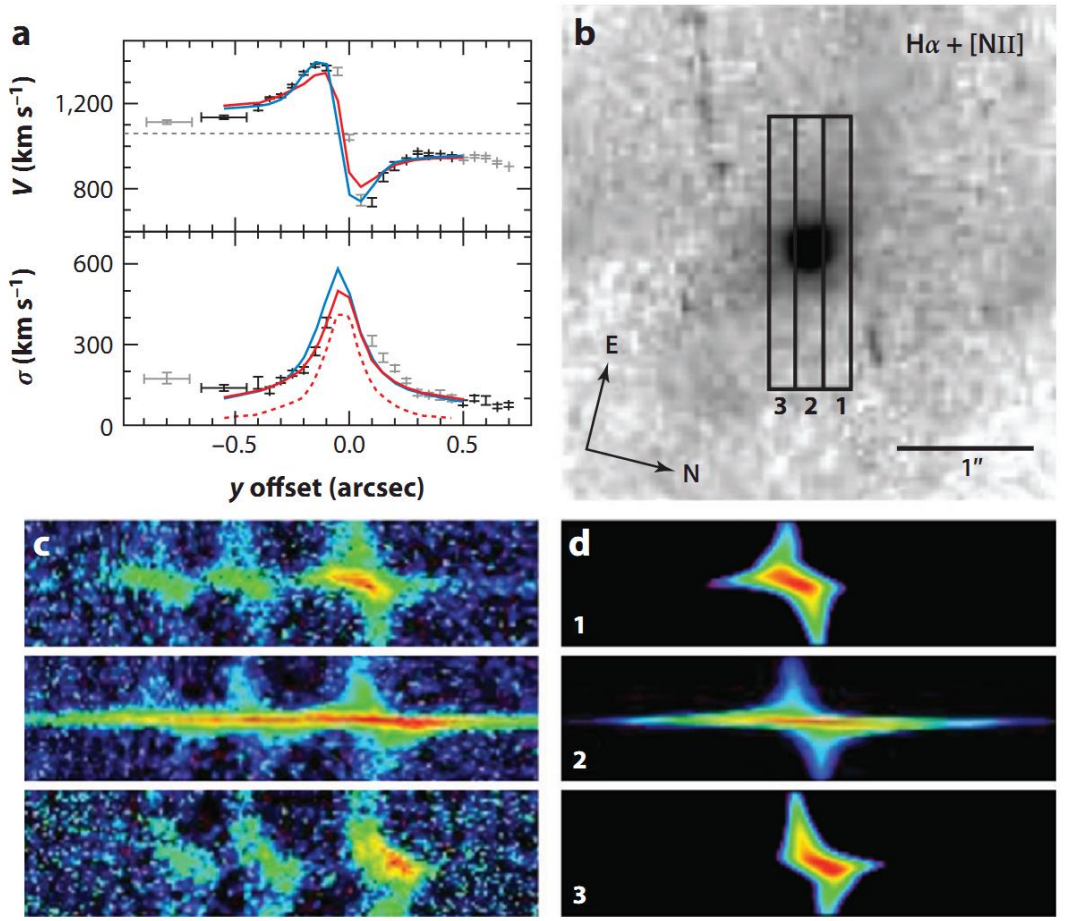

Space Telescope Imaging Spectrograph (STIS) observations of NGC 4374 (Bower et al. 1998)

$$M(r) = \frac{V^2 r}{G} + \frac{\sigma_r^2 r}{G}\left[-\frac{d\ln v}{d\ln r} - \frac{d\ln \sigma_r^2}{d\ln r} - \left(1 - \frac{\sigma_\theta^2}{\sigma_r^2}\right) - \left(1 - \frac{\sigma_\phi^2}{\sigma_r^2}\right)\right]$$

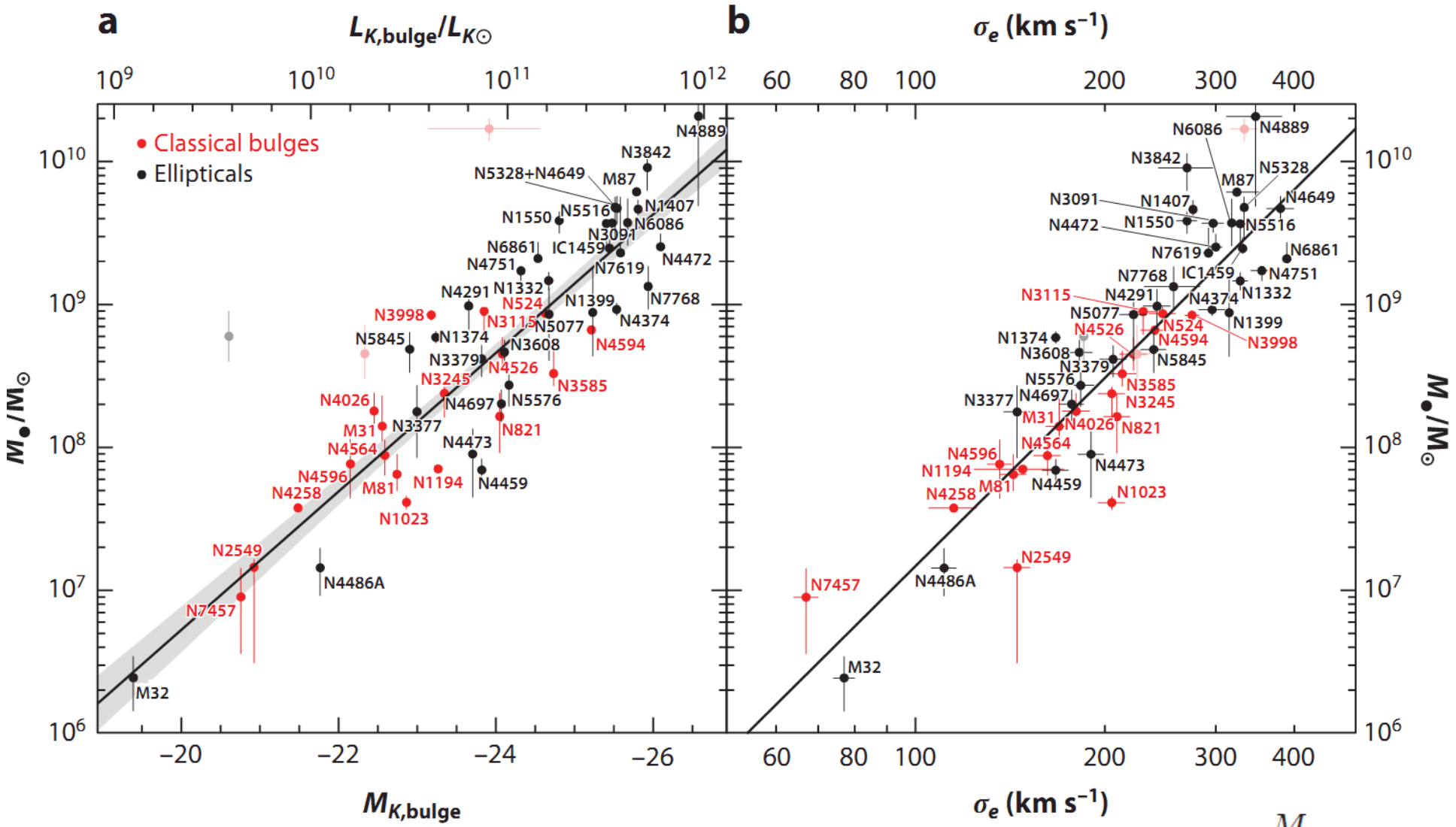

$$\frac{M_\bullet}{10^9\,\mathrm{M}_\odot} = (0.544^{+0.067}_{-0.059}) \left(\frac{L_{K,\mathrm{bulge}}}{10^{11} L_{K\odot}} \right)^{1.22\pm0.08},$$

$$\frac{M_\bullet}{10^9\,\mathrm{M}_\odot} = (0.310^{+0.037}_{-0.033}) \left(\frac{\sigma}{200\,\mathrm{km\,s^{-1}}} \right)^{4.38\pm0.29}.$$

John Kormendy and Luis C. Ho,
Annu. Rev. Astron. Astrophys. 2013. 51:511–653

Galaxy Collisions

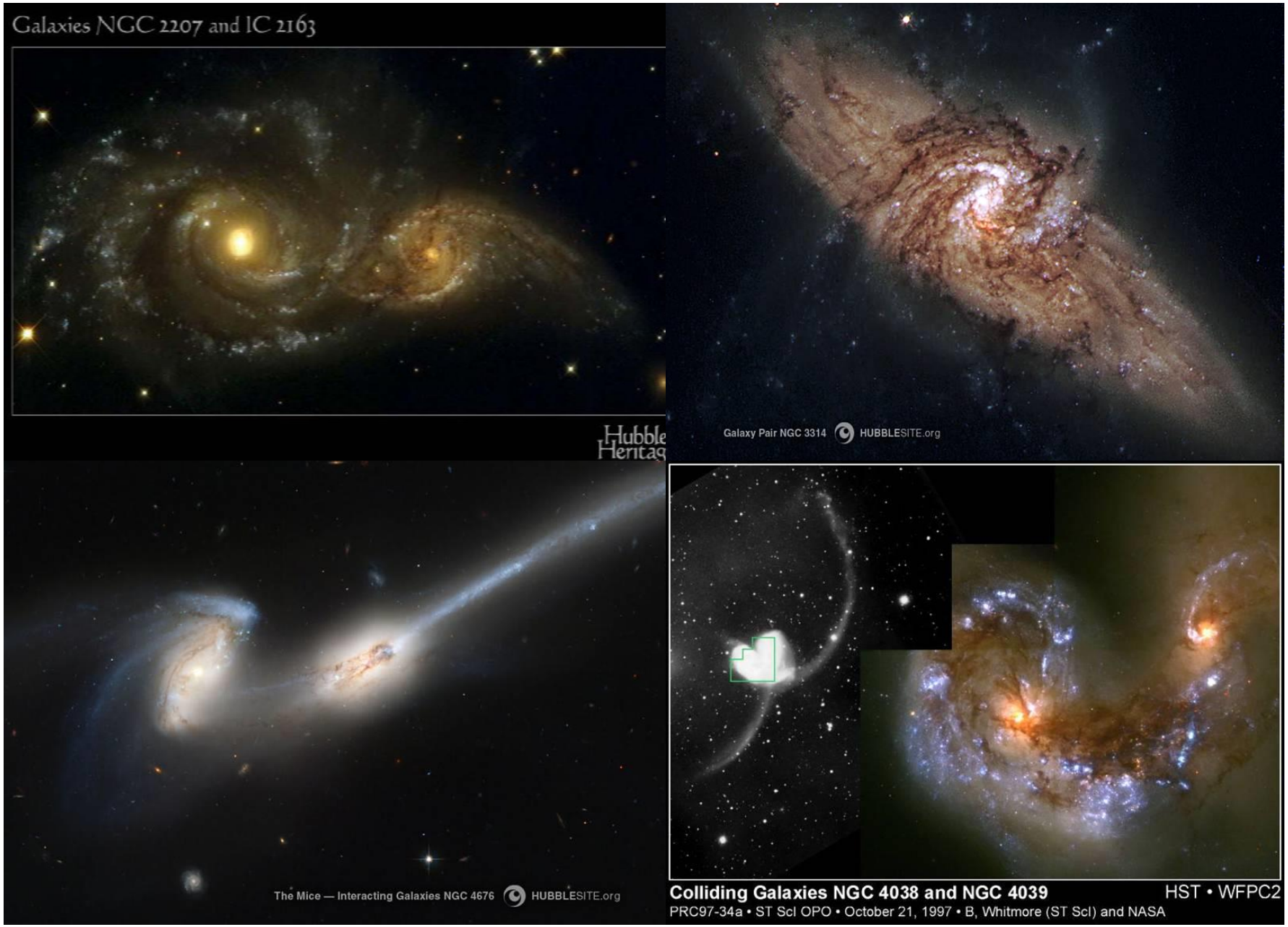

Galaxy Collisions ≈ BH's collisions

Galaxy Collisions ≈ BH's collisions

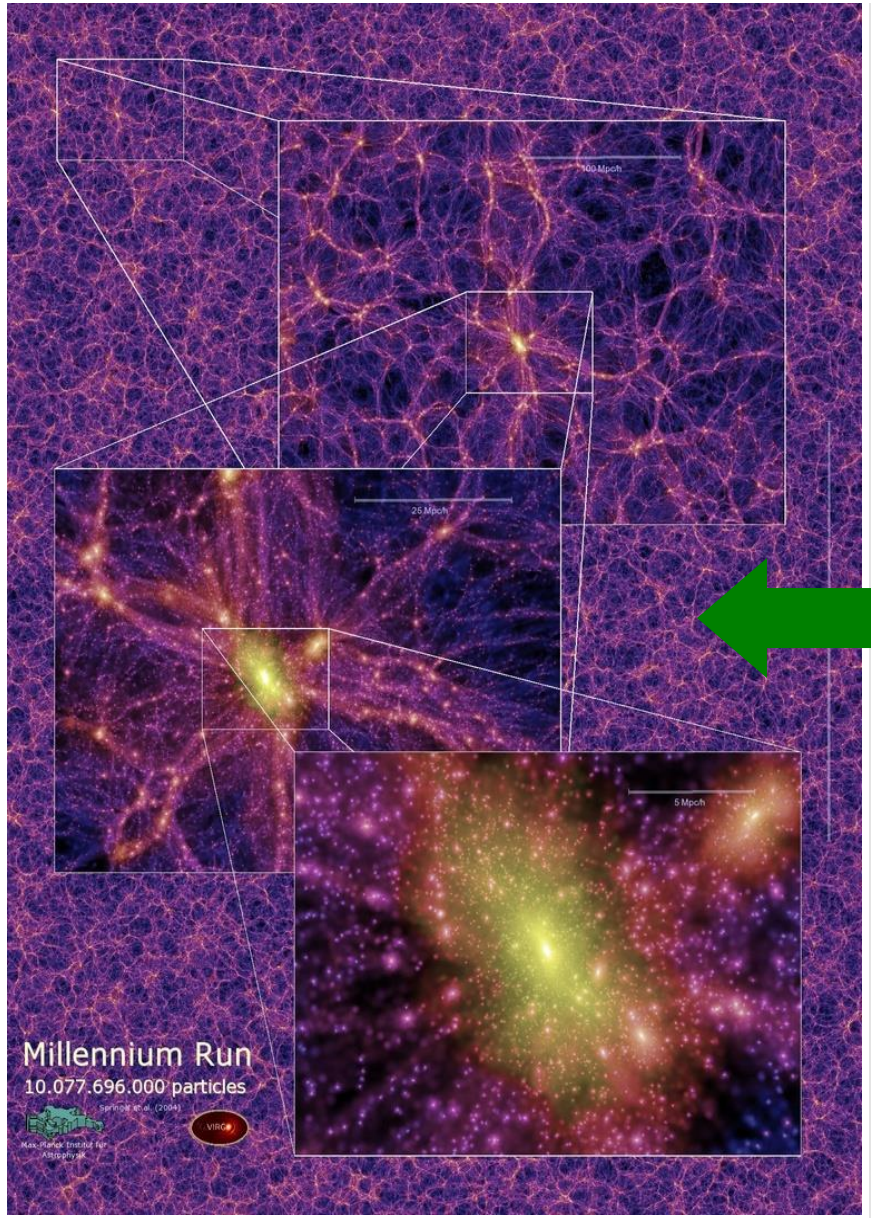

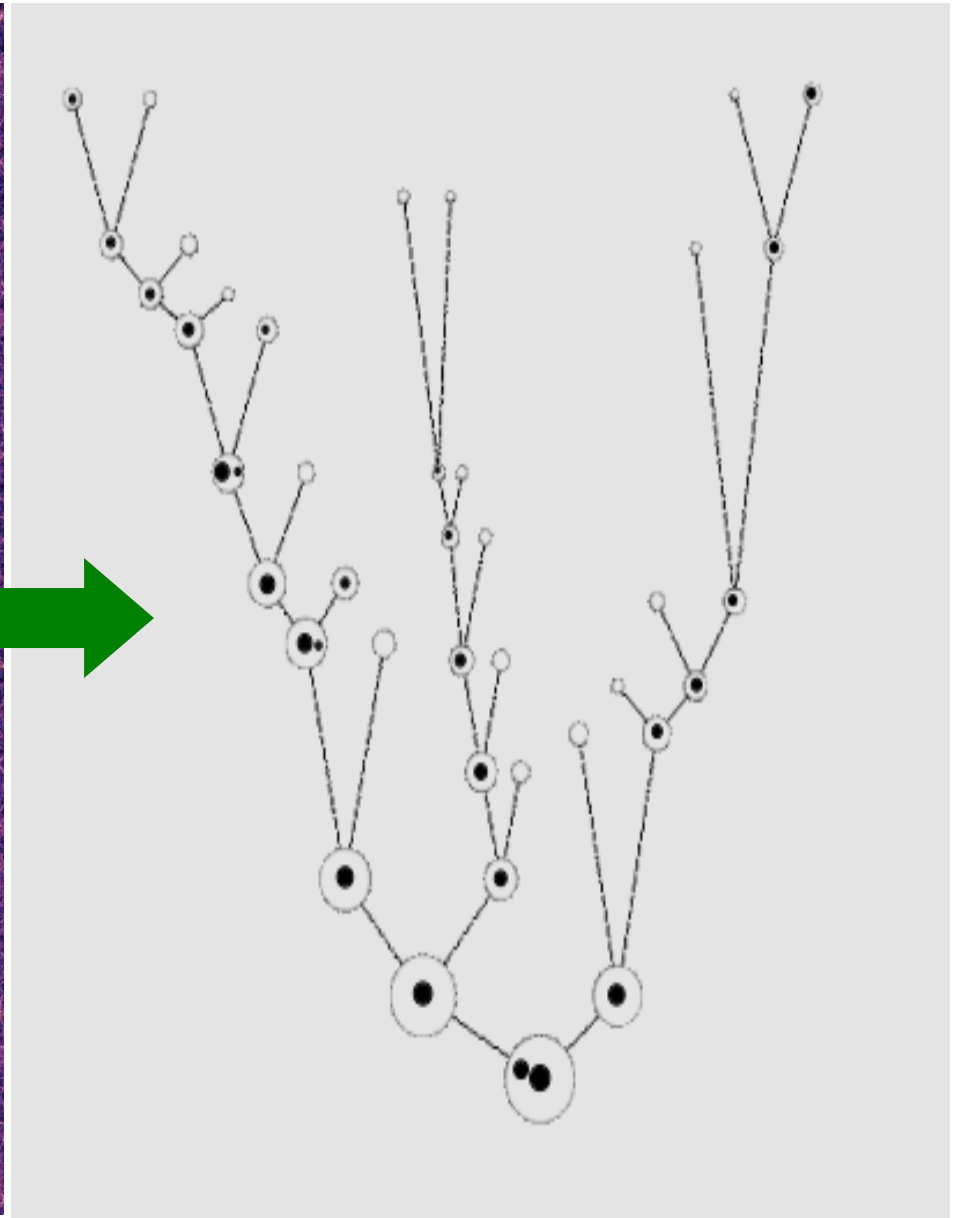

https://www.tng-project.org

-The TNG Collaboration

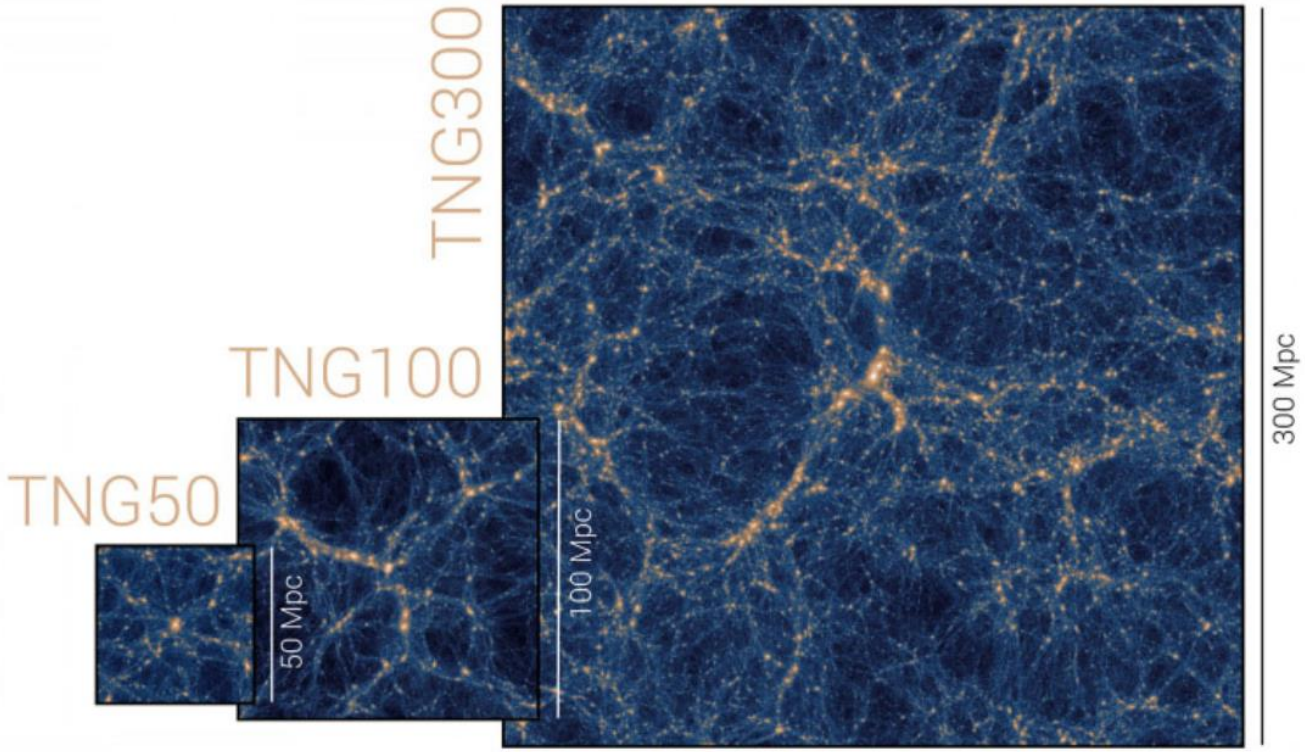

		TNG50	TNG100	TNG300
Volume	$[\mathrm{Mpc}^3]$	51.7^3	110.7^3	302.6^3
L_{box}	$[\mathrm{Mpc}/h]$	35	75	205
N_{GAS}	-	2160^3	1820^3	2500^3
N_{DM}	-	2160^3	1820^3	2500^3
N_{TR}	-	2160^3	2×1820^3	2500^3
m_{baryon}	$[\mathrm{M}_\odot]$	8.5×10^4	1.4×10^6	1.1×10^7
m_{DM}	$[\mathrm{M}_\odot]$	4.5×10^5	7.5×10^6	5.9×10^7
$\epsilon_{\mathrm{gas,min}}$	[pc]	74	185	370
$\epsilon_{\mathrm{DM},\star}$	[pc]	288	740	1480

Volker Springel

Heidelberg Institute for Theoretical Studies ➔ MPA

PI: Overall TNG Project

Lars Hernquist

Harvard University

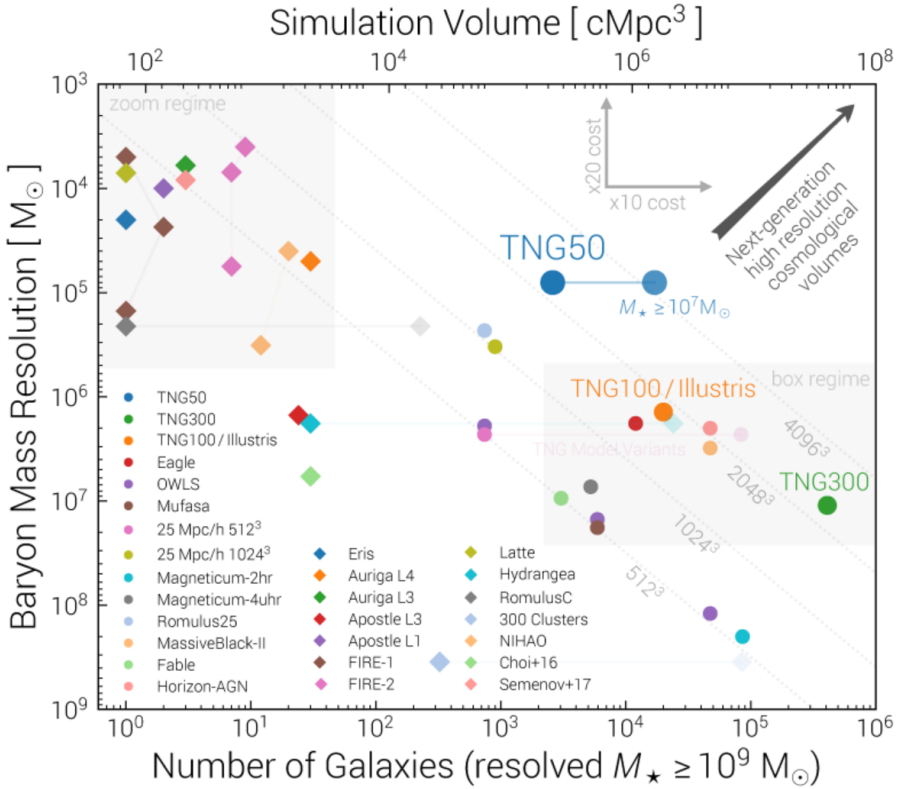

https://www.tng-project.org

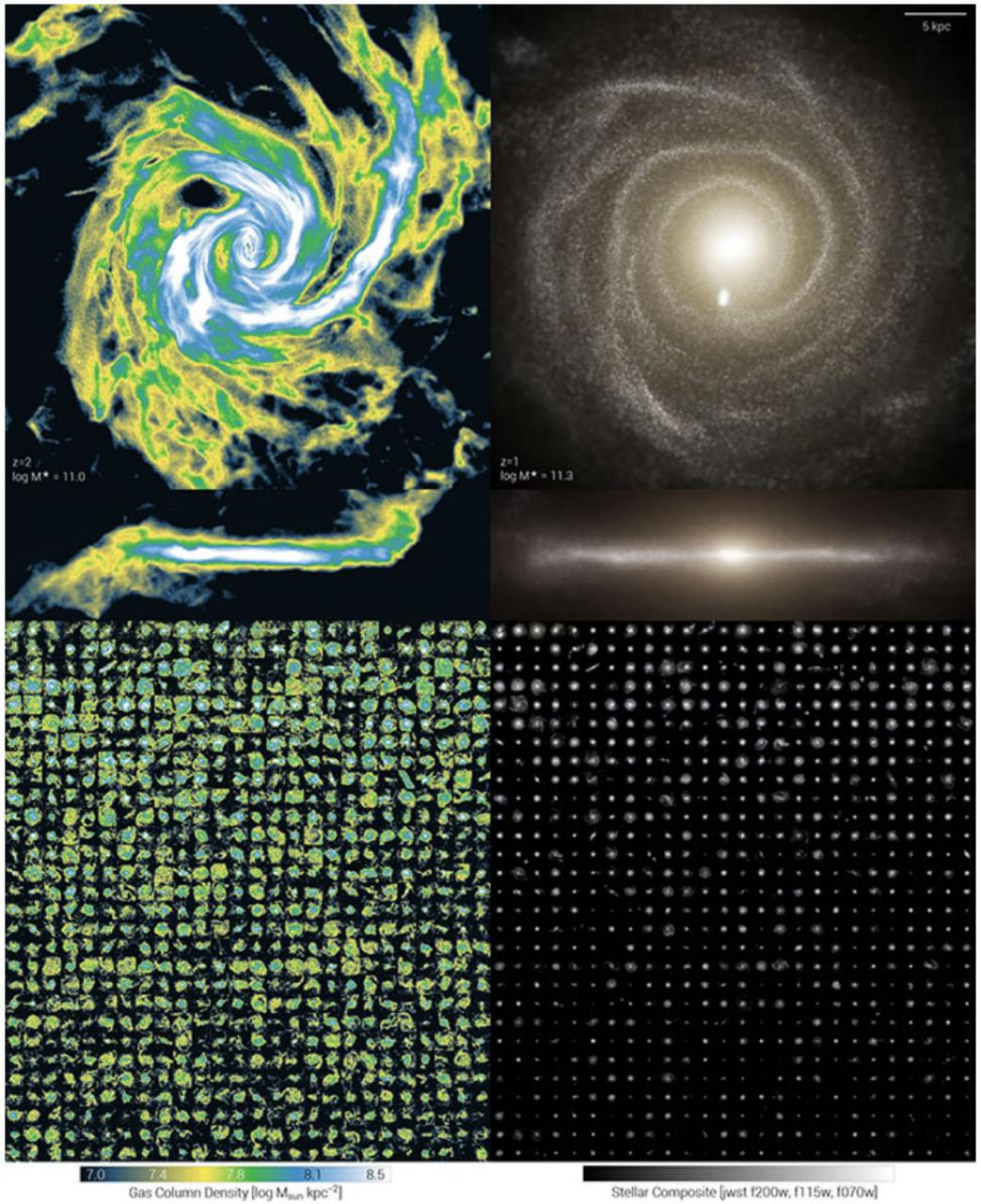

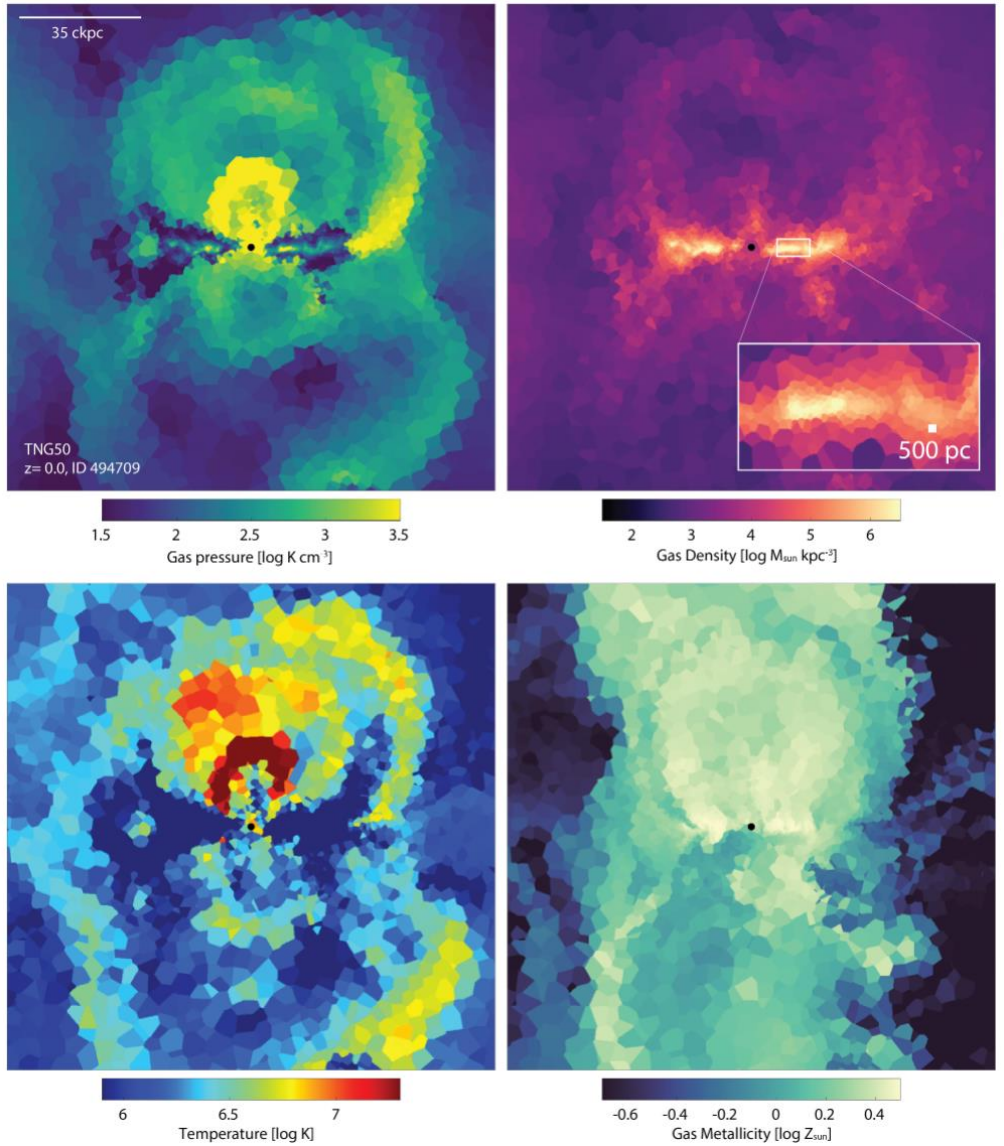

The gaseous (left) and stellar (right) structure of TNG50 galaxies at high redshift. The top shows a massive disk galaxy at z=2 and a descendant at z=1, while the bottom montage reveals ~750 central galaxies at redshift two, from large ellipticals at the center of galaxy groups to smaller, dwarf systems. [large] [ref]

A outflow-driven "bubble" produced by supermassive black hole feedback, around a disky galaxy similar to our own Milky Way at redshift zero, found within the TNG50 simulation. This structure is similar to those observed in gamma-rays by the Fermi telescope, and in x-rays by the eROSITA mission, in our own Galaxy. [large] [ref]

Galaxy Collisions ≈ BH's collisions

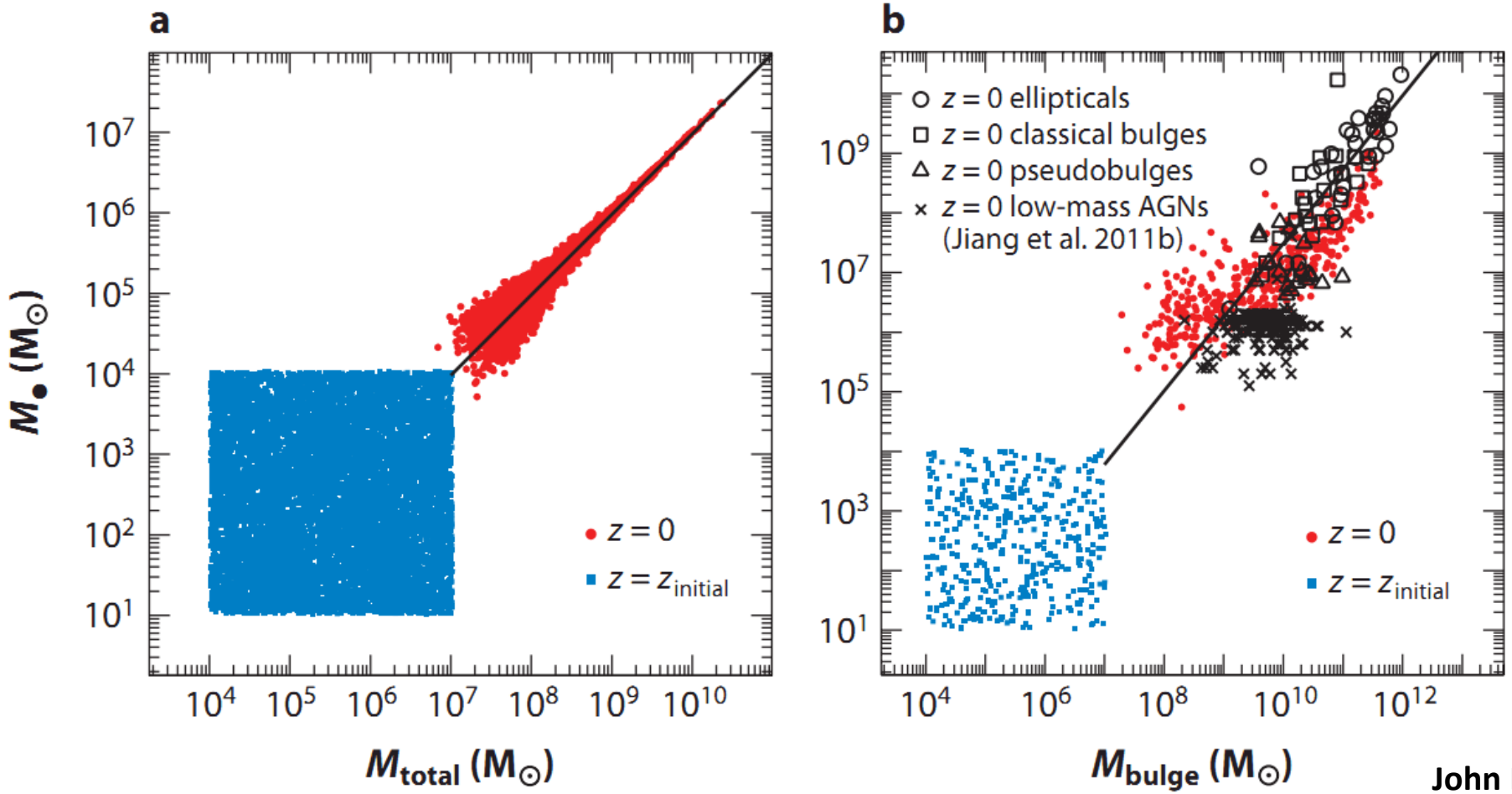

John Kormendy and Luis C. Ho

(*a*) Numerical experiment to show how a correlation (*red points*) between BH mass and bulge stellar mass is produced from an initially uncorrelated distribution (*blue points*) by a succession of dry mergers. A tight linear correlation emerges, and the scatter decreases toward higher masses. The solid line has a slope of 1. (*b*) Here, a subset of 400 randomly selected merger trees include simple prescriptions for star formation, BH accretion, population of dark matter halos with stars, and conversion of disks to bulges during major mergers. Overplotted in black is the Section 5 database of dynamically measured BH masses supplemented by low-mass BHs from Greene & Ho (2004, 2007c) that have bulge photometry in Jiang et al. (2011). The line is the best-fit $M_\bullet$-M_{bulge} relation from Section 6.6.1 (Equation 10). Simulations adapted from Jahnke & Macciò (2011).

Galaxy Collisions ≈ BH's collisions

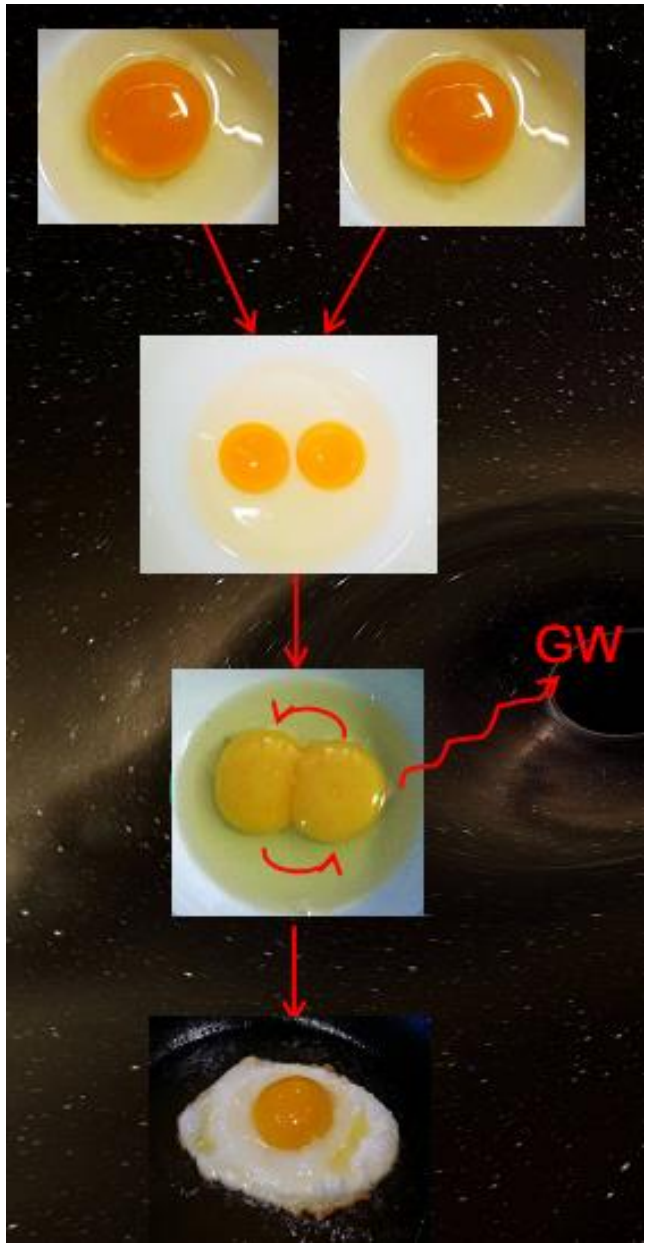

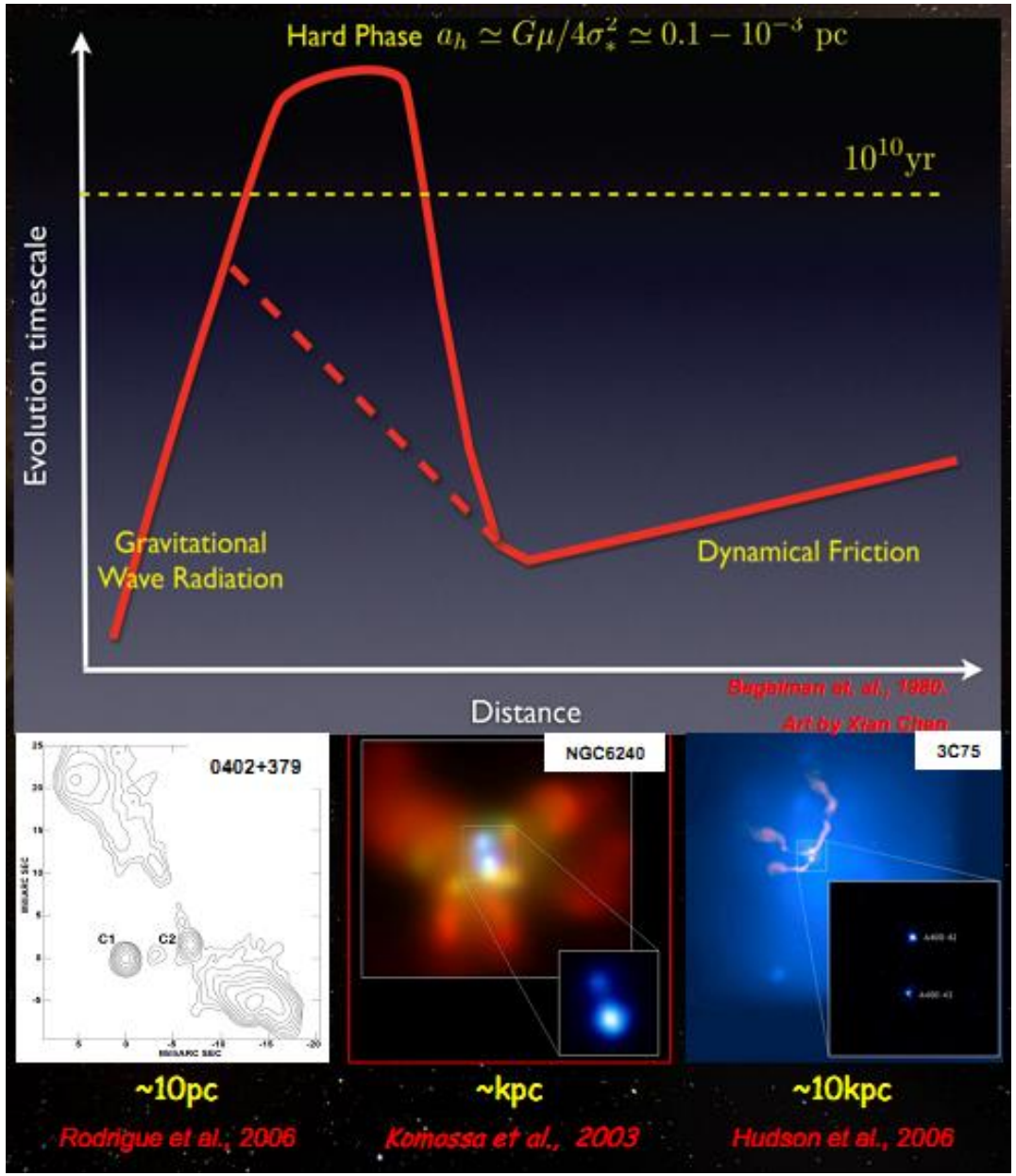

Slide from Li Shuo (NAOC, CAS)

0. Hybrid and direct N-body code development. GPU optimization…

1. Merging timescale for the supermassive black hole binary in interacting galaxy NGC 6240.

2. Dynamical model of an obscuring clumpy torus in AGNs. Velocity and velocity dispersion maps for interpretation of ALMA observations.

3. Properties of loss cone stars in a cosmological galaxy merger remnant.

4. Eccentricity evolution of massive black hole binaries from formation to final coalescence. Gravitational Wave (GW) emission calculation.

Double & Triple SMBH evolution in galaxy centers. New hybrid code approaches and performance tests.

MAO 3+2 new nodes 4xGF 2080S + 4xGF 3070

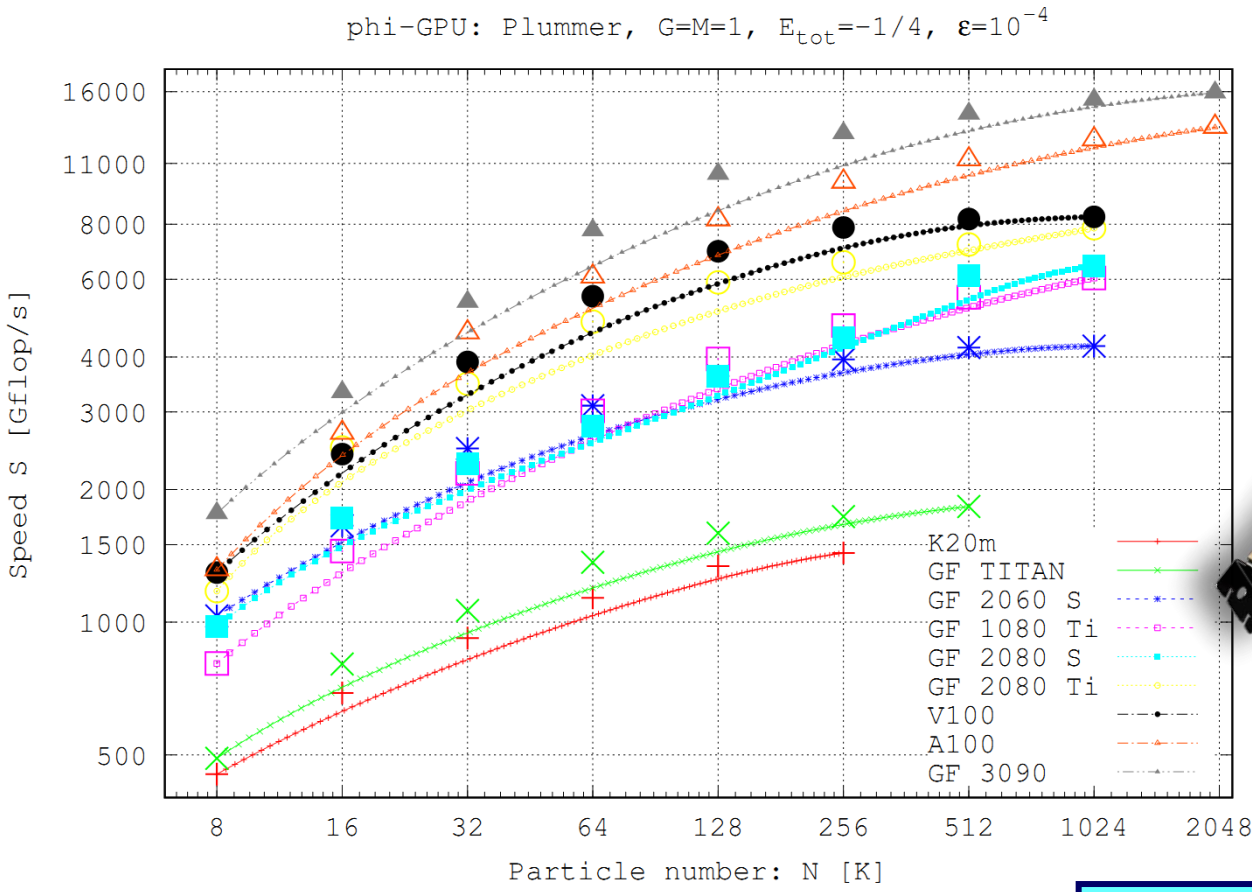

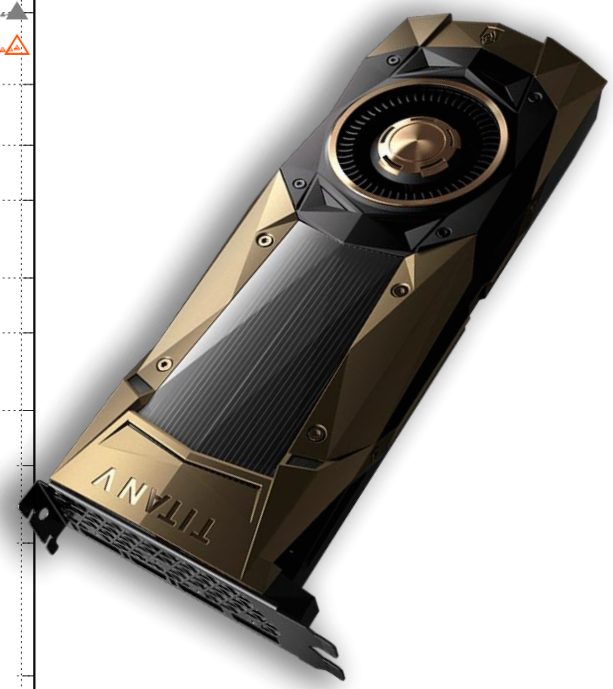

4 x GF 2080S, 3072 SP @ 1.81 GHz
4 x GF 3070, 5888 SP @ 1.77 GHz

JUWELS Booster consists of 936 compute nodes, each equipped with 4 NVIDIA A100 GPUs. The GPUs are hosted by AMD EPYC Rome CPUs. The compute nodes are connected with HDR-200 InfiniBand in a DragonFly+ topology.

The InfiniBand network of JUWELS Booster is implemented as a DragonFly+ network.

48 nodes are combined in a switch group (*cell*), interconnected in a full fat-tree topology, with 10 leaf switches and 10 spine switches in a two-level configuration. 40 Tbit/s of bi-section bandwidth is available.

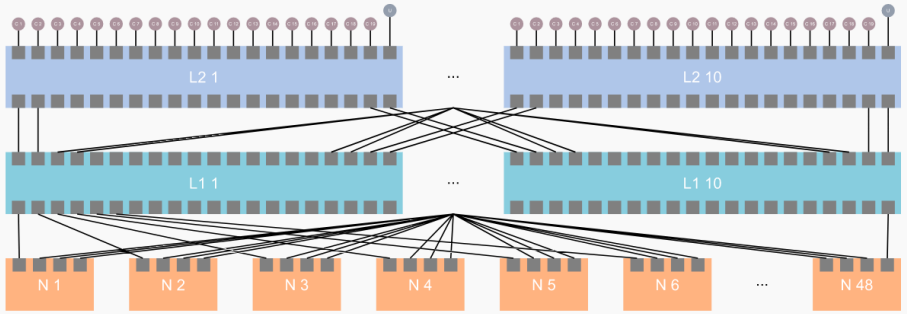

Sketch of the network topology within a JUWELS Booster cell with 48 nodes (`N1` to `N 48`), 10 level 1 switches (`L1 1` to `L1 10`) and 10 level 2 switches (`L2 1` to `L2 10`). Only a small subset of the total amount of links are shown for readability. The purple, 20th link leaving each level 2 switch should indicate the connection to JUWELS Cluster, while the other 19 outgoing level 2 links connect to other cells.

The configuration of JUWELS Booster compute nodes is the following

- **CPU**: AMD EPYC 7402 processor; 2 sockets, 24 cores per socket, SMT-2 (total: 2×24×2 = 96 threads) in NPS-4 [1] configuration (details on WikiChip)
- **Memory**: 512 GB DDR4-3200 RAM (of which at least 20 GB is taken by the system software stack, including the file system); 256 GB per socket; 8 memory channels per socket (2 channels per NUMA domain)
- **GPU**: 4 × NVIDIA A100 Tensor Core GPU with 40 GB; connected via NVLink3 to each other
- **Network**: 4 × Mellanox HDR200 InfiniBand ConnectX 6 (200 Gbit/s each), *HCA*
- **Periphery**: CPU, GPU, and network adapter are connected via 2 PCIe Gen 4 switches with 16 PCIe lanes going to each device (CPU socket: 2×16 lanes). PCIe switches are configured in *synthetic mode*.

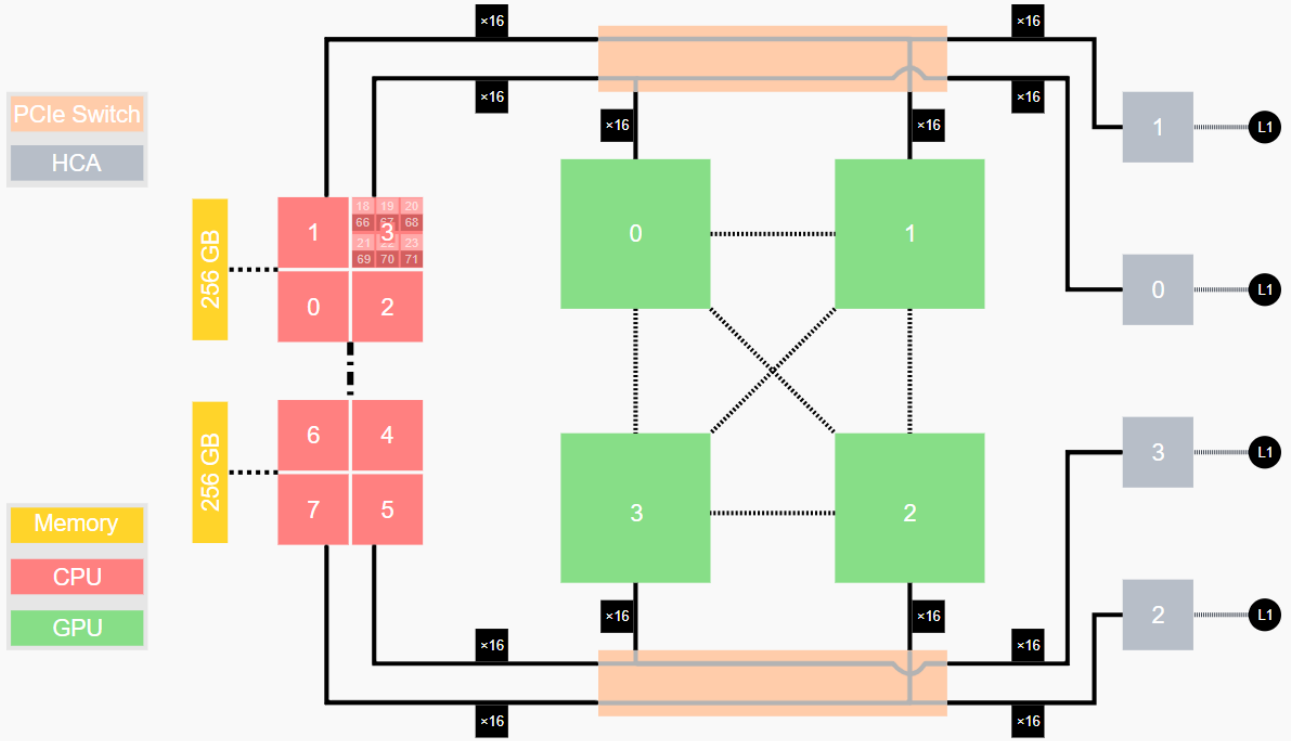

TOP500 LIST - NOVEMBER 2021

Rank	System	Cores	Rmax (TFlop/s)	Rpeak (TFlop/s)	Power (kW)
1	**Supercomputer Fugaku** - Supercomputer Fugaku, A64FX 48C 2.2GHz, Tofu interconnect D, Fujitsu RIKEN Center for Computational Science Japan	7,630,848	442,010.0	537,212.0	29,899
2	**Summit** - IBM Power System AC922, IBM POWER9 22C 3.07GHz, NVIDIA Volta GV100, Dual-rail Mellanox EDR Infiniband, IBM DOE/SC/Oak Ridge National Laboratory United States	2,414,592	148,600.0	200,794.9	10,096
3	**Sierra** - IBM Power System AC922, IBM POWER9 22C 3.1GHz, NVIDIA Volta GV100, Dual-rail Mellanox EDR Infiniband, IBM / NVIDIA / Mellanox DOE/NNSA/LLNL United States	1,572,480	94,640.0	125,712.0	7,438
4	**Sunway TaihuLight** - Sunway MPP, Sunway SW26010 260C 1.45GHz, Sunway, NRCPC National Supercomputing Center in Wuxi China	10,649,600	93,014.6	125,435.9	15,371
5	**Perlmutter** - HPE Cray EX235n, AMD EPYC 7763 64C 2.45GHz, NVIDIA A100 SXM4 40 GB, Slingshot-10, HPE DOE/SC/LBNL/NERSC United States	761,856	70,870.0	93,750.0	2,589
6	**Selene** - NVIDIA DGX A100, AMD EPYC 7742 64C 2.25GHz, NVIDIA A100, Mellanox HDR Infiniband, Nvidia NVIDIA Corporation United States	555,520	63,460.0	79,215.0	2,646
7	**Tianhe-2A** - TH-IVB-FEP Cluster, Intel Xeon E5-2692v2 12C 2.2GHz, TH Express-2, Matrix-2000, NUDT National Super Computer Center in Guangzhou China	4,981,760	61,444.5	100,678.7	18,482
8	**JUWELS Booster Module** - Bull Sequana XH2000 , AMD EPYC 7402 24C 2.8GHz, NVIDIA A100, Mellanox HDR InfiniBand/ParTec ParaStation ClusterSuite, Atos Forschungszentrum Juelich (FZJ) Germany	449,280	44,120.0	70,980.0	1,764

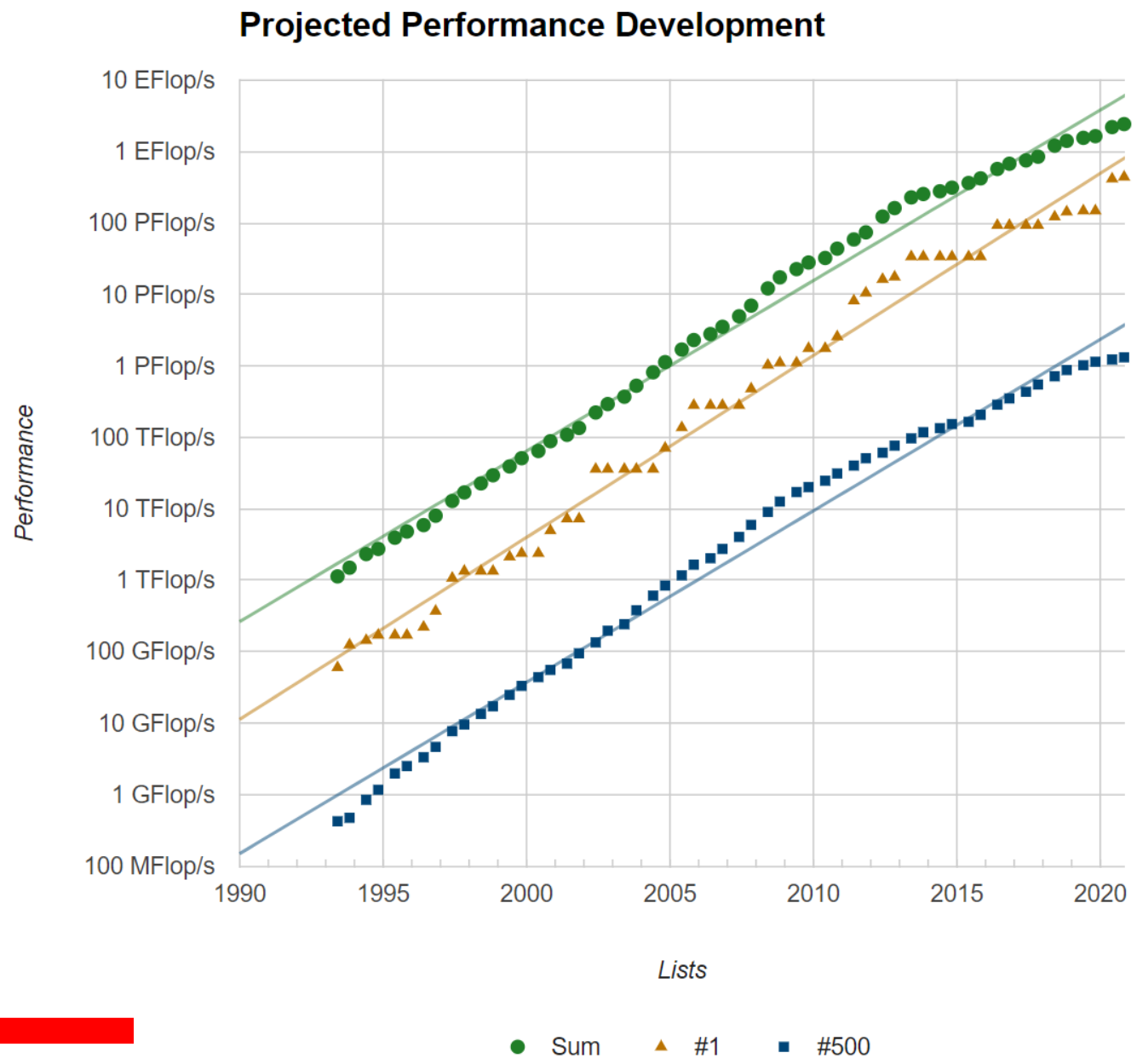

Our φGRAPE/GPU (parallel) N-body code

Harfst et al, NewA, 12, 357 (2007) [astro-ph/0608125]

Hierarchical Individual Block Time Steps

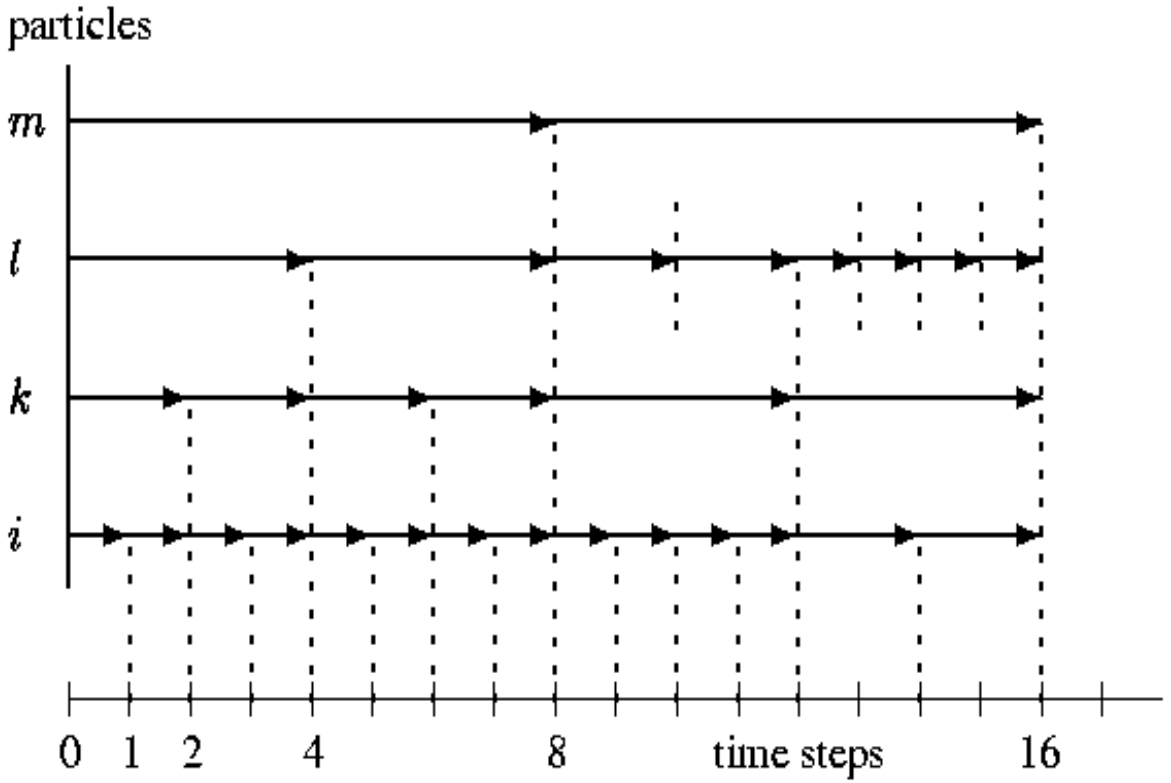

$$\Delta t = \sqrt{\eta \frac{|\vec{a}||\vec{a}^{(2)}| + |\dot{\vec{a}}|^2}{|\dot{\vec{a}}||\vec{a}^{(3)}| + |\vec{a}^{(2)}|^2}} \,.$$

4th order Hermite scheme

$$\frac{d^2\vec{r}_i}{dt^2} = \vec{a}_i$$

ftp://ftp.mao.kiev.ua/pub/berczik/phi-GRAPE/

Our φGRAPE/GPU (parallel) N-body code

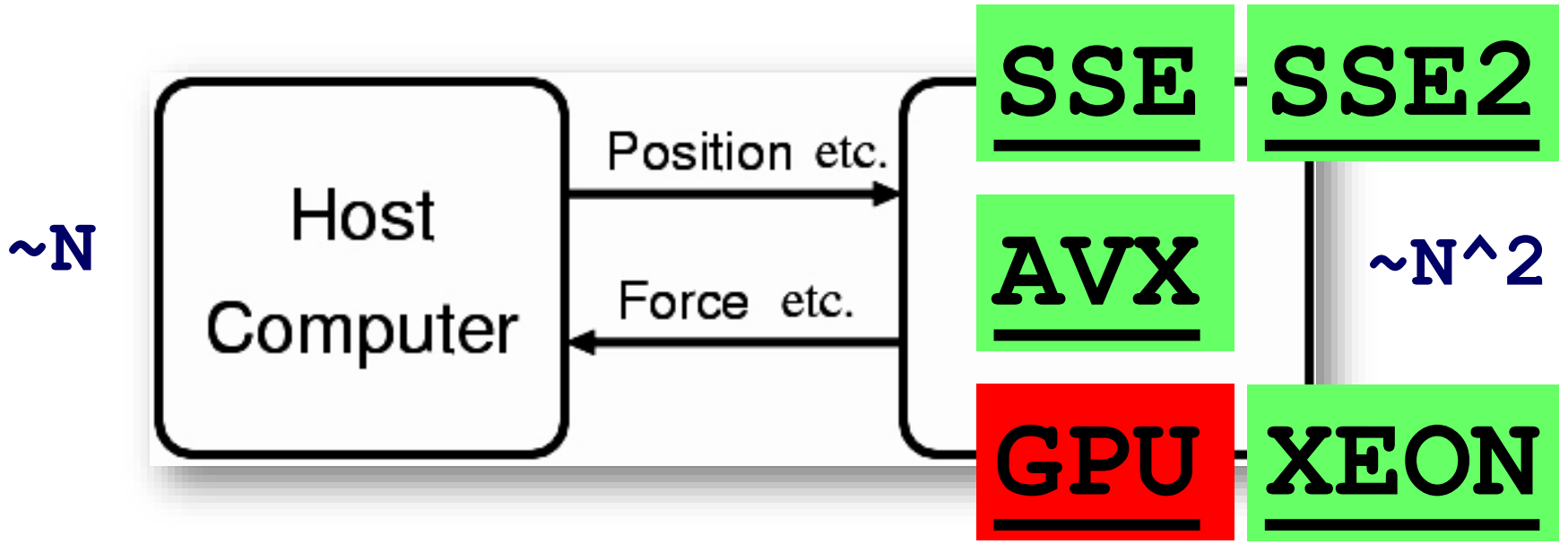

$$\vec{a}_i = \sum_{j=1;\, j\neq i}^{N} \vec{f}_{ij} \qquad \vec{f}_{ij} = -\frac{G \cdot m_j}{(r_{ij}^2 + \varepsilon^2)^{3/2}} \vec{r}_{ij}$$

ftp://ftp.mao.kiev.ua/pub/berczik/phi-GRAPE/

Our CPU/GPU "hybrid" N-body code

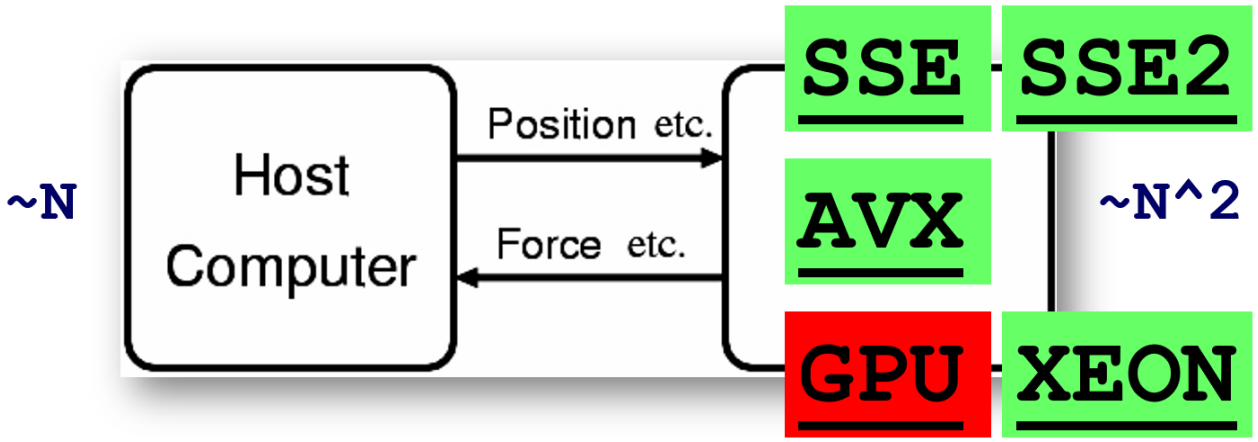

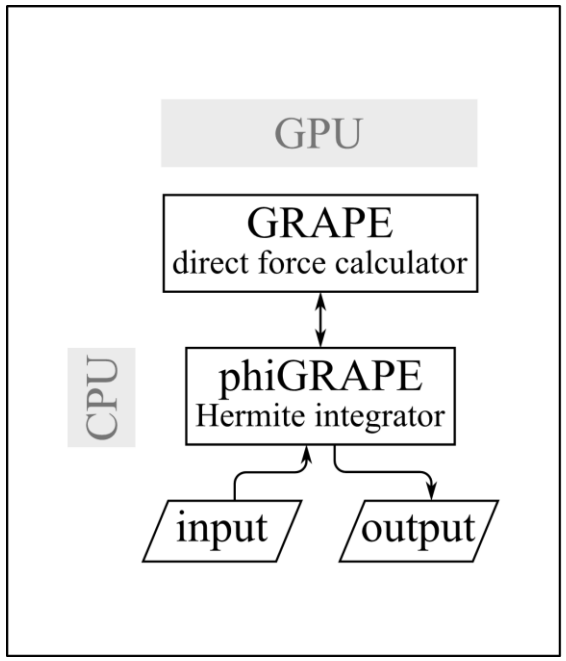

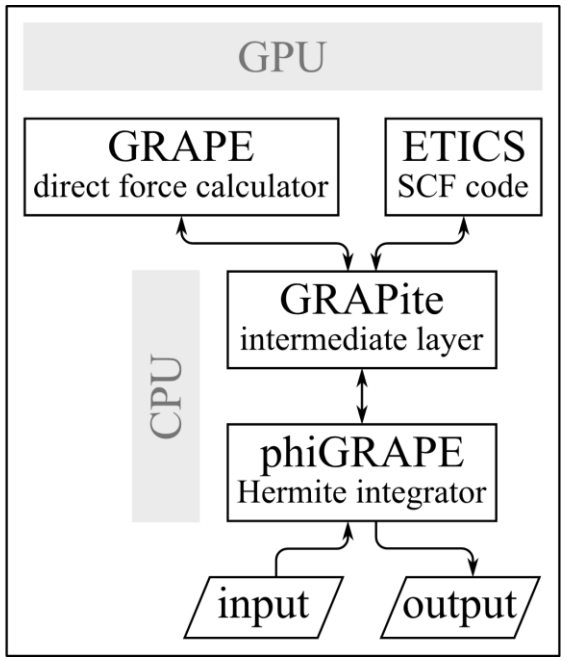

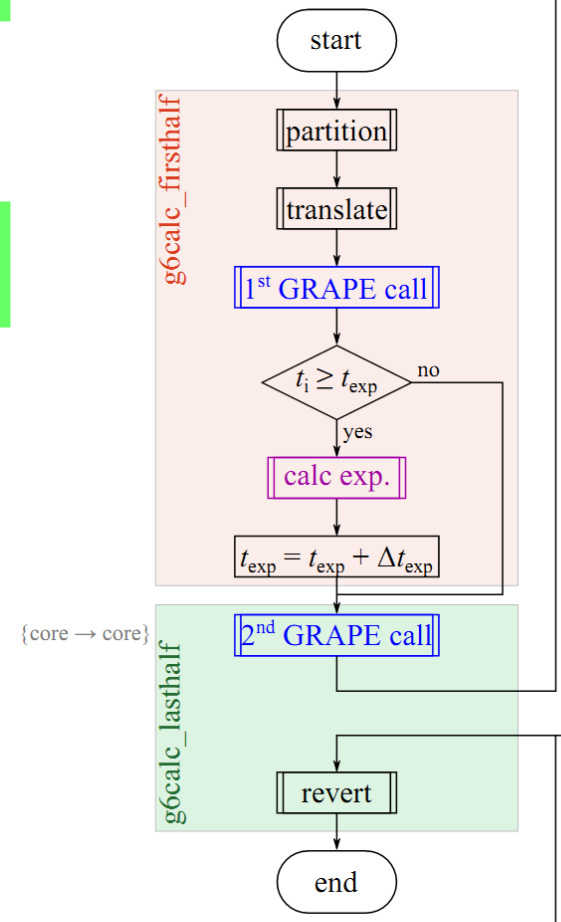

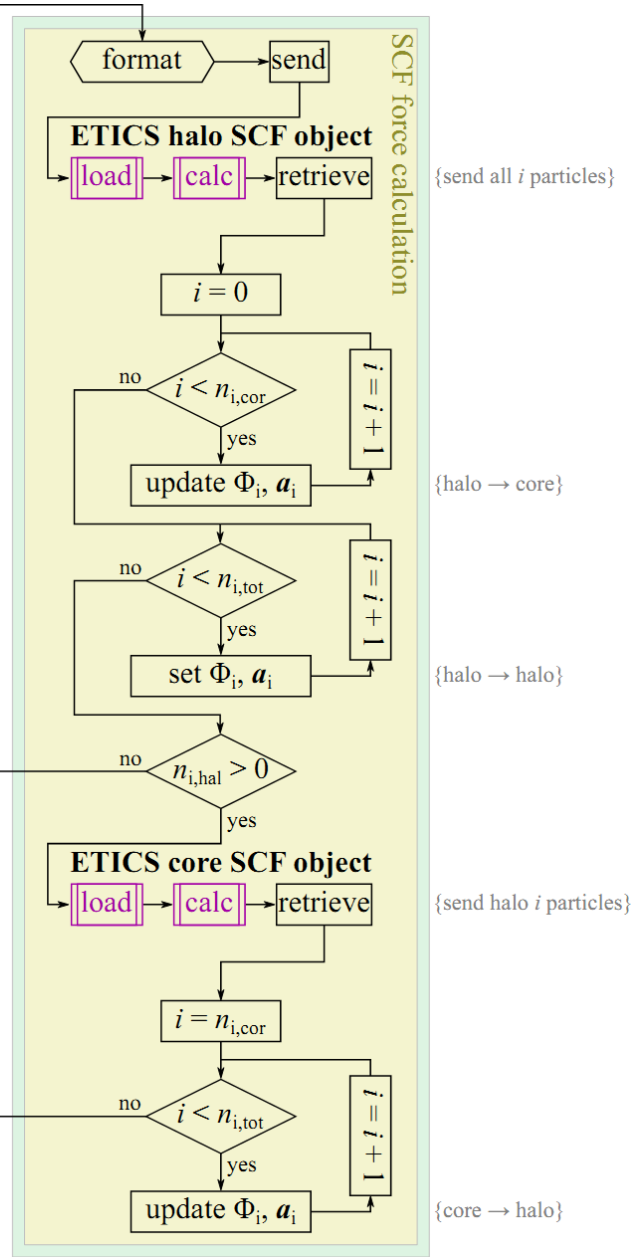

Slide from Yohai...

Our φGRAPE/GPU (parallel) N-body code

N

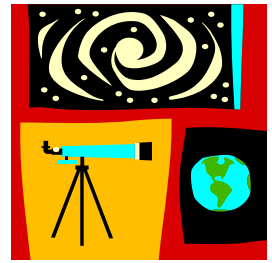

MPI_Bcast

MPI_Reduce

N_{act}

$m_i; \vec{r}_i; \vec{v}_i; t_i$

$\varphi_i; \vec{a}_i; \dot{\vec{a}}_i$

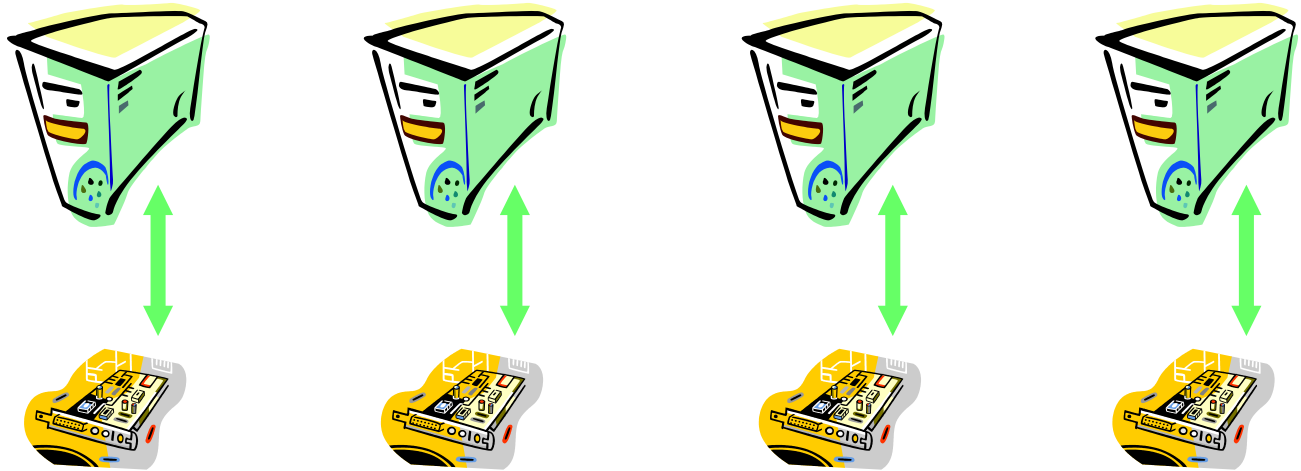

MPI_Scatter

N/N_{GPU}

$m_j; \vec{r}_j; \vec{v}_j; t_j$

Our φGRAPE/GPU (parallel) N-body code

$$i, j - particle$$

Some communication scheme...

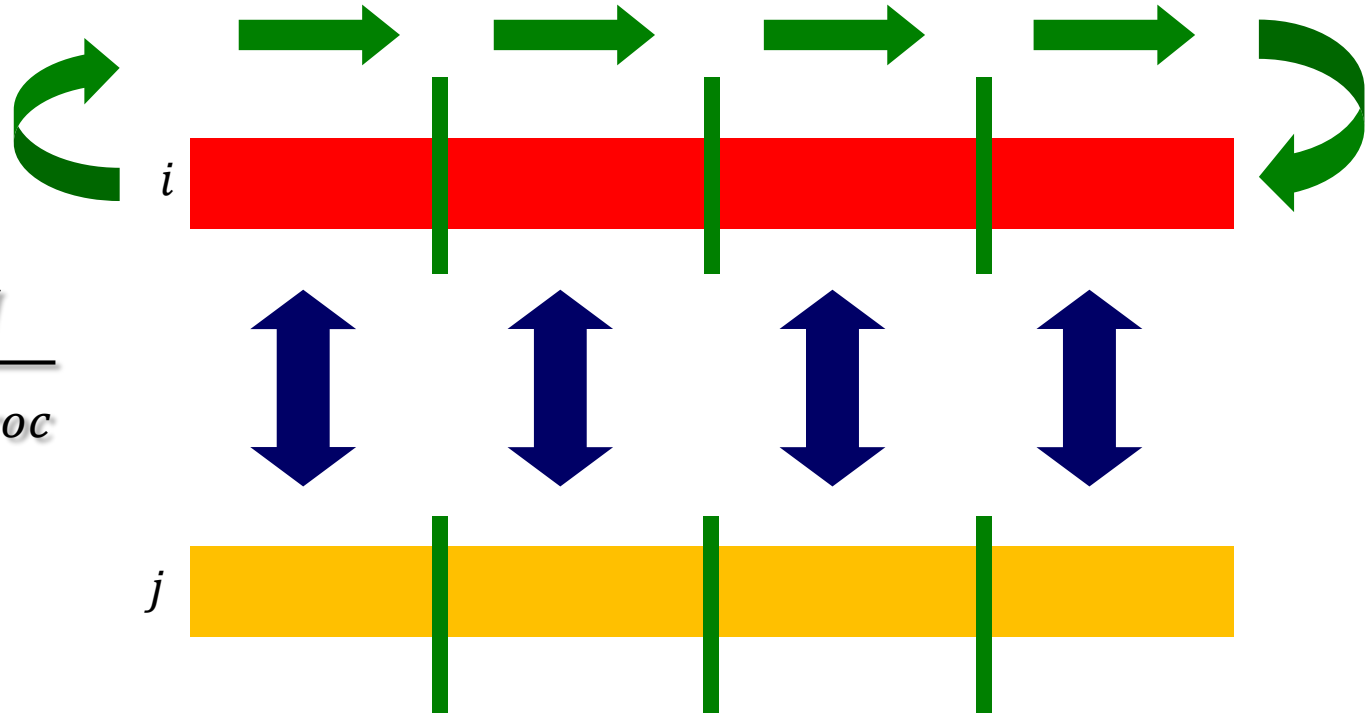

$$N_{loc} = \frac{N}{N_{proc}}$$

Our φGRAPE/GPU (parallel) N-body code

http://adsabs.harvard.edu/abs/2011hpc..conf....8B

- active part. scan: $O(N_{act} \log(N_{act}))$ $+T_{host}$
- all part. prediction: $O(N/N_{GPU})$ $+T_{host}$
- ''j'' part. send. to GPU: $O(N/N_{GPU})$ $+T_{comm}$
- ''i'' part. send. to GPU: $O(N_{act})$ $+T_{comm}$
- ''force'' determ. on GPU: $O(N\ N_{act}/N_{GPU})$ $+T_{GPU}$
- receive the ''force'': $O(N_{act})$ $+T_{comm}$
- MPI global comm.: $O((\tau_{lat}+N_{act}) \log(N_{GPU}))$ $+T_{MPI}$
- corr. for ''i'' part.: $O(N_{act})$ $+T_{host}$

ftp://ftp.mao.kiev.ua/pub/berczik/phi-GPU/

Our φGRAPE/GPU (parallel) N-body code

http://adsabs.harvard.edu/abs/2011hpc..conf....8B

$$\Delta T_{total} = \Delta T_{host} + \Delta T_{GPU} + \Delta T_{comm} + \Delta T_{MPI}$$

$$\Delta T_{MPI} \propto (\tau_{lat} + N_{act}) \cdot \log(N_{GPU})$$

$$\Delta T_{GPU} \propto N \cdot \frac{N_{act}}{N_{GPU}}$$

ftp://ftp.mao.kiev.ua/pub/berczik/phi-GPU/

Our CPU/GPU "hybrid" N-body code

$$M(r) = M_o \cdot \frac{1}{(1 + (r_o/r)^2)^{3/2}}$$

$$\rho(r) = \frac{3 \cdot M_o}{4\pi \cdot {r_o}^3} \cdot \frac{1}{(1 + (r/r_o)^2)^{5/2}}$$

$$r_{HM} \approx 0.769$$

$$G = M = 1$$

$$E_{TOT} = -\frac{1}{4}$$

$$r_o = \frac{3\pi}{16} \approx 0.6$$

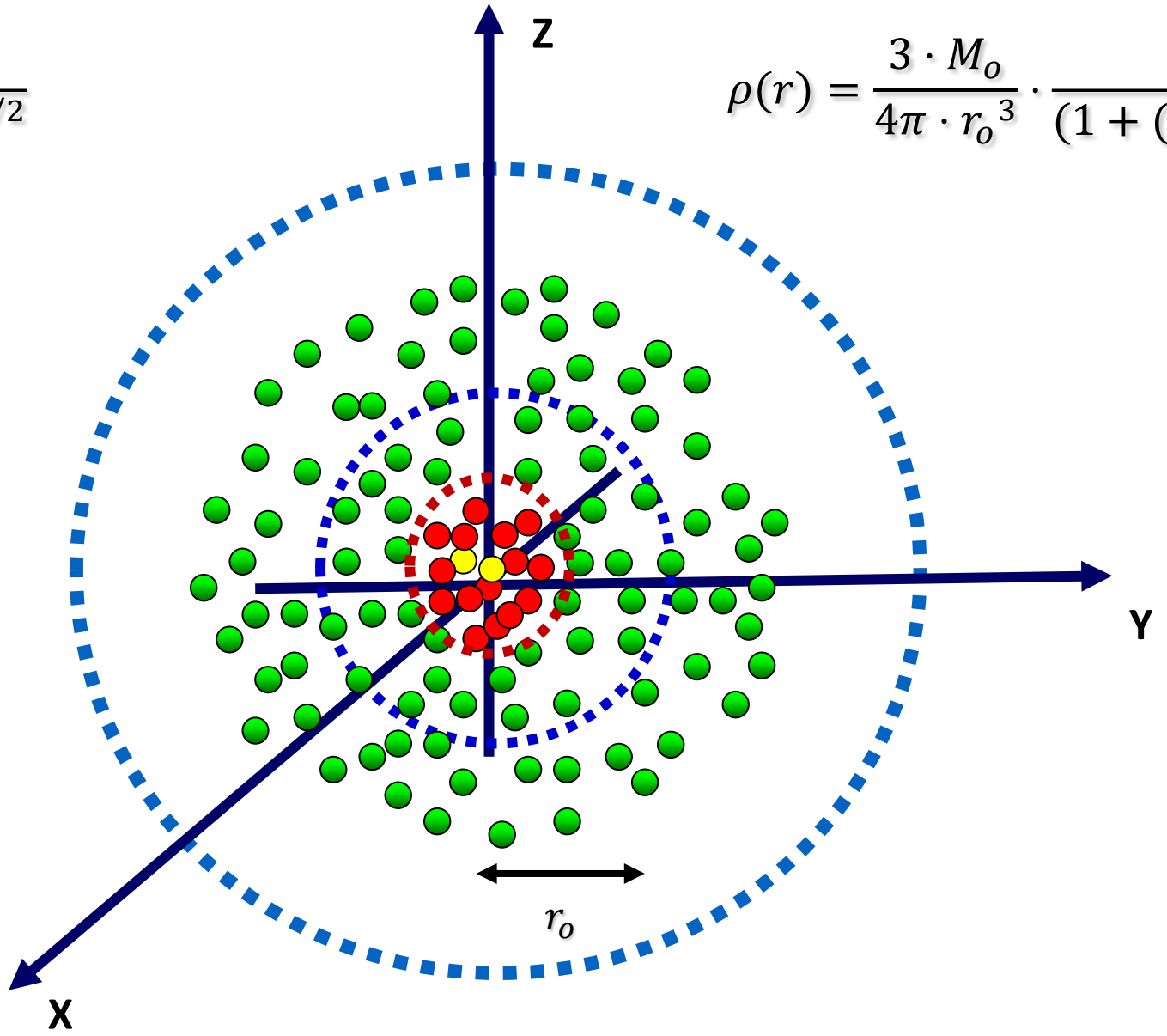

Initial Condition

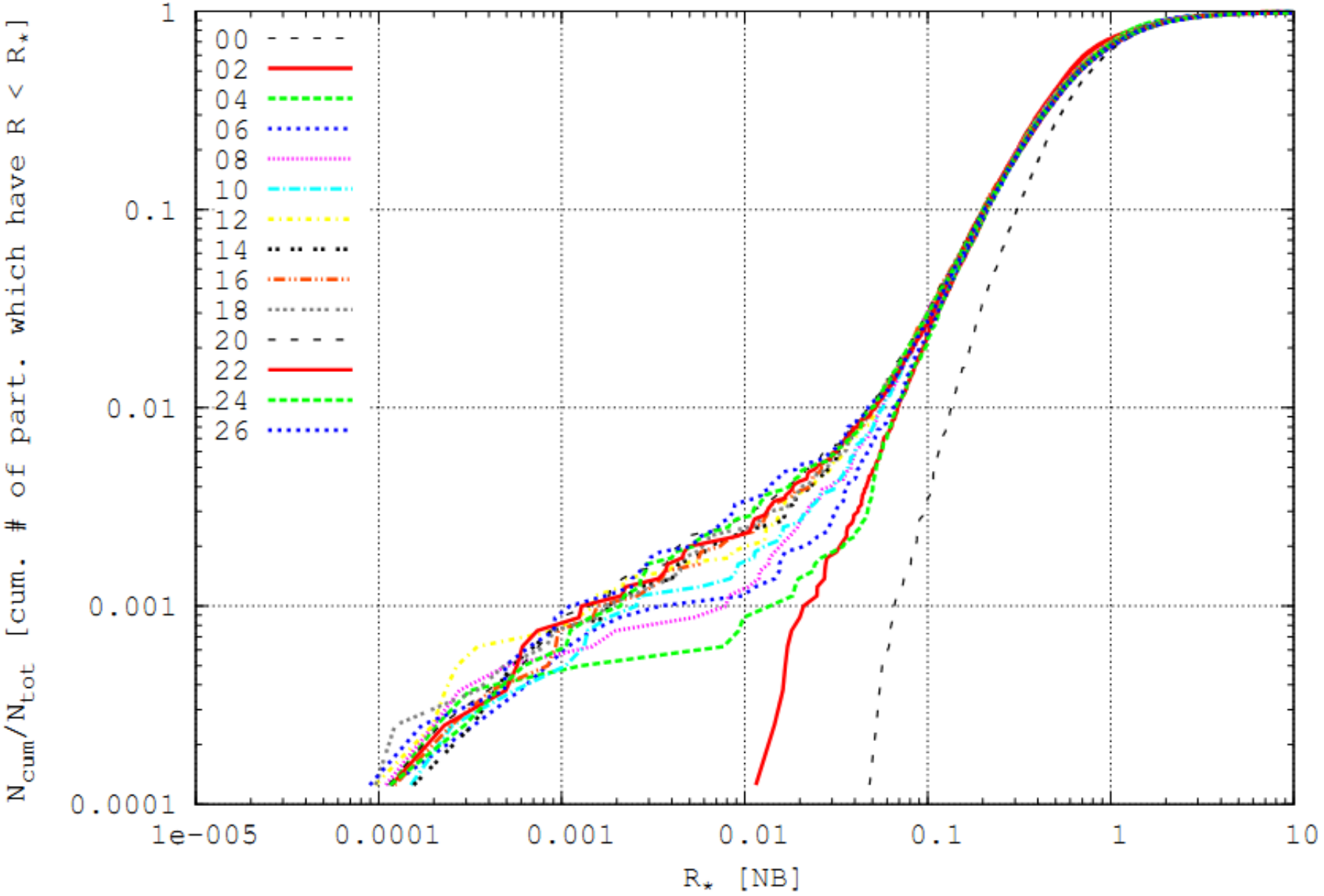

Initial Condition

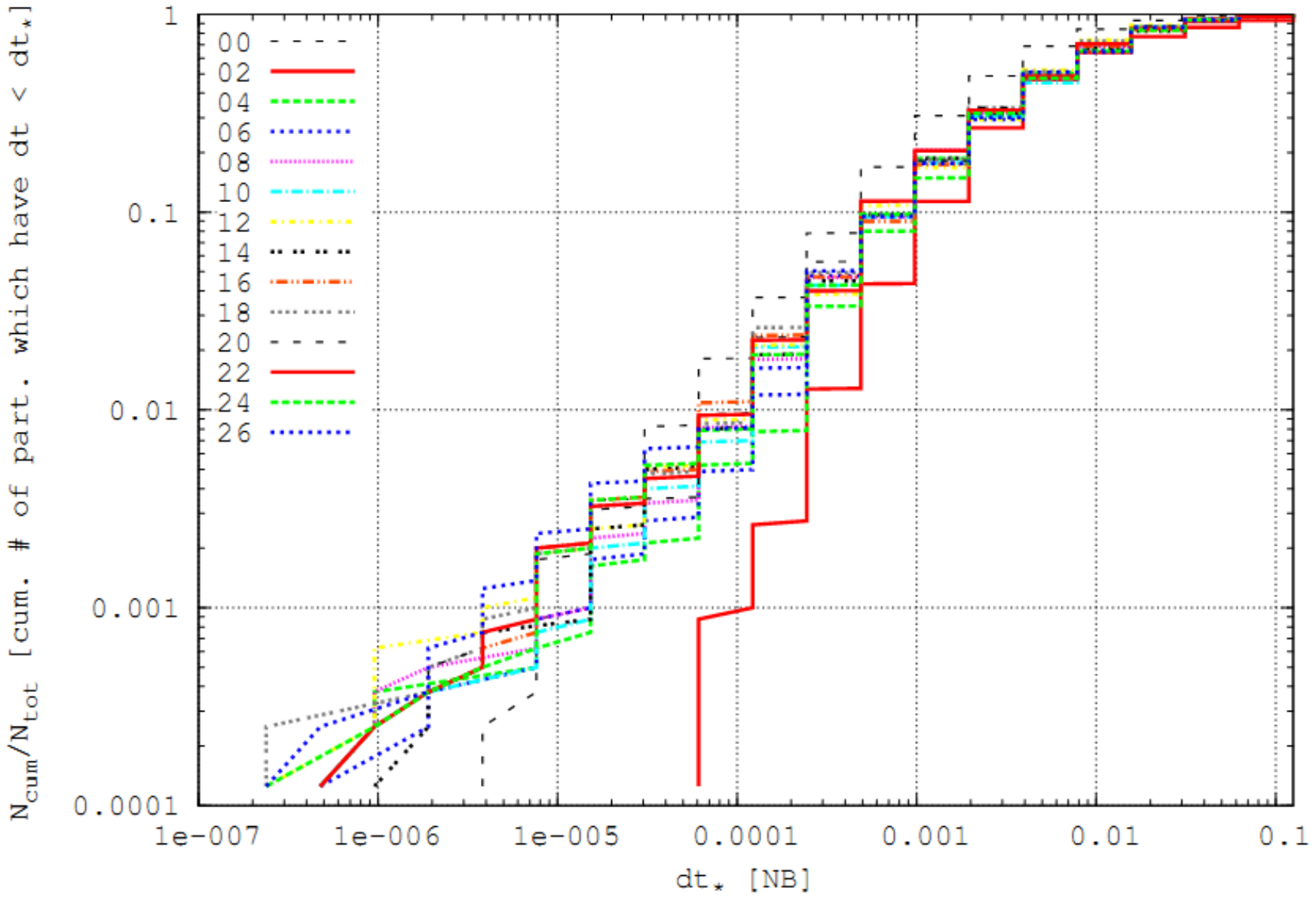

Our φGRAPE/GPU (parallel) N-body code

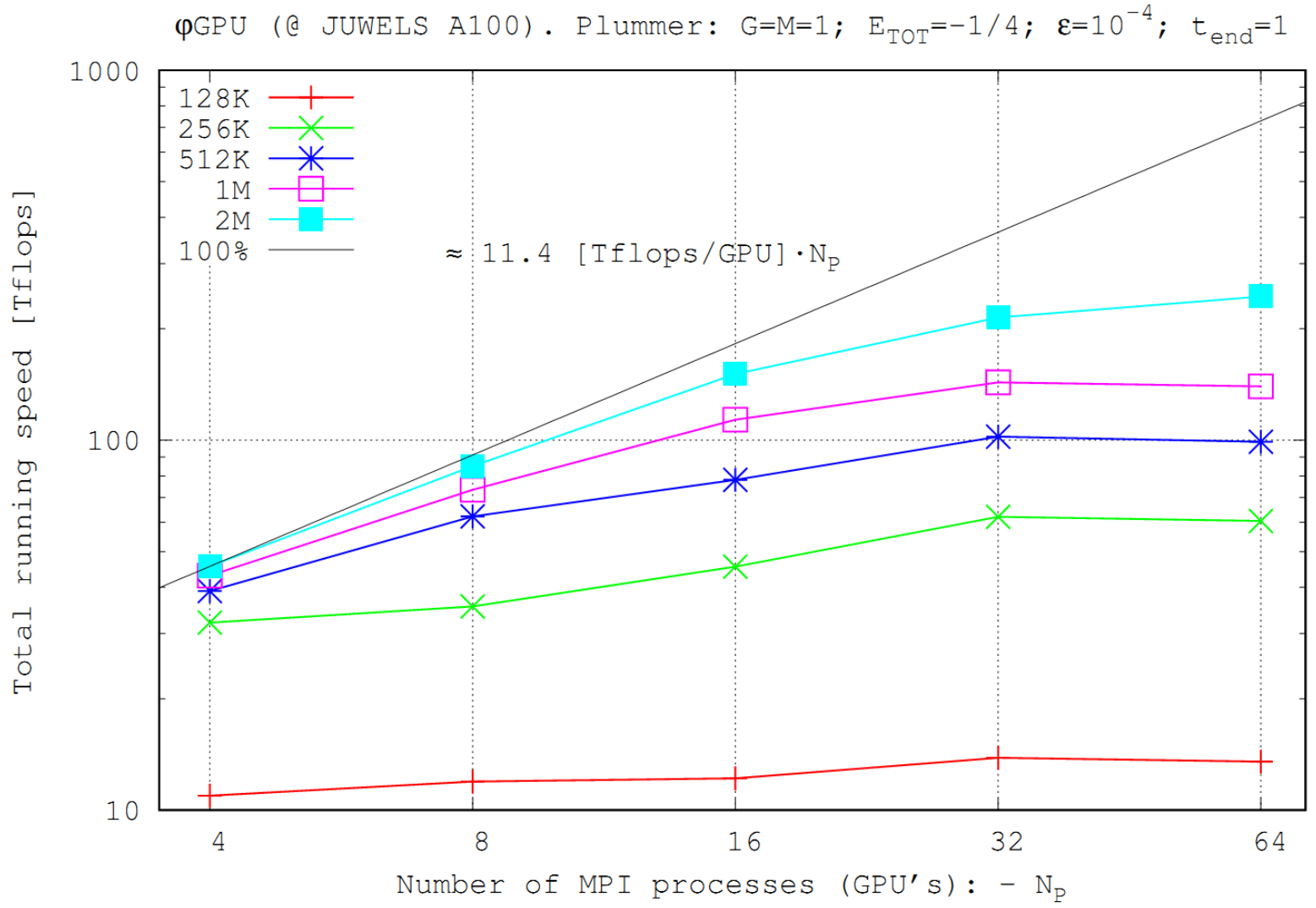

Our φGRAPE/GPU (parallel) N-body code

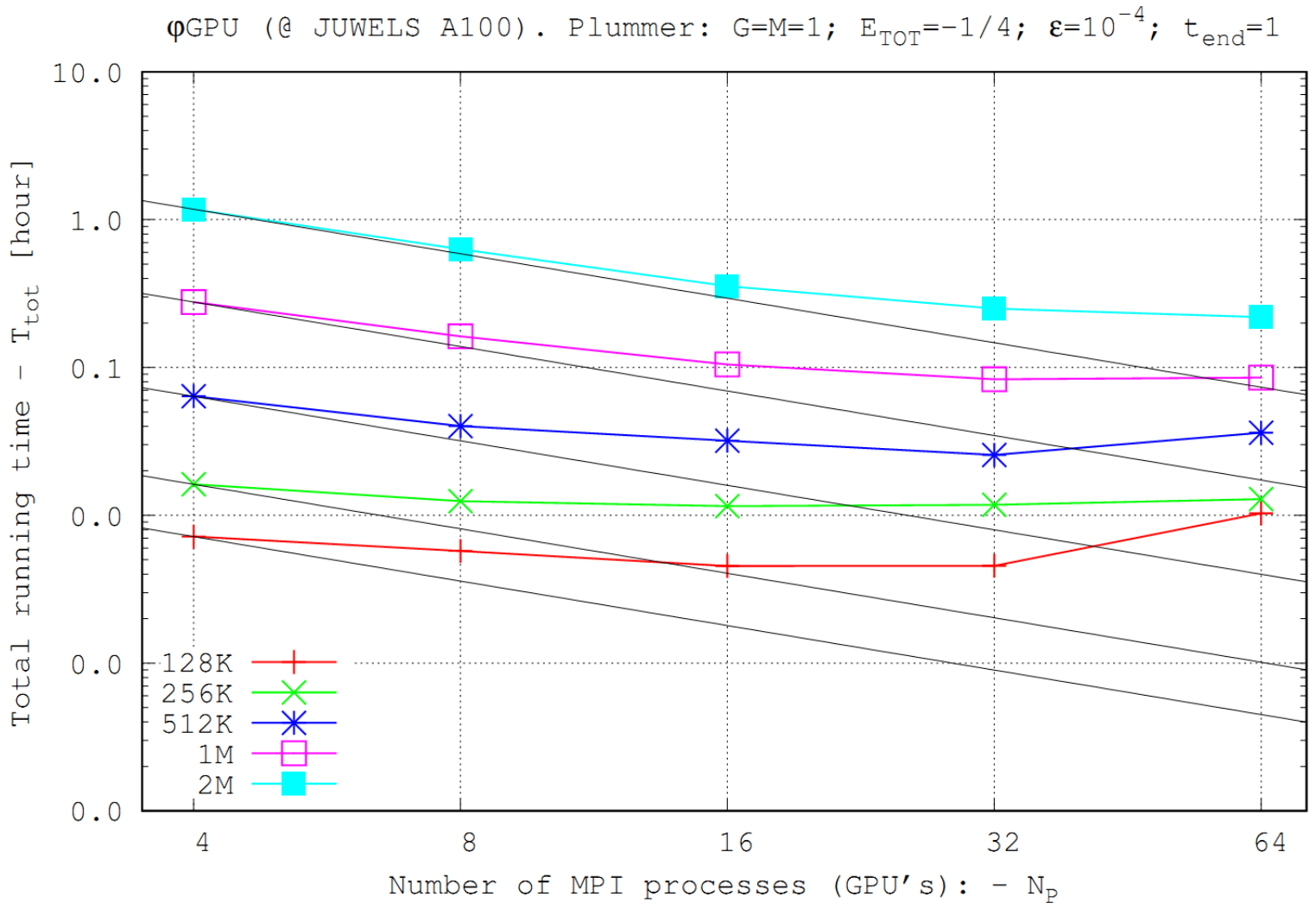

Our φGRAPE/GPU (parallel) N-body code

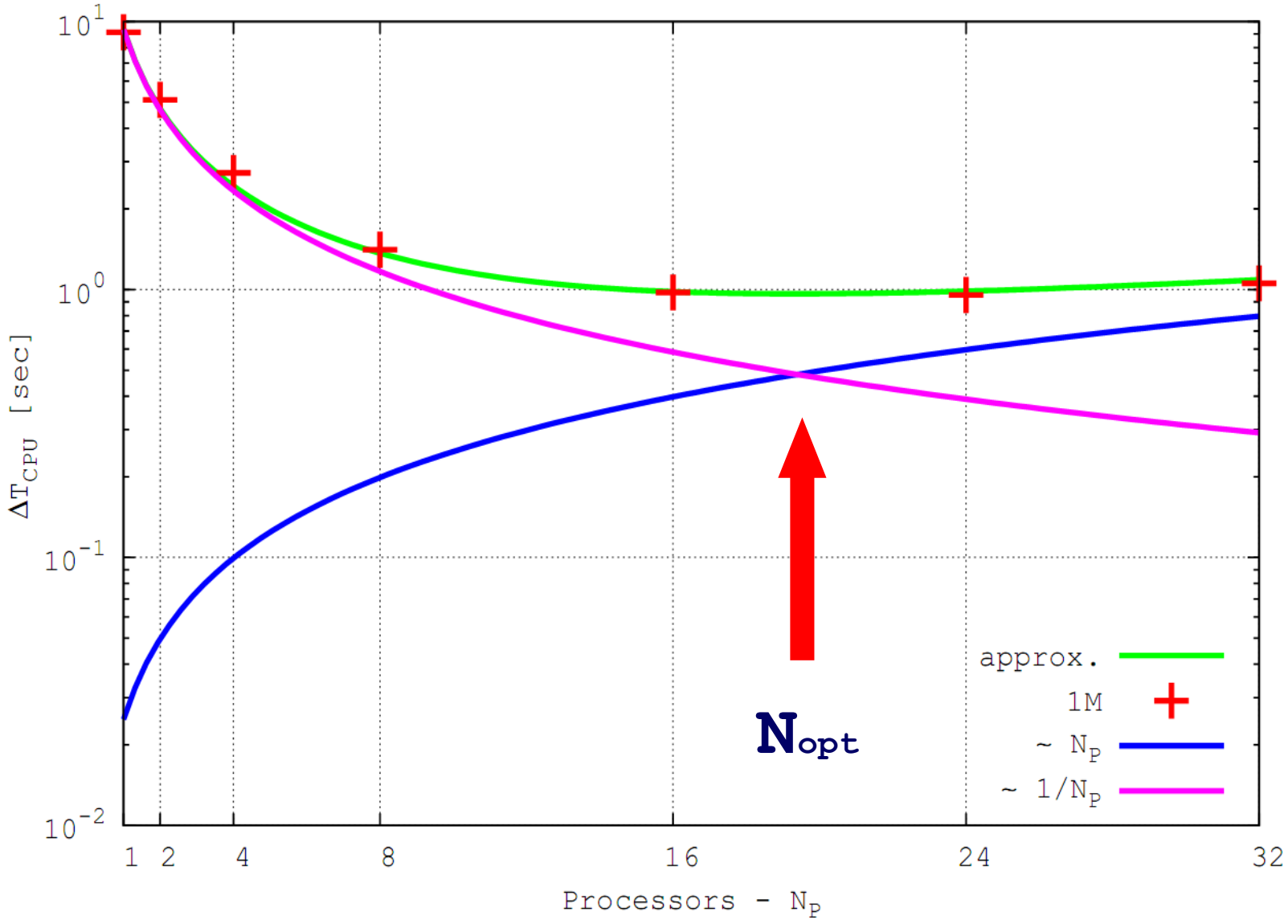

Our φGRAPE/GPU (parallel) N-body code

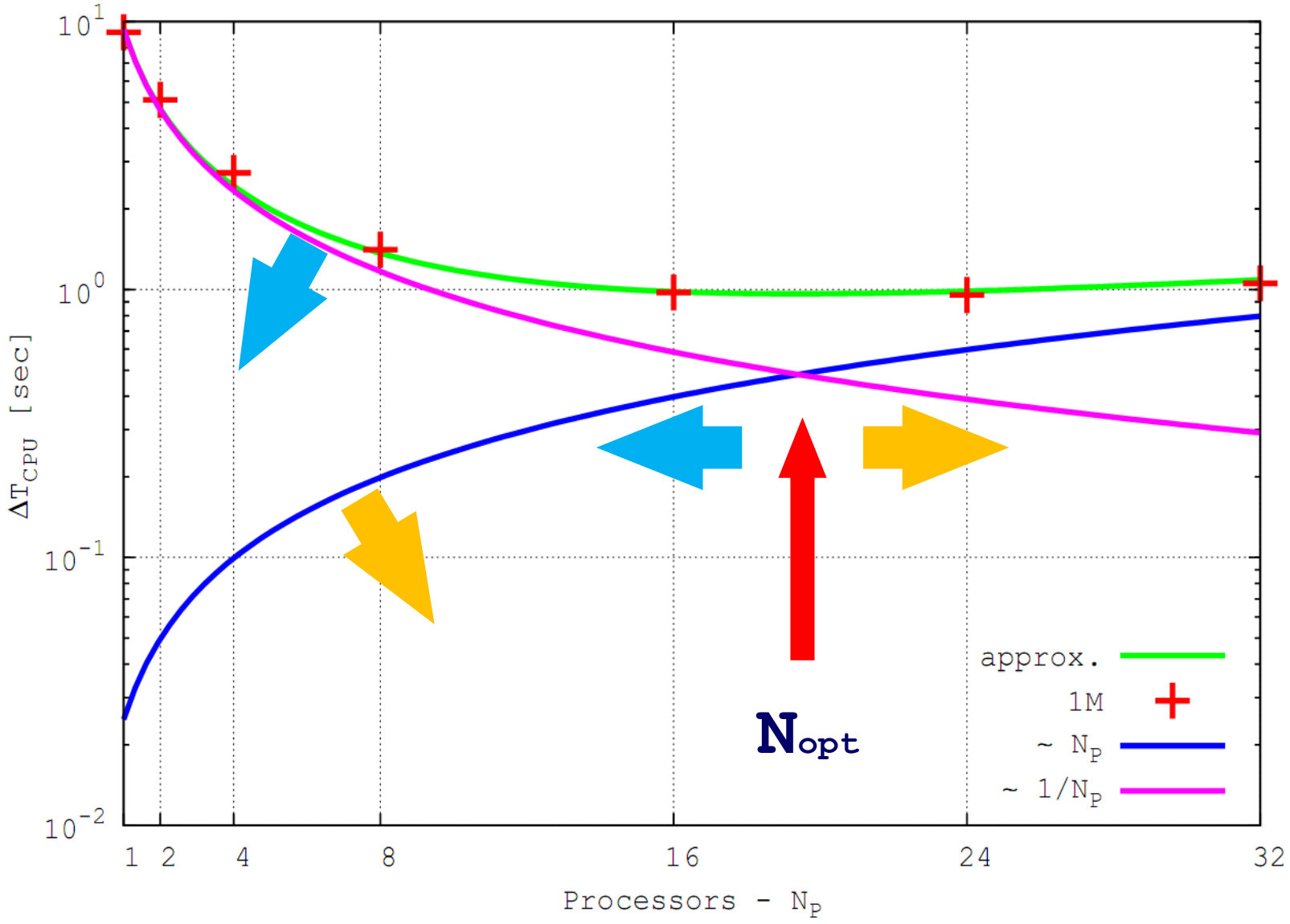

φGPU current usage/results

$$A^{(k)} = \left(|a^{(k-1)}||a^{(k+1)}| + |a^{(k)}|^2 \right)^{1/2}$$

mass distr.: Low mass + High mass.

$$\Delta t = \eta \left(\frac{A^{(1)}}{A^{(p-2)}} \right)^{1/(p-3)}$$

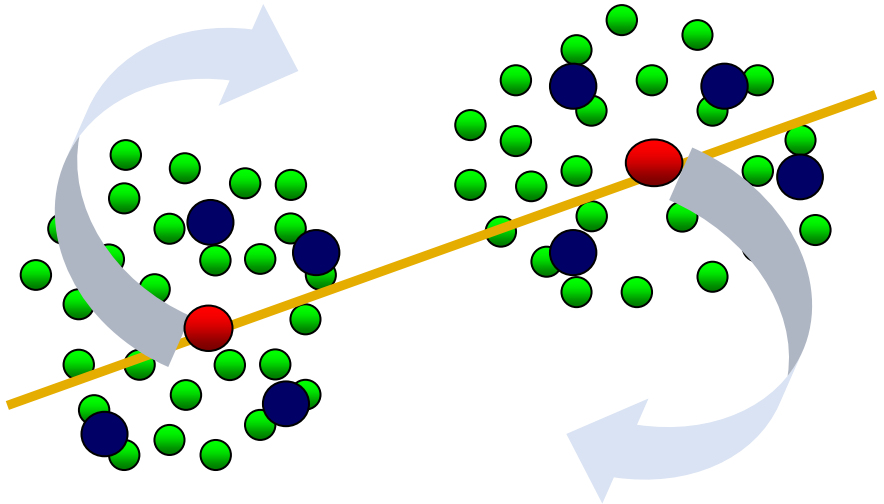

$$\epsilon_{ij}^2 = (\epsilon_i^2 + \epsilon_j^2)/2,$$

$$\frac{d\mathbf{v}}{dt} = -\frac{GM_\bullet}{r^2} \left[(1+\mathcal{A})\mathbf{n_{12}} + \mathcal{B}\mathbf{v_{12}} \right] + \mathcal{O}(1/c^8),$$

PN routine

$$\mathbf{a}_{\rm NoSpin} = \mathbf{a}_{\rm N} + \frac{1}{c^2}\mathbf{a}_{1\mathcal{PN}} + \frac{1}{c^4}\mathbf{a}_{2\mathcal{PN}} + \frac{1}{c^5}\mathbf{a}_{2.5\mathcal{PN}} + \frac{1}{c^6}\mathbf{a}_{3\mathcal{PN}} + \frac{1}{c^7}\mathbf{a}_{3.5\mathcal{PN}} + \mathcal{O}\left(\frac{1}{c^8}\right),$$

Blanchet 2006

Faye et al. 2006 Tagoshi et al. 2001

$$\mathbf{a}_{\rm Spin} = \mathbf{a}_{\rm NoSpin} + \frac{1}{c^3}\mathbf{a}_{1.5\mathcal{PN},\rm SO} + \frac{1}{c^4}\mathbf{a}_{2\mathcal{PN},\rm SS} + \frac{1}{c^5}\mathbf{a}_{2.5\mathcal{PN},\rm SO},$$

$$\frac{d\mathbf{v}}{dt} = -\frac{Gm}{r^2}[(1+A)\mathbf{n} + B\mathbf{v}].$$

Kupi et al. 2006; Berentzen et al. 2009; Brem 2013;
Sobolenko et al. 2016

$$\frac{d\vec{v}}{dt} = -\frac{Gm}{r^2}[(1+A)\vec{n} + B\vec{v}].$$

$$\begin{aligned}
A =& \frac{1}{c^2}\left\{-\frac{3\dot{r}^2\eta}{2} + v^2 + 3\eta v^2 - \frac{Gm}{r}(4+2\eta)\right\} \\
&+\frac{1}{c^4}\left\{\frac{15\dot{r}^4\eta}{8} - \frac{45\dot{r}^4\eta^2}{8} - \frac{9\dot{r}^2\eta v^2}{2} + 6\dot{r}^2\eta^2 v^2 + 3\eta v^4 - 4\eta^2 v^4\right. \\
&\left. + \frac{Gm}{r}(-2\dot{r}^2 - 25\dot{r}^2\eta - 2\dot{r}^2\eta^2 - \frac{13\eta v^2}{2} + 2\eta^2 v^2) + \frac{G^2m^2}{r^2}(9 + \frac{87\eta}{4})\right\} \\
&+\frac{1}{c^5}\left\{-\frac{24\dot{r}\eta v^2}{5}\frac{Gm}{r} - \frac{136\dot{r}\eta}{15}\frac{G^2m^2}{r^2}\right\} \\
&+\frac{1}{c^6}\left\{-\frac{35\dot{r}^6\eta}{16} + \frac{175\dot{r}^6\eta^2}{16} - \frac{175\dot{r}^6\eta^3}{16} + \frac{15\dot{r}^4\eta v^2}{2} - \frac{135\dot{r}^4\eta^2 v^2}{4} + \frac{255\dot{r}^4\eta^3 v^2}{8}\right. \\
&- \frac{15\dot{r}^2\eta v^4}{2} + \frac{237\dot{r}^2\eta^2 v^4}{8} - \frac{45\dot{r}^2\eta^3 v^4}{2} + \frac{11\eta v^6}{4} - \frac{49\eta^2 v^6}{4} + 13\eta^3 v^6 \\
&+ \frac{Gm}{r}(79\dot{r}^4\eta - \frac{69\dot{r}^4\eta^2}{2} - 30\dot{r}^4\eta^3 - 121\dot{r}^2\eta v^2 + 16\dot{r}^2\eta^2 v^2 + 20\dot{r}^2\eta^3 v^2 + \frac{75\eta v^4}{4} \\
&+ 8\eta^2 v^4 - 10\eta^3 v^4) \\
&+ \frac{G^2m^2}{r^2}(\dot{r}^2 + \frac{22717\dot{r}^2\eta}{168} + \frac{11\dot{r}^2\eta^2}{8} - 7\dot{r}^2\eta^3 + \frac{615\dot{r}^2\eta\pi^2}{64} - \frac{20827\eta v^2}{840} + \eta^3 v^2 \\
&- \frac{123\eta\pi^2 v^2}{64}) \\
&\left. + \frac{G^3m^3}{r^3}(-16 - \frac{1399\eta}{12} - \frac{71\eta^2}{2} + \frac{41\eta\pi^2}{16})\right\} \\
&+\frac{1}{c^7}\left\{\frac{Gm}{r}(\frac{366}{35}\eta v^4 + 12\eta^2 v^4 - 114 v^2\eta\dot{r}^2 - 12\eta^2 v^2\dot{r}^2 + 112\eta\dot{r}^4)\right. \\
&+ \frac{G^2m^2}{r^2}(\frac{692}{35}\eta v^2 - \frac{724}{15}v^2\eta^2 + \frac{294}{5}\eta\dot{r}^2 + \frac{376}{5}\eta^2\dot{r}^2) \\
&\left. + \frac{G^3m^3}{r^3}(\frac{3956}{35}\eta + \frac{184}{5}\eta^2)\right\}
\end{aligned}$$

$$\begin{aligned}
B =& \frac{1}{c^2}\{-4\dot{r} + 2\dot{r}\eta\} \\
&+\frac{1}{c^4}\left\{\frac{9\dot{r}^3\eta}{2} + 3\dot{r}^3\eta^2 - \frac{15\dot{r}\eta v^2}{2} - 2\dot{r}\eta^2 v^2 + \frac{Gm}{r}(2\dot{r} + \frac{41\dot{r}\eta}{2} + 4\dot{r}\eta^2)\right\} \\
&+\frac{1}{c^5}\left\{\frac{8\eta v^2}{5}\frac{Gm}{r} + \frac{24\eta}{5}\frac{G^2m^2}{r^2}\right\} \\
&+\frac{1}{c^6}\left\{-\frac{45\dot{r}^5\eta}{8} + 15\dot{r}^5\eta^2 + \frac{15\dot{r}^5\eta^3}{4} + 12\dot{r}^3\eta v^2 - \frac{111\dot{r}^3\eta^2 v^2}{4} - 12\dot{r}^3\eta^3 v^2 - \frac{65\dot{r}\eta v^4}{8}\right. \\
&\left. + 19\dot{r}\eta^2 v^4 + 6\dot{r}\eta^3 v^4\right. \\
&+ \frac{Gm}{r}(\frac{329\dot{r}^3\eta}{6} + \frac{59\dot{r}^3\eta^2}{2} + 18\dot{r}^3\eta^3 - 15\dot{r}\eta v^2 - 27\dot{r}\eta^2 v^2 - 10\dot{r}\eta^3 v^2) \\
&\left. + \frac{G^2m^2}{r^2}(-4\dot{r} - \frac{5849\dot{r}\eta}{840} + 25\dot{r}\eta^2 + 8\dot{r}\eta^3 - \frac{123\dot{r}\eta\pi^2}{32})\right\} \\
&+\frac{1}{c^7}\left\{\frac{Gm}{r}(-\frac{626}{35}\eta v^4 - \frac{12}{5}\eta^2 v^4 + \frac{678}{5}\eta v^2\dot{r}^2 + \frac{12}{5}\eta^2 v^2\dot{r}^2 - 120\eta\dot{r}^4)\right. \\
&+ \frac{G^2m^2}{r^2}(\frac{164}{21}\eta v^2 + \frac{148}{5}\eta^2 v^2 - \frac{82}{3}\eta\dot{r}^2 - \frac{848}{15}\eta^2\dot{r}^2) \\
&\left. + \frac{G^3m^3}{r^3}(-\frac{1060}{21}\eta - \frac{104}{5}\eta^2)\right\}
\end{aligned}$$

L. Blanchet. Gravitational Radiation from Post-Newtonian Sources and Inspiralling Compact Binaries. *Living Reviews in Relativity*, 9:4–+, June 2006.

$$\frac{d\vec{v}}{dt} = \vec{B}_{\mathrm{NoSpin}} + \frac{1}{c^2}\vec{B}_{1.5PNSO} + \frac{1}{c^4}\vec{B}_{2PNSS} + \frac{1}{c^4}\vec{B}_{2.5PNSO}$$

$$h^{ij} = \frac{2G\mu}{Dc^4}\left[Q^{ij} + P^{0.5}Q^{ij} + PQ^{ij} + PQ^{ij}_{\rm SO} + P^{1.5}Q^{ij} + ...\right]_{\rm TT},$$

$$Q^{ij} = 2\left[v^i v^j - \frac{Gm}{r}n^i n^j\right]$$

$$h^{ij} \approx \frac{4G\mu}{Dc^4}\left[v^i v^j - \frac{Gm}{r}n^i n^j\right]$$

$$\begin{aligned}
\epsilon^{ij}_{+} &= \hat{e}^i_y \hat{e}^j_y - \hat{e}^i_x \hat{e}^j_x \\
\epsilon^{ij}_{\times} &= \hat{e}^i_x \hat{e}^j_y + \hat{e}^i_y \hat{e}^j_x,
\end{aligned}$$

$$\begin{aligned}
\hat{e}_x &= (1,0,0) \\
\hat{e}_y &= (0,1,0) \\
\hat{e}_z &= (0,0,1),
\end{aligned}$$

$$\epsilon^{ij}_{+} = \begin{pmatrix} 0 & 0 & 0 \\ 0 & 1 & 0 \\ 0 & 0 & -1 \end{pmatrix}$$

$$\epsilon^{ij}_{\times} = \begin{pmatrix} 0 & 0 & 0 \\ 0 & 0 & 1 \\ 0 & 1 & 0 \end{pmatrix}$$

$$\begin{aligned}
h_{+} &= h^{ij}\epsilon^{+}_{ij} \\
h_{\times} &= h^{ij}\epsilon^{\times}_{ij}.
\end{aligned}$$

PHYSICAL REVIEW VOLUME 136, NUMBER 4B 23 NOVEMBER 1964

Gravitational Radiation and the Motion of Two Point Masses

P. C. PETERS*†
California Institute of Technology, Pasadena, California
(Received 2 July 1964)

$$r = a(1-e^2)/(1+e\cos\psi)$$

$$a = -Gm_1m_2/2E,$$

$$L^2 = Gm_1^2m_2^2(m_1+m_2)^{-1}a(1-e^2).$$

$$\left\langle \frac{da}{dt} \right\rangle = -\frac{64}{5}\frac{G^3m_1m_2(m_1+m_2)}{c^5a^3(1-e^2)^{7/2}}\left(1+\frac{73}{24}e^2+\frac{37}{96}e^4\right)$$

$$\left\langle \frac{de}{dt} \right\rangle = -\frac{304}{15}e\frac{G^3m_1m_2(m_1+m_2)}{c^5a^4(1-e^2)^{5/2}}\left(1+\frac{121}{304}e^2\right)$$

T ~ a/(da/dt)

$$\beta = \frac{64}{5}\frac{G^3m_1m_2(m_1+m_2)}{c^5}$$

$$T_c(a_0) = a_0^4/(4\beta)$$

$$T(a_0,e_0) \approx (768/425)T_c(a_0)(1-e_0^2)^{7/2}$$

PN routine

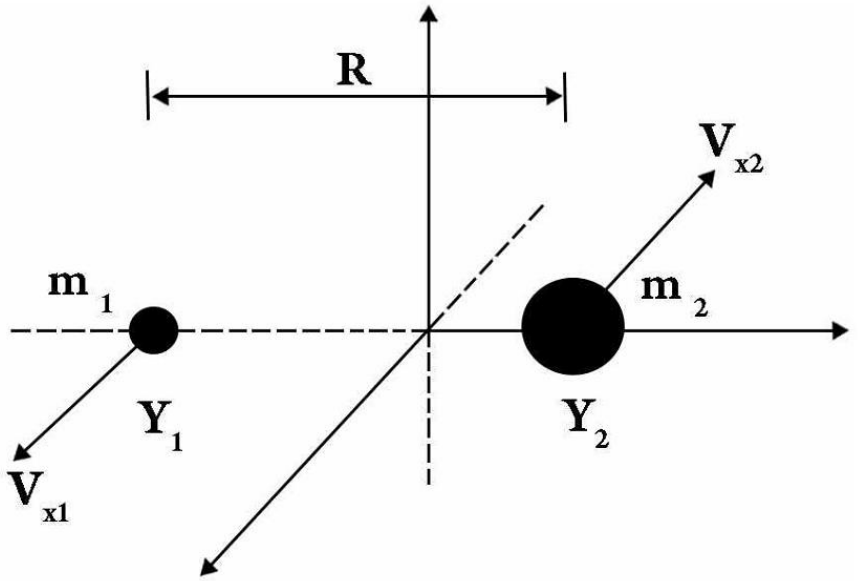

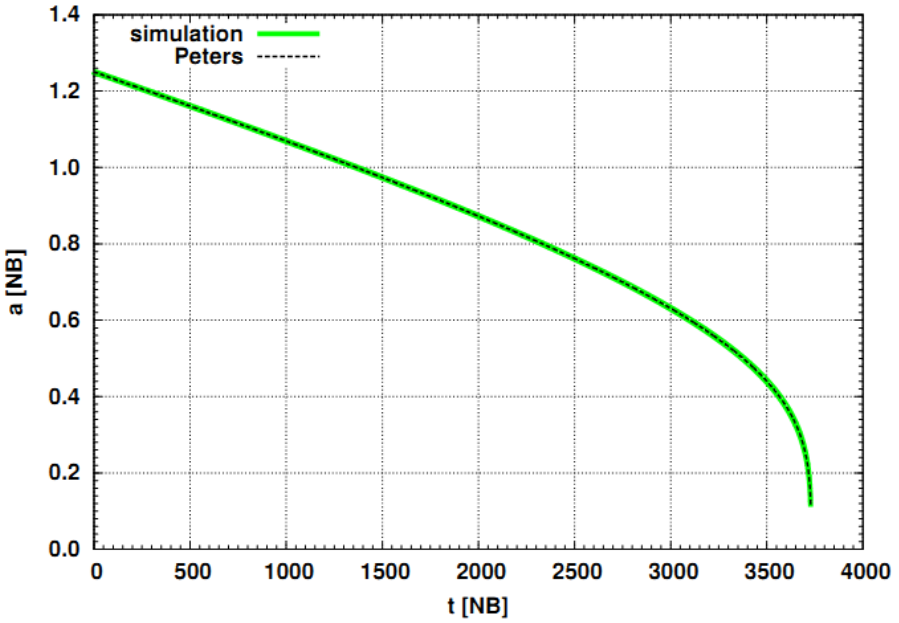

$$M_{\bullet\mathrm{tot}} = 2\ [\mathrm{NB}],\ q = 1,\ R = 1\ [\mathrm{NB}],$$

$$e_0 = 0.6,\ c = 15\ [\mathrm{NB}]\ \text{with just turning on}\ 2.5\mathcal{PN}$$

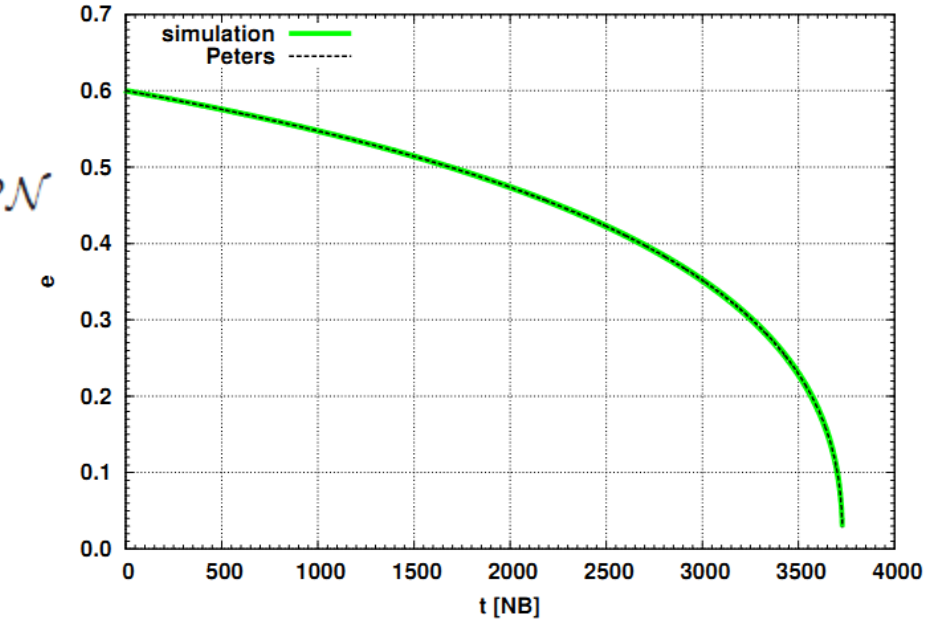

$$\left\langle \frac{da}{dt} \right\rangle = -\frac{64}{5}\frac{G^3 m_1 m_2 (m_1+m_2)}{c^5 a^3 (1-e^2)^{7/2}}\left(1+\frac{73}{24}e^2+\frac{37}{96}e^4\right)$$

$$\left\langle \frac{de}{dt} \right\rangle = -\frac{304}{15}e\frac{G^3 m_1 m_2 (m_1+m_2)}{c^5 a^4 (1-e^2)^{5/2}}\left(1+\frac{121}{304}e^2\right)$$

Double & Triple SMBH evolution in galaxy centers. New hybrid code approaches and performance tests.

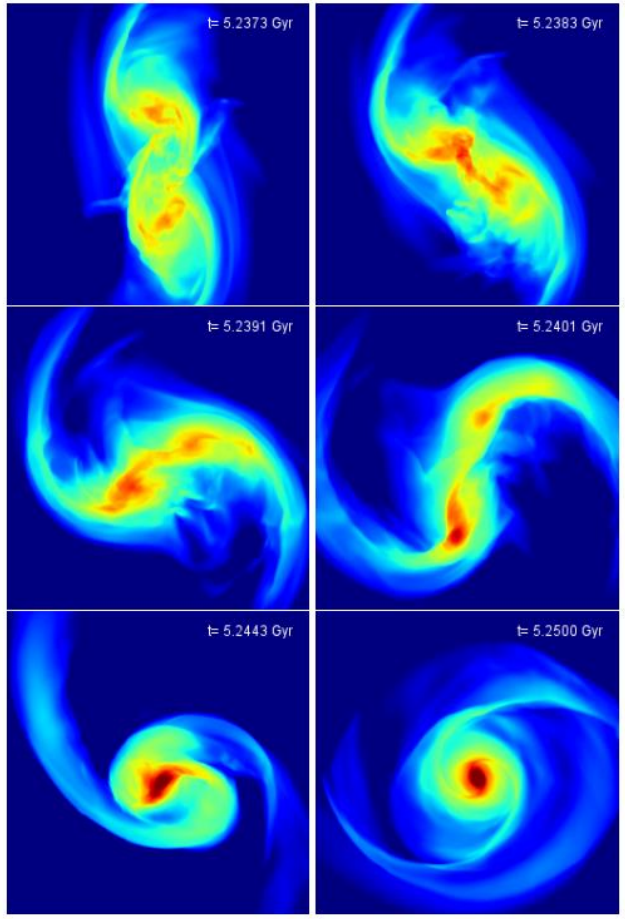

Figure 1. Mass-weighted gas density maps during last pericenter and final merger. The line-of-sight is perpendicular to the orbital plane and the maps are 1.8 kpc wide. While fairly symmetric before the pericenter (top left), the density distribution becomes clearly asymmetric after the pericenter (middle). After the final merger, a thick $\sim 10^9$ $M_\odot$ gaseous nuclear disk is formed (bottom), in which the two SMBHs start orbiting.

1:10 – 1:3 minor merger

Two SMBH's ~10^6 M_o

High accuracy direct summation: ~3 – 6 M Particles!

First time reach the < 1 mpc separation of BBH from initial ~1 kpc scale

<u>Full up to 3.5 PN accurate BBH dynamics!</u>

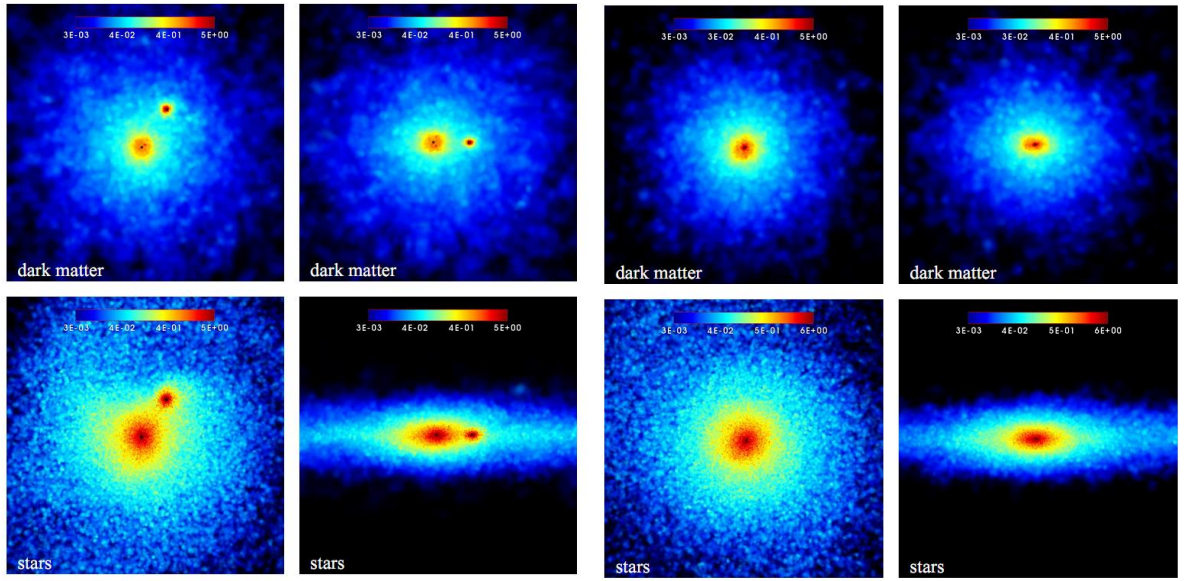

FIG. 1.— Density distribution of the dark matter (top panels) and stellar component (bottom panels) in the $x-y$ (left column) and $y-z$ (right column) planes. The two high density regions are clearly visible around the two SMBHs (black dots) in the center. The size of each box is 4 kpc.

FIG. 3.— Same as in Figure 1 but at $T = 40$ Myr. Both SMBHs are embedded in a single cusp.

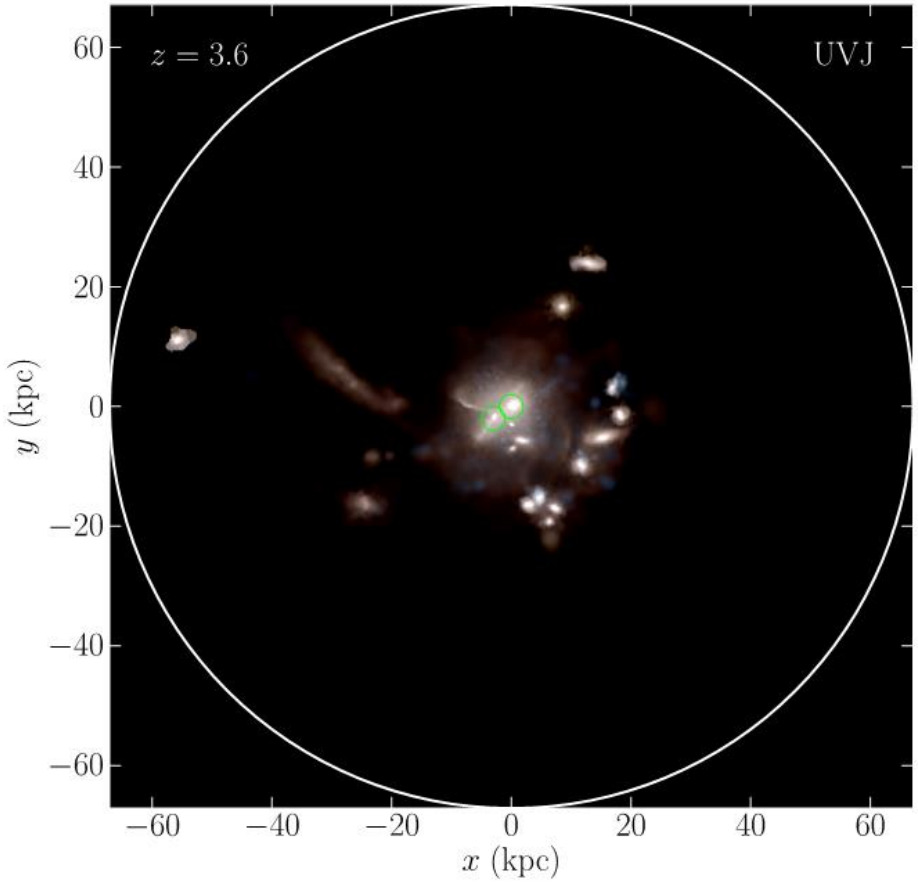
$z = 3.6$
UVJ
y (kpc)
x (kpc)

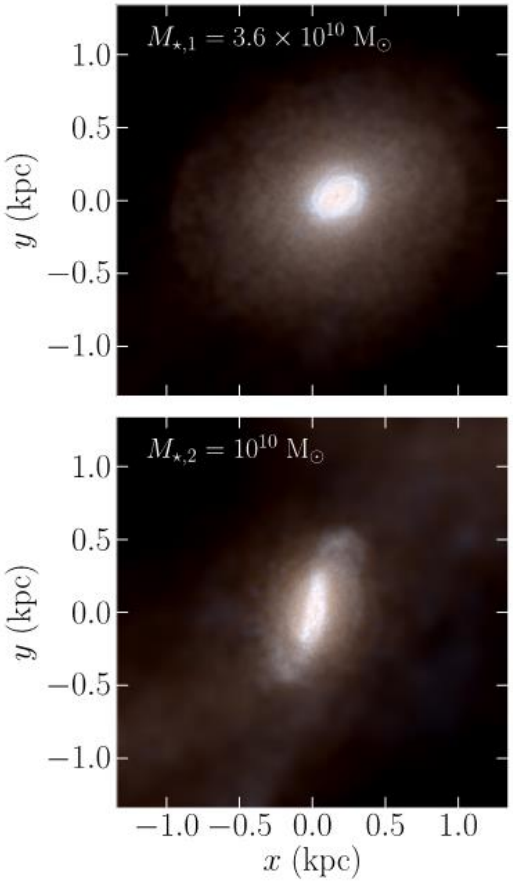
$M_{\star,1} = 3.6 \times 10^{10}$ M$_\odot$
$M_{\star,2} = 10^{10}$ M$_\odot$
y (kpc)
x (kpc)

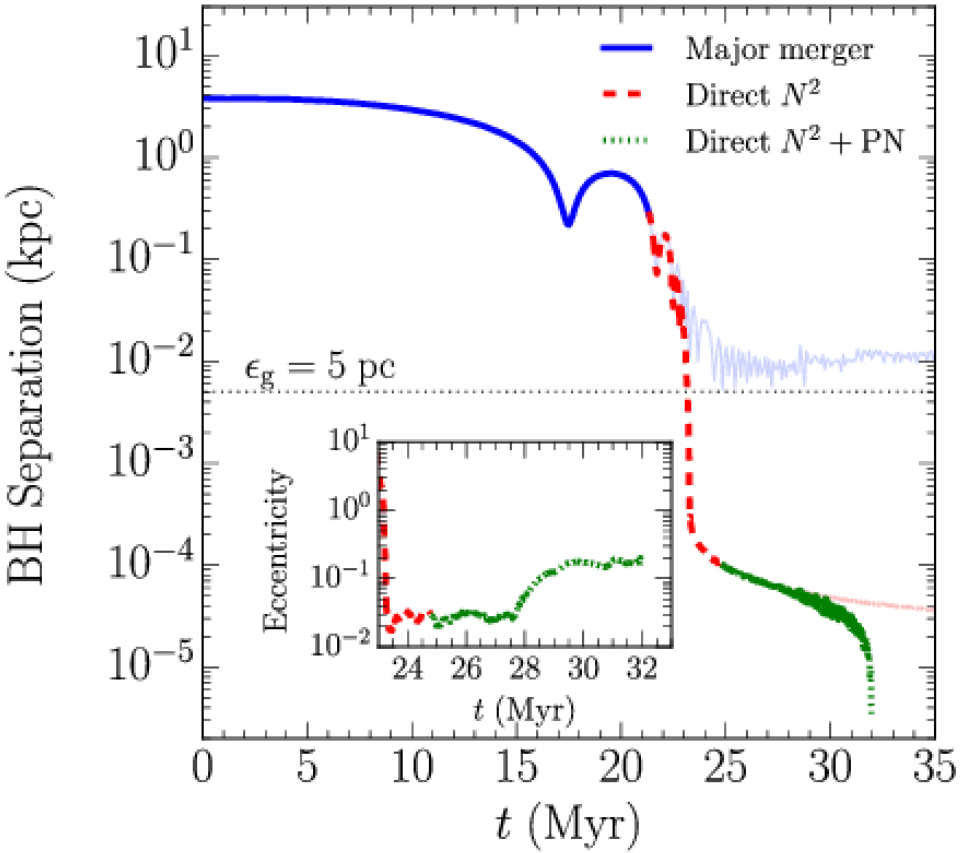
Major merger
Direct N^2
Direct N^2 + PN
$\epsilon_g = 5$ pc
BH Separation (kpc)
Eccentricity
t (Myr)

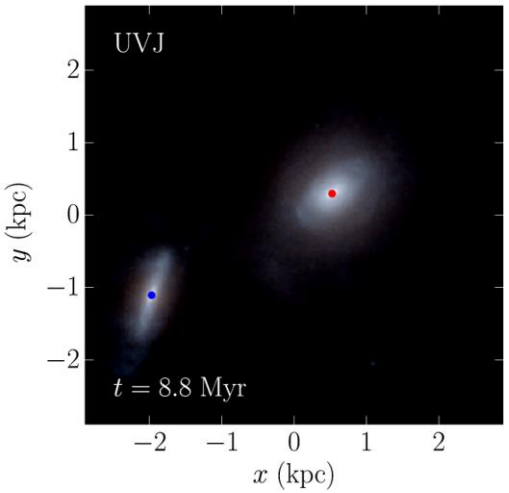
UVJ
$t = 8.8$ Myr
y (kpc)
x (kpc)

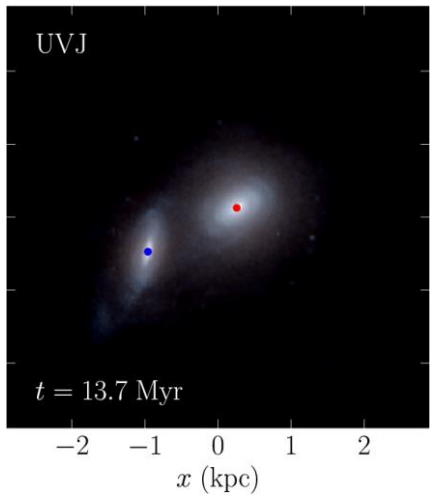
UVJ
$t = 13.7$ Myr
x (kpc)

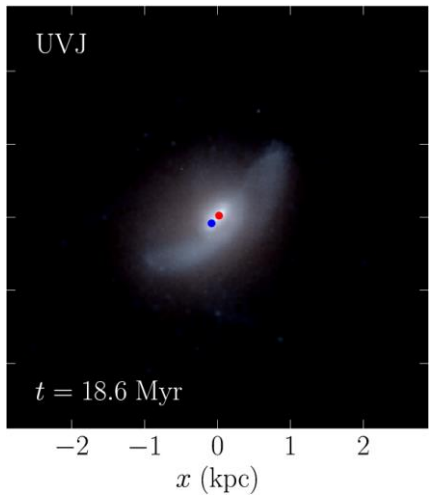
UVJ
$t = 18.6$ Myr
x (kpc)

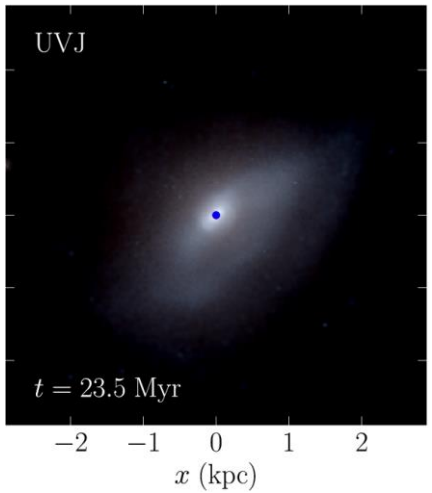
UVJ
$t = 23.5$ Myr
x (kpc)

Direct N-body

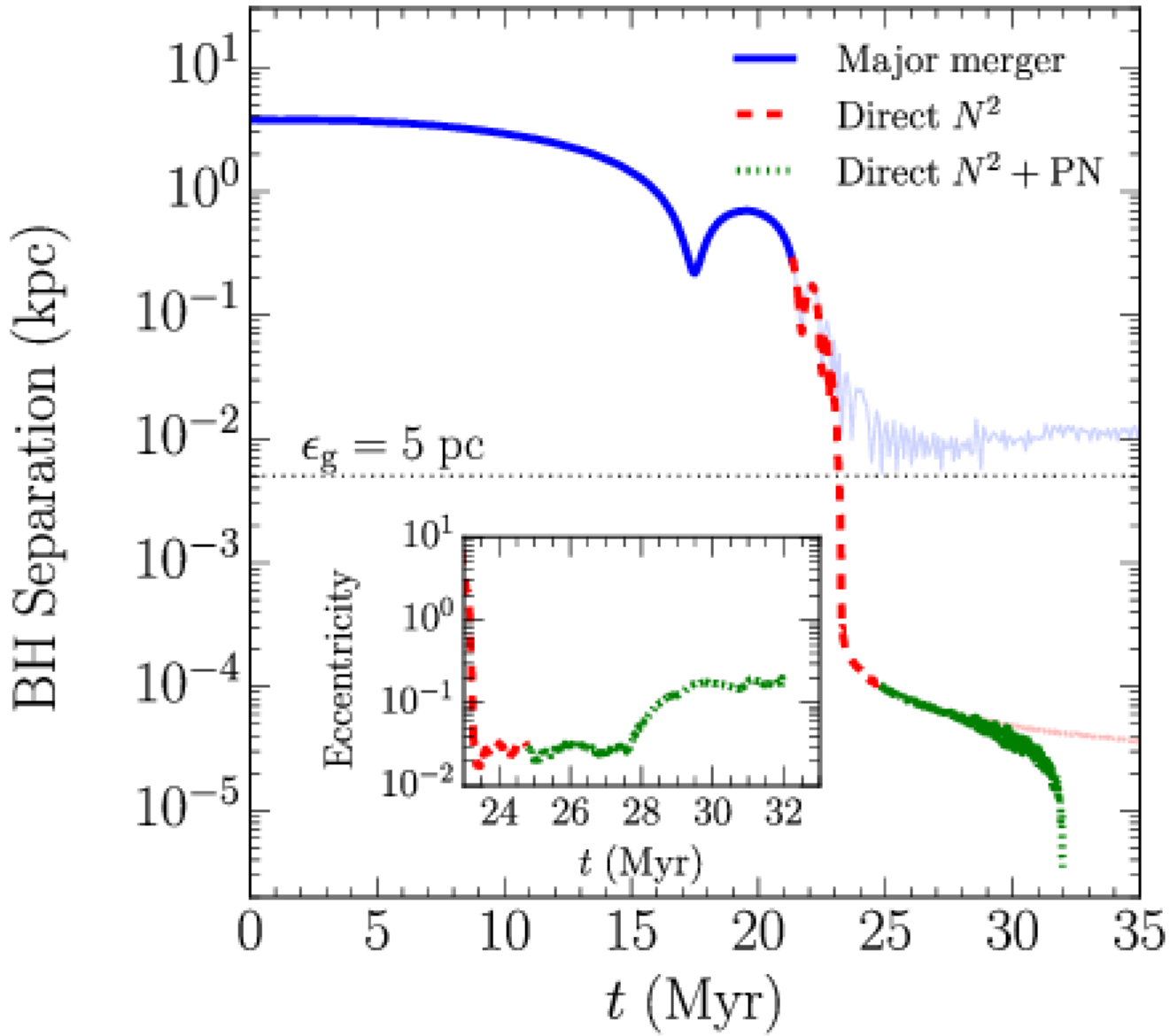

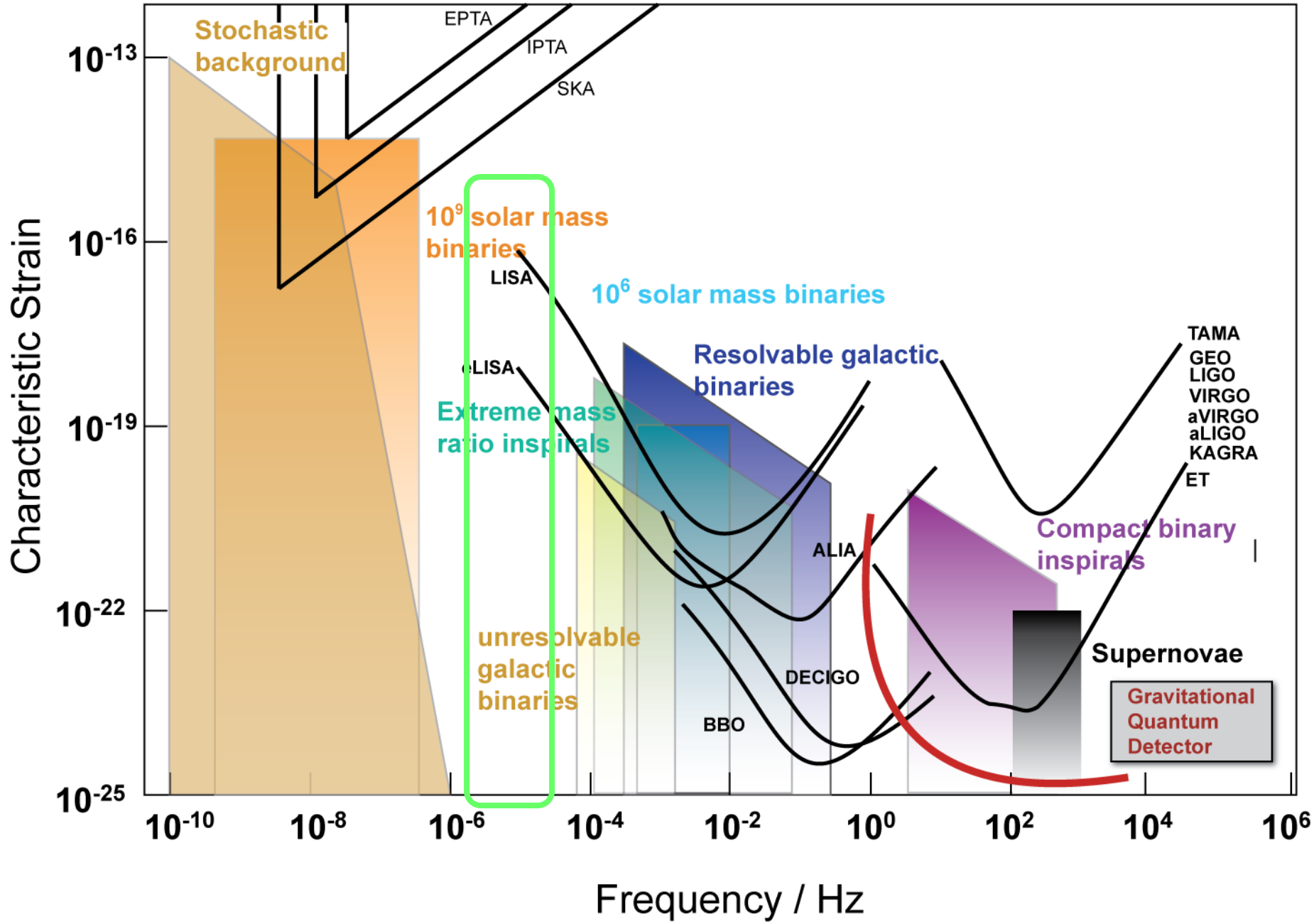
Stochastic background
EPTA
IPTA
SKA
10^9 solar mass binaries
LISA
10^6 solar mass binaries
Resolvable galactic binaries
eLISA
Extreme mass ratio inspirals
TAMA
GEO
LIGO
VIRGO
aVIRGO
aLIGO
KAGRA
ET
ALIA
Compact binary inspirals
unresolvable galactic binaries
DECIGO
BBO
Supernovae
Gravitational Quantum Detector
Characteristic Strain
Frequency / Hz
10^-13
10^-16
10^-19
10^-22
10^-25
10^-10
10^-8
10^-6
10^-4
10^-2
10^0
10^2
10^4
10^6

Series	Galaxy	$M_\bullet$ $[M_\odot]$	$\sigma_\star$ [km s^{-1}]	r_h [pc]	TU [Myr]	LU [kpc]	MU $[M_\odot]$	c $[LU\,TU^{-1}]$
A	M87	6.05×10^9	325	255	3.07	2.95	6.05×10^{11}	320
B	M31	1.63×10^8	169	21.75	1.01	0.42	1.63×10^{10}	733
C	MW	4.6×10^6	103	1.4	0.62	.092	4.6×10^8	2044

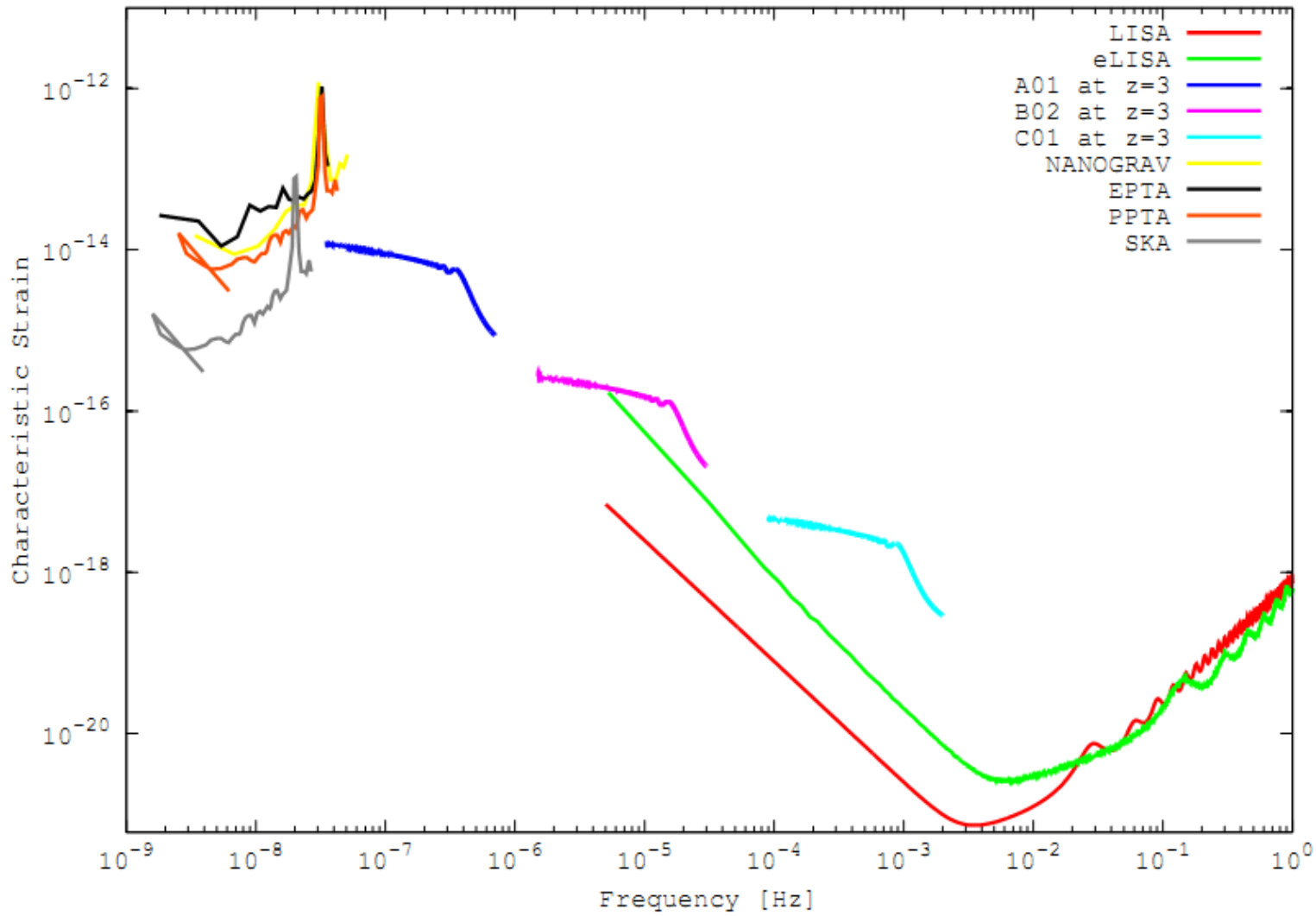

NGC 6240: rare observable SMBH triple system (or not)

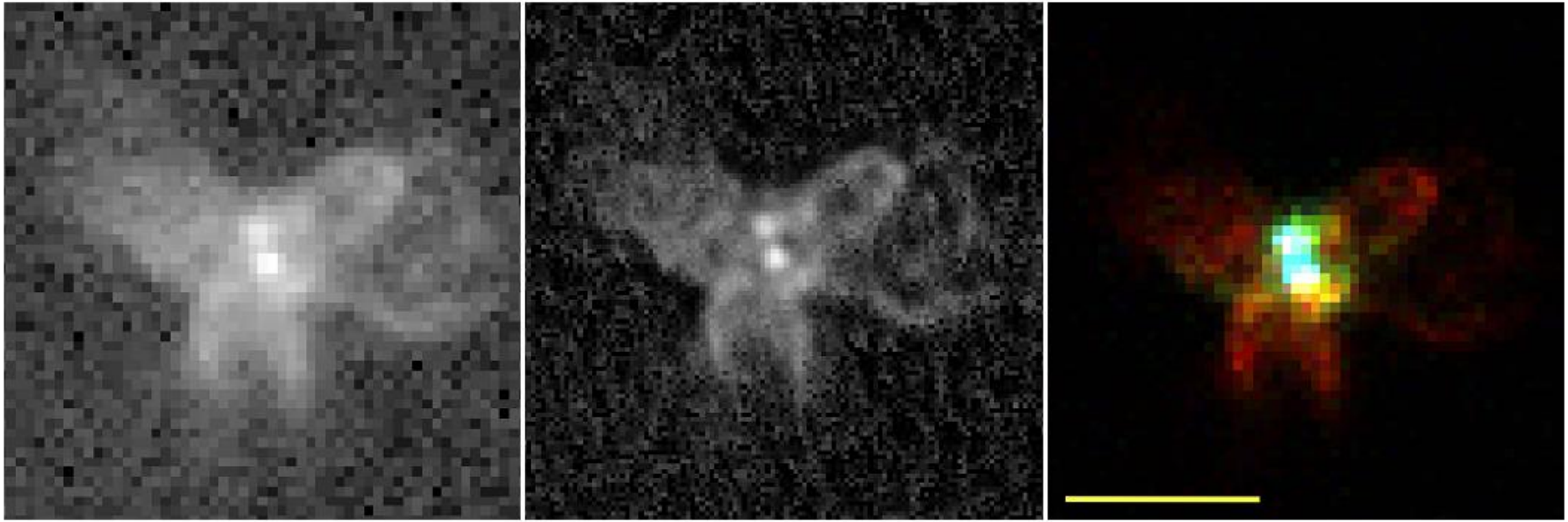

Figure 1. The *Chandra* images of NGC 6240 with binning factor of 0.5: *(left)* the original merged image, *(center)* the deconvolved image, *(right)* the exposure-corrected three-color image, where colors correspond to energies: red: 0.5 – 2.5 keV, green: 2.5 – 6.0 keV, blue: 6.0 – 7.5 keV. The yellow line on right panel is 5 kpc long.

NGC 6240: rare observable SMBH triple system (or not)

Table 1. Basic N-body models.

Physical models						
Run	q	Q	$m_{\bullet 1}$, $10^8 M_\odot$	$m_{\bullet 2}$, $10^8 M_\odot$	M_{*1}, $10^{10} M_\odot$	M_{*2}, $10^{10} M_\odot$
A	0.5	0.01	8.67	4.33	8.67	4.33
B	0.5	0.02	17.34	8.66		
C	0.25	0.01	10.4	2.6	10.4	2.6
D	0.25	0.02	20.8	5.2		

Numerical models	
Run	Characteristic property
B1	Number of particles $N = 10^6$
B2	Randomisation seed
B3	Starting point for PN
B4	Multi-mass prescription

$$\mathrm{MU} = M_* = 1.3 \times 10^{11} M_\odot,$$
$$\mathrm{RU} = \Delta R = 1\,\mathrm{kpc}.$$

$$\mathrm{VU} = \left(\frac{GM}{\Delta R}\right)^{1/2} = 747.6\,\mathrm{km\,s^{-1}},$$

$$\mathrm{TU} = \left(\frac{\Delta R^3}{GM}\right)^{1/2} = 1.3079\,\mathrm{Myr}.$$

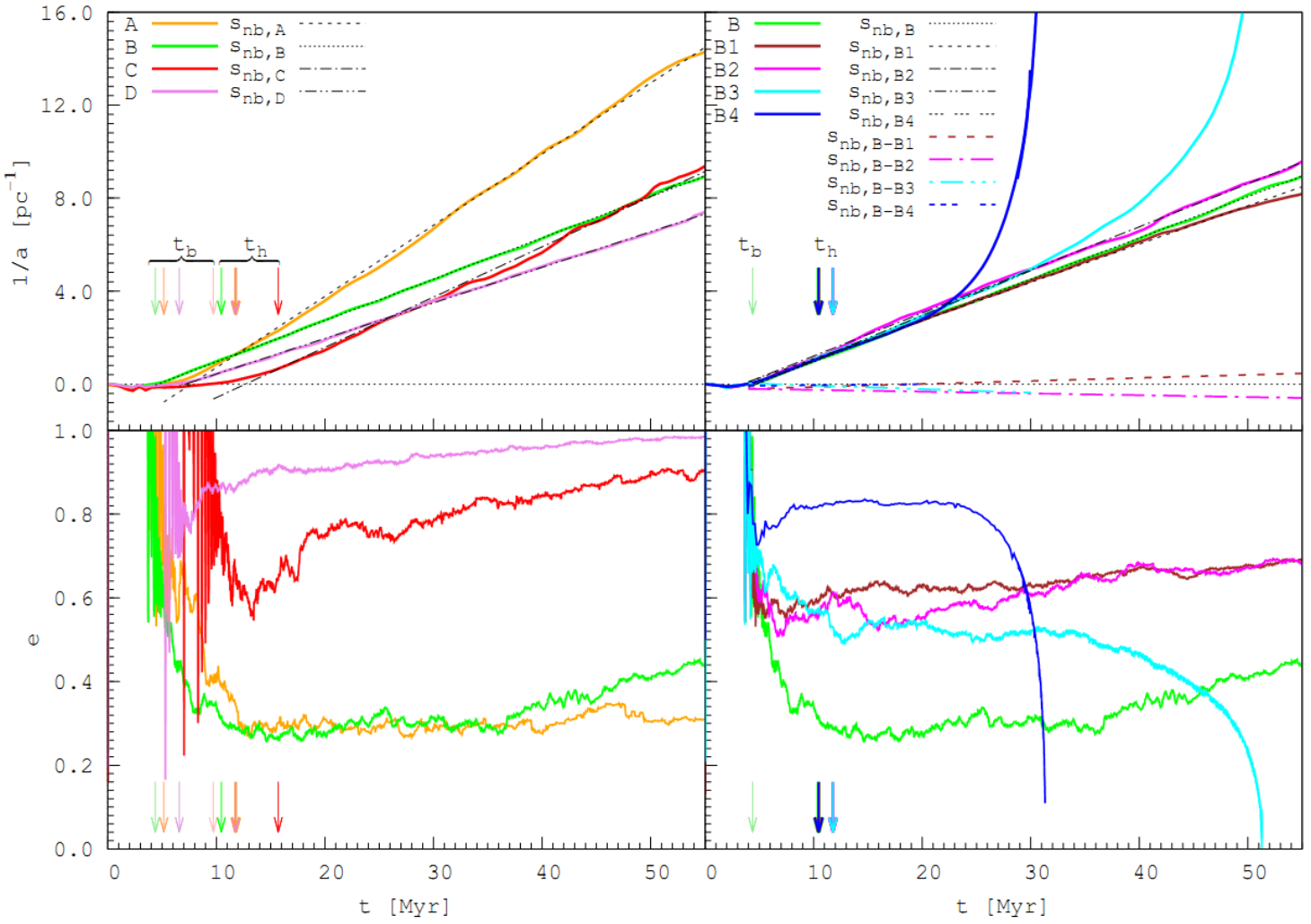

Fig. 3. *From top to bottom*: evolution of inverse semimajor axis and eccentricity in the pure N-body regime for physical models A, B, C, and D (*left*) and numerical models B1-4 (*right*) based on physical model B. It is worth noting that for numerical models B3 and B4 we turned on PN terms from the start of simulations. For numerical models, residuals between model B and models B1-4 are shown as colored dashed lines. Colored arrows mark the time when each system becomes bound t_b (pale color) and then hard t_h (intense color). Colors were chosen according to the main color scheme for each model.

NGC 6240: rare observable SMBH triple system (or not)

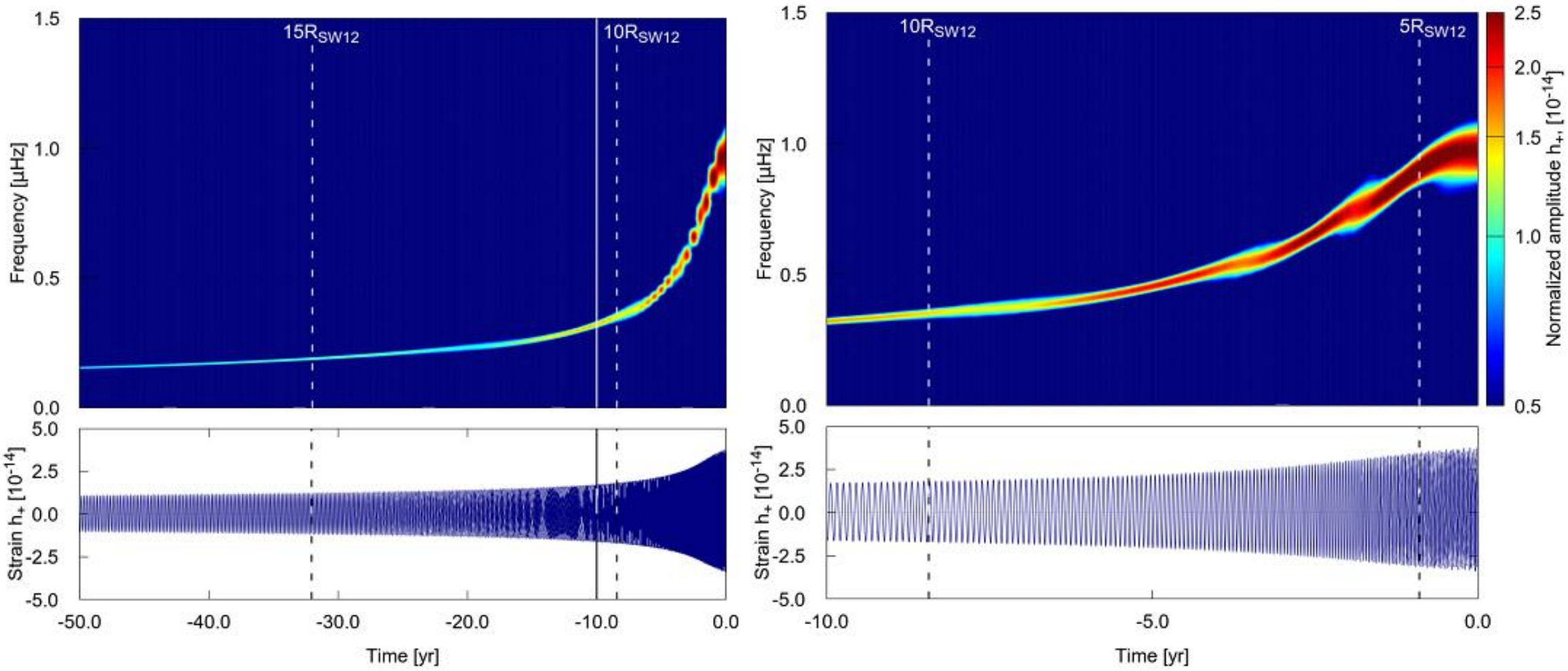

Figure 6. Time-frequency representations (*top*) of the strain data (*bottom*) for predicted gravitational waveforms of h_+ polarisation from SMBHB merging at NGC 6240 (D_L=111.2 Mpc) for the last 50 Myr (*left*) and last 10 Myr (*right*). Major merging is represented by binary component with masses $1.36 \times 10^9 M_\odot$ and $6.8 \times 10^8 M_\odot$ and corresponding mass ratio 2:1. The final separation (due to our $\mathcal{PN}$ routine) is 0.75 mpc. Solid vertical line on the left panel indicates the last 10 Myr of merging. Dashed vertical lines from left to right are indicates binary separation 15, 10 and 5 Schwarzschild radii respectively.

NGC 6240: rare observable SMBH triple system (or not)

A&A 633, A79 (2020)
https://doi.org/10.1051/0004-6361/201936540
© ESO 2020

Astronomy & Astrophysics

NGC 6240: A triple nucleus system in the advanced or final state of merging

W. Kollatschny[1], P. M. Weilbacher[2], M. W. Ochmann[1], D. Chelouche[3], A. Monreal-Ibero[4,5], R. Bacon[6], T. Contini[7]

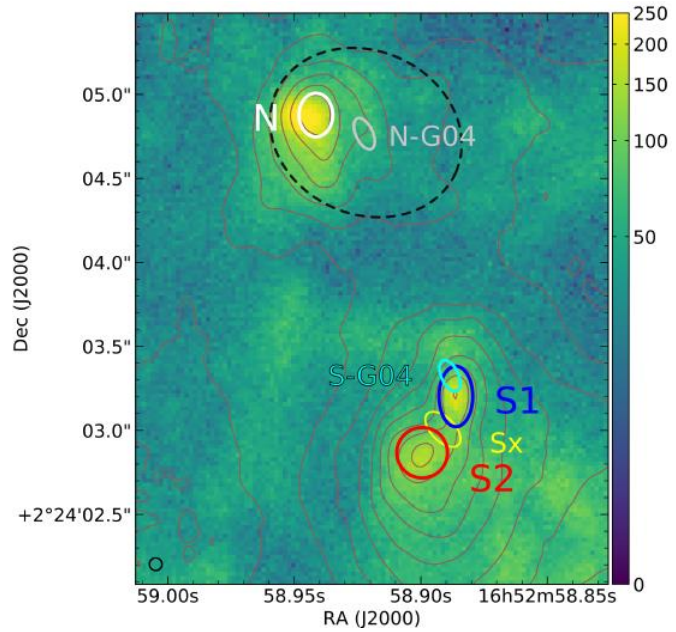

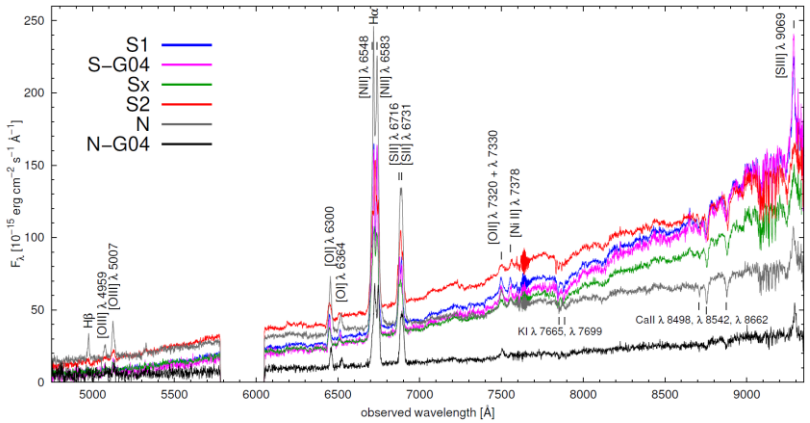

Revisiting the Complex Nuclear Region of NGC 6240 with Chandra

G. Fabbiano[1], A. Paggi[2,3], M. Karovska[1], M. Elvis[1], E. Nardini[4,5], and Junfeng Wang[6]
Published 2020 October 12 • © 2020. The American Astronomical Society. All rights reserved.
The Astrophysical Journal, Volume 902, Number 1

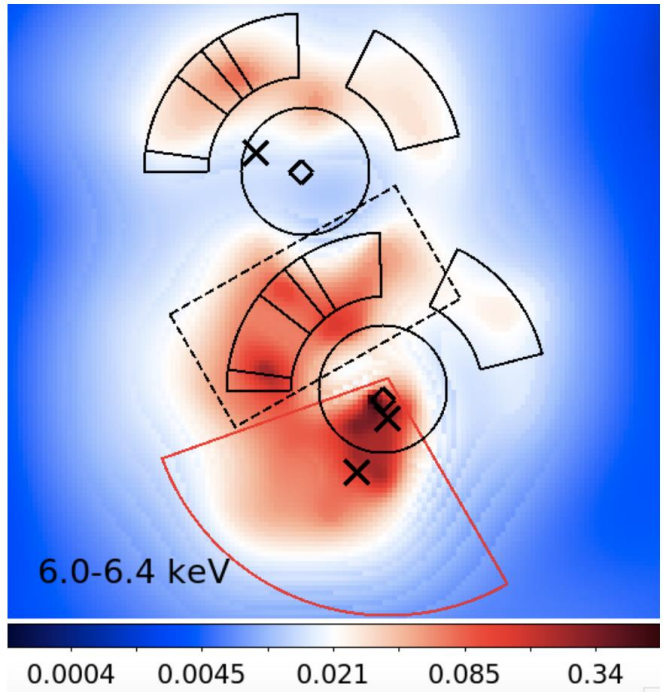

"We do not find strong evidence of X-ray emission associated with the 3rd nucleus proposed by Kollatschny et al. (2020), although this region is associated with the SE excess, and a possible clump of Fe I Ka emission is suggested in this area by the EMC2 reconstruction."

Initial *physical* model

Plummer mass density profiles

$$\rho(r) = \frac{3M}{4\pi r_0^2} \frac{1}{\left(1 + (r_0/r)^2\right)^{\frac{5}{2}}}$$

Between:
$M_* = 0.21 \cdot 10^{10} M_\odot$
***r* = 856 pc**

South2:
$M_\bullet = 0.9 \cdot 10^8 M_\odot$
$M_* = 0.07 \cdot 10^{10} M_\odot$
***r* = 100 pc**

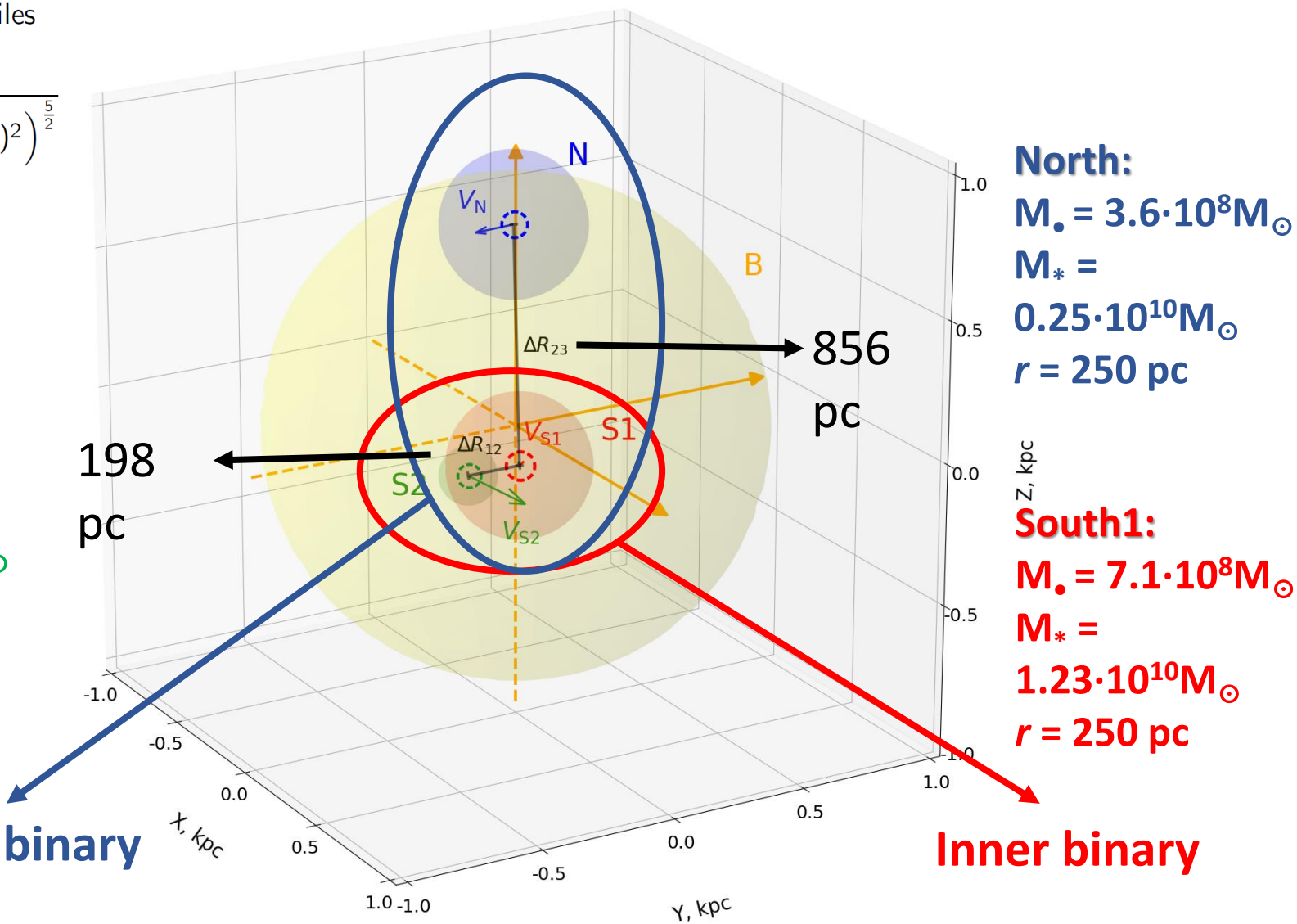

North:
$M_\bullet = 3.6 \cdot 10^8 M_\odot$
$M_* = 0.25 \cdot 10^{10} M_\odot$
***r* = 250 pc**

South1:
$M_\bullet = 7.1 \cdot 10^8 M_\odot$
$M_* = 1.23 \cdot 10^{10} M_\odot$
***r* = 250 pc**

Tacconi+1999, Tecza+2000, Engel+2010, Medling+2011, Kollatschny+2020

N-body code and set of models

- For simulations we used the publicity available ***φ-"GPU" code***† with the blocked hierarchical individual time step scheme and a 4th-order Hermite integration of the equation of motions for all particles (Berczik+2011, Khan+2011)
- Acceleration for *i* partic'

$$\boldsymbol{a}_i = -\sum_{j=1,\, j\neq i}^{N} \frac{G m_j}{(r_{ij}^2 + \varepsilon_{ij}^2)^{3/2}} \boldsymbol{r}_{ij},$$

where ***softening*** is $\varepsilon_{BH}=0$ for BHs and $\varepsilon_p=10^{-4}$ for all another particles.

Physical model

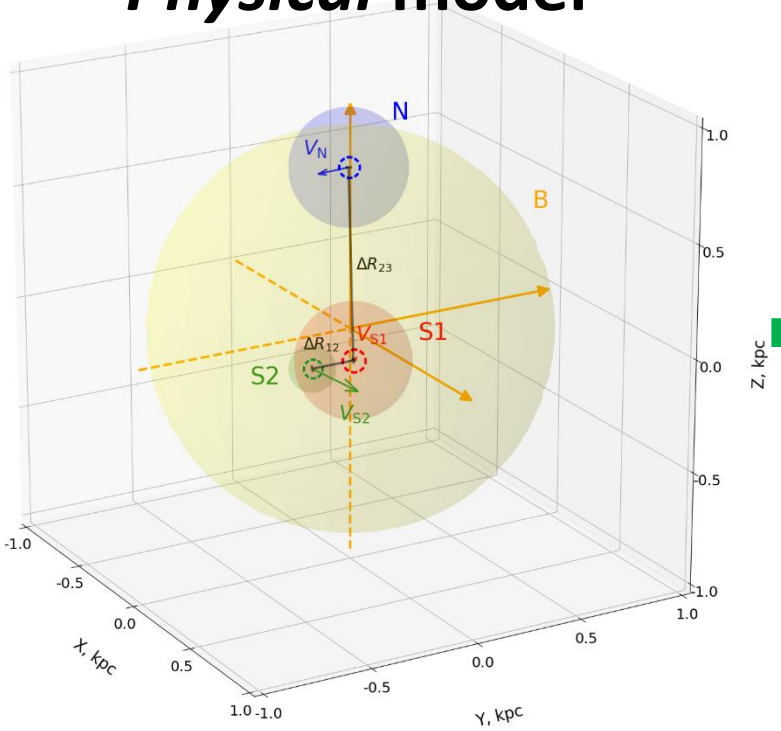

Numerical models

N, number of particles	Randomisation
67.5k	rnd1, 2, 3, 4, 5
135k	rnd1, 2, 3, 4, 5
270k	rnd1, 2, 3, 4, 5
540k	rnd1, 2, 3, 4, 5

4 variants x 5 randomization = **20 *numerical* models**

† ftp://ftp.mao.kiev.ua/pub/berczik/phi-GPU/

540k models – evolution of separation ΔR_{BH}

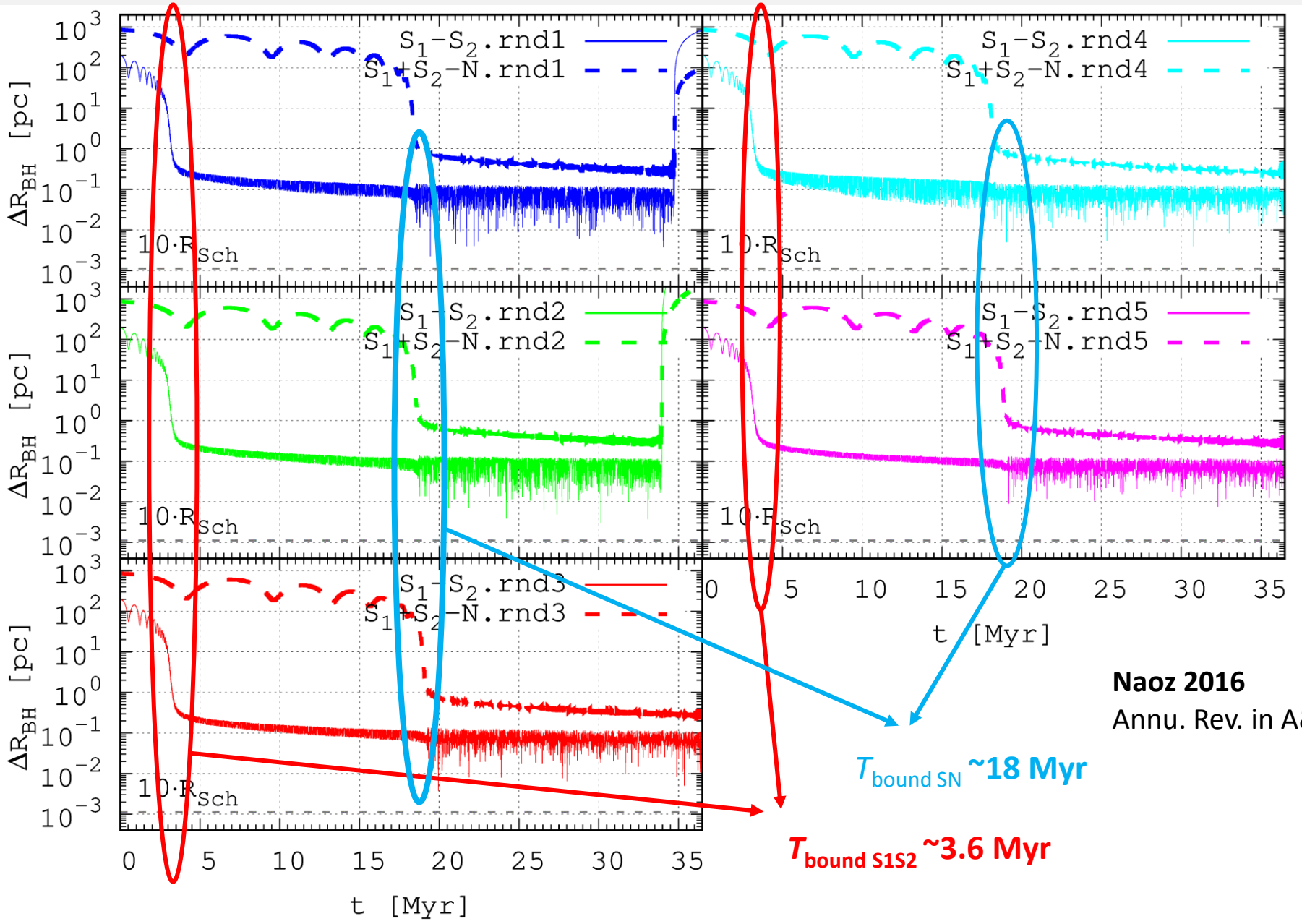

Naoz 2016
Annu. Rev. in A&A

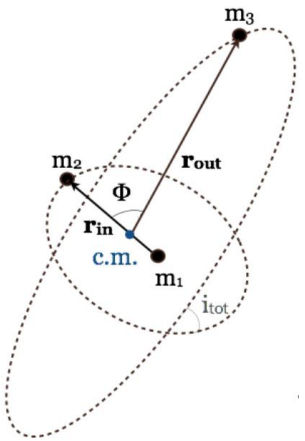

540k models – evolution of eccentricity *e*

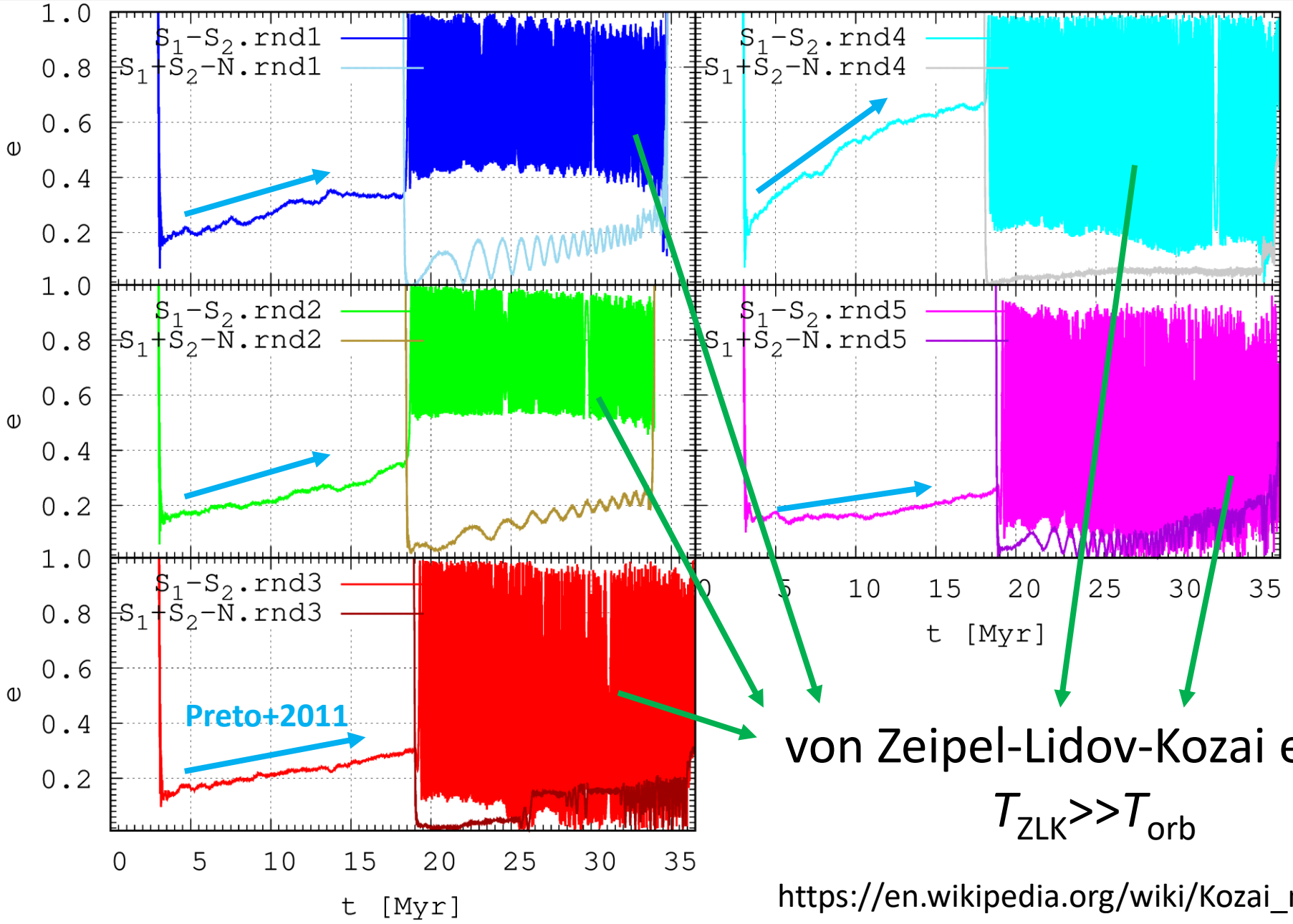

von Zeipel-Lidov-Kozai effect

$T_{ZLK} >> T_{orb}$

https://en.wikipedia.org/wiki/Kozai_mechanism

540k model – details at 18 Myr and 22 Myr

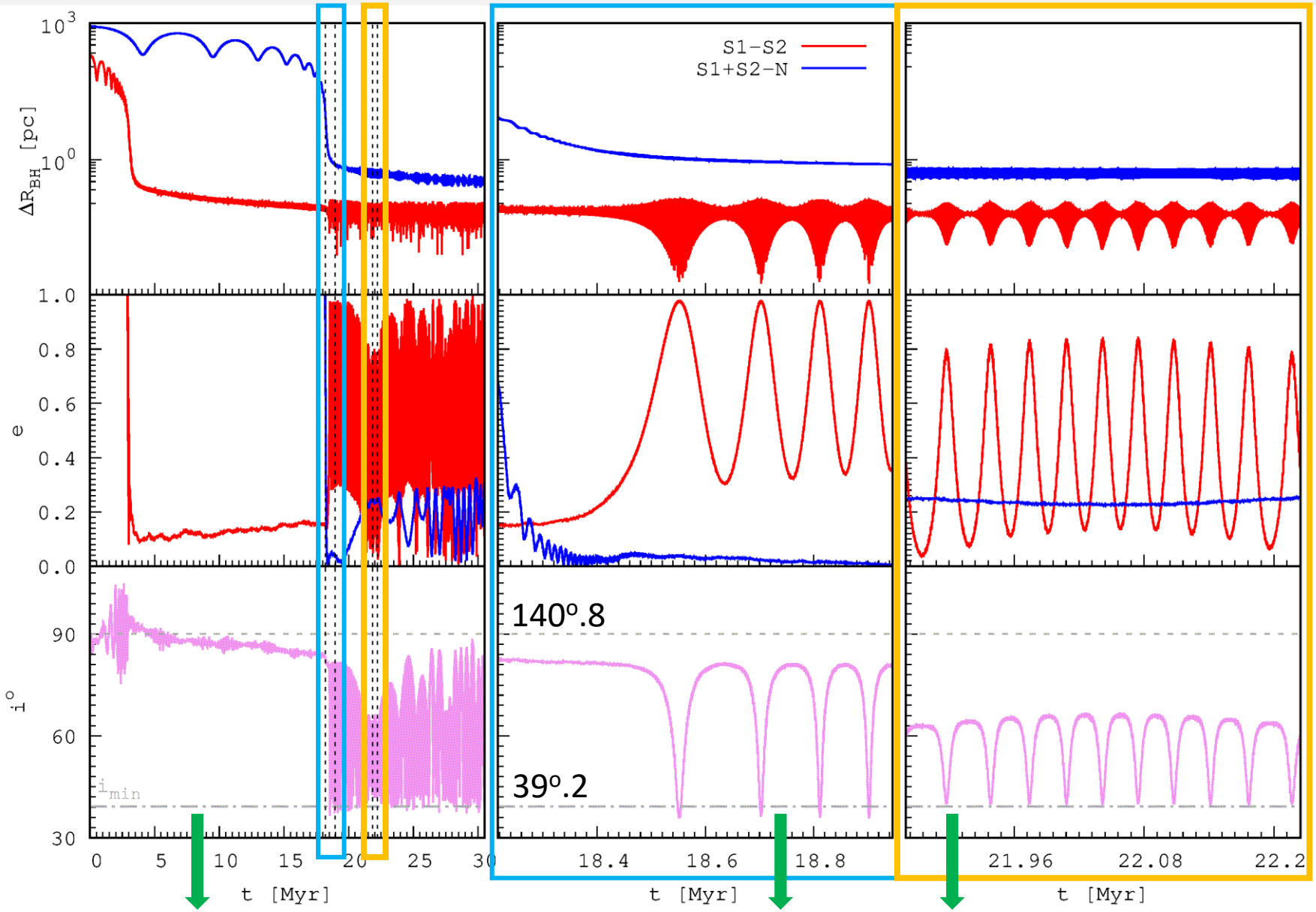

$\Delta t_{snap} \approx 46\,000$ yr

$\Delta t_{snap} \approx 5.6$ yr

Visualization of NGC 6240 evolution

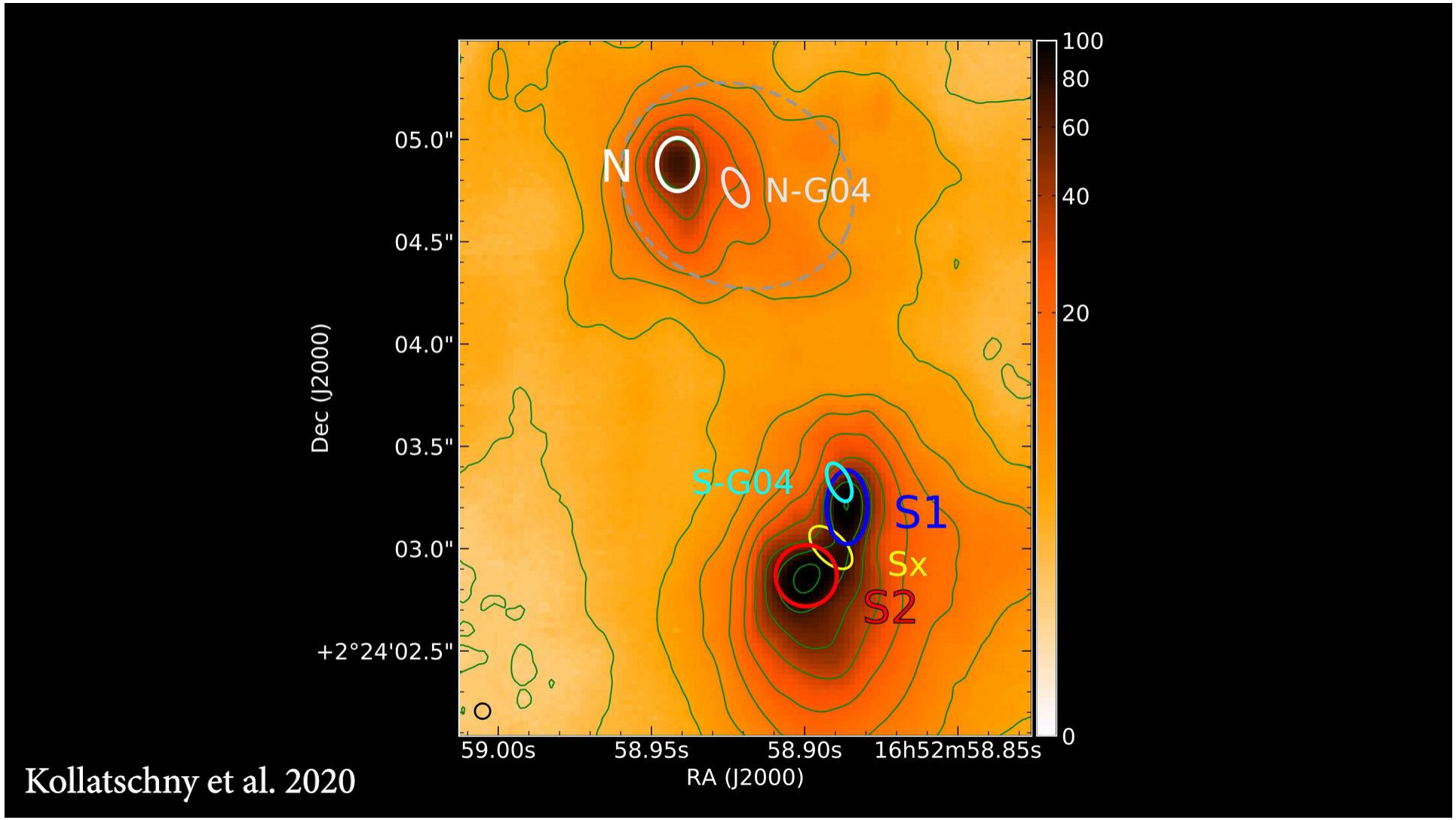

Permanent link to the video https://youtu.be/Jy919R6f61g

Dynamical model of an obscuring clumpy torus in AGNs – I. Velocity and velocity dispersion maps for interpretation of ALMA observations

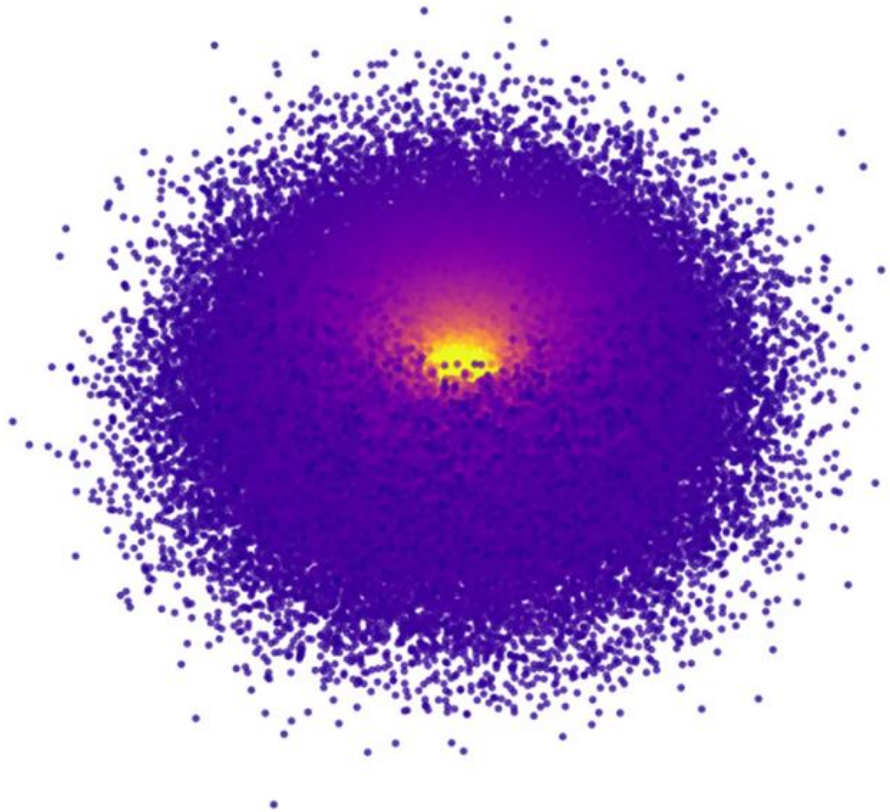

Figure 5. The result of the N-body simulation for $N = 128k$: 3D distribution of clouds after 1000 periods. The colour of clouds is chosen corresponding to $1/r$, where r is the distance from the SMBH.

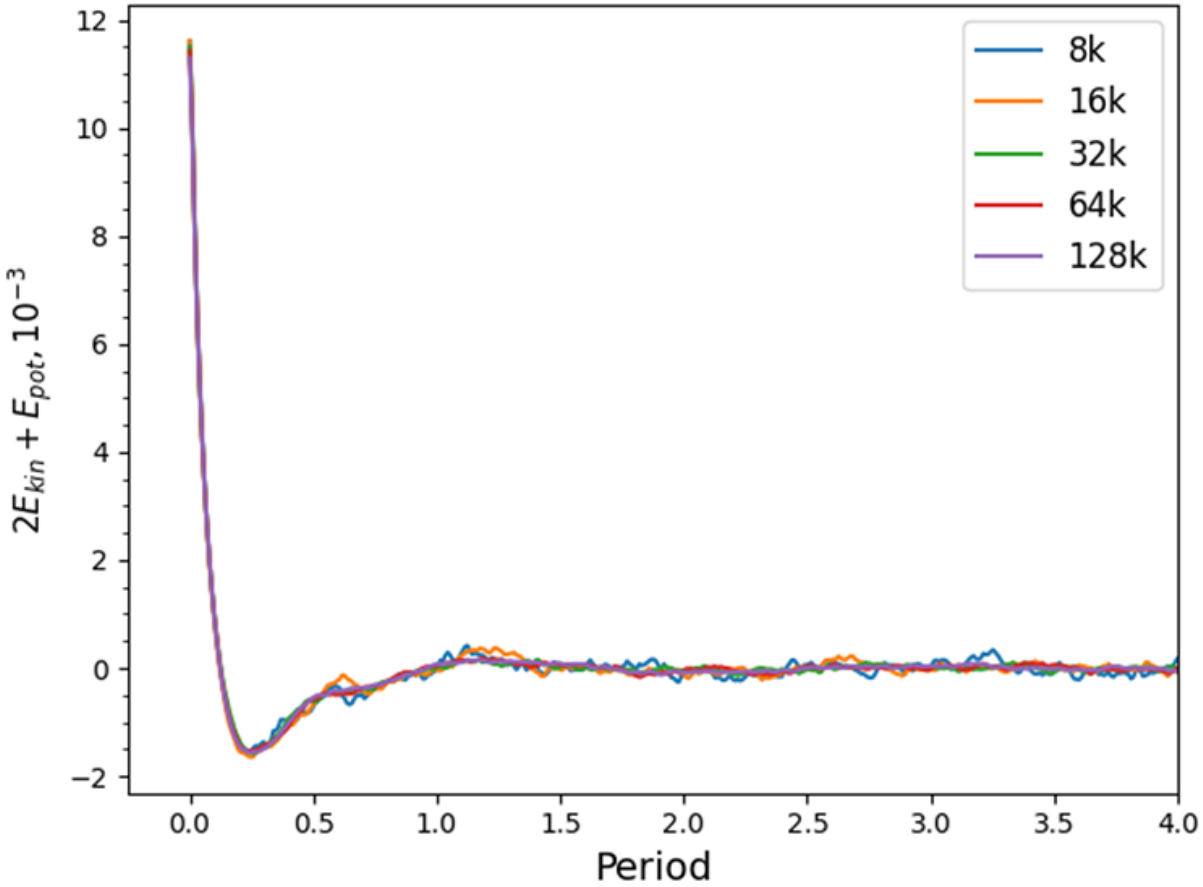

Figure 3. Change of the virial parameter ($2E_{\rm kin} + E_{\rm pot}$) during the first 4 periods.

Dynamical model of an obscuring clumpy torus in AGNs – I. Velocity and velocity dispersion maps for interpretation of ALMA observations

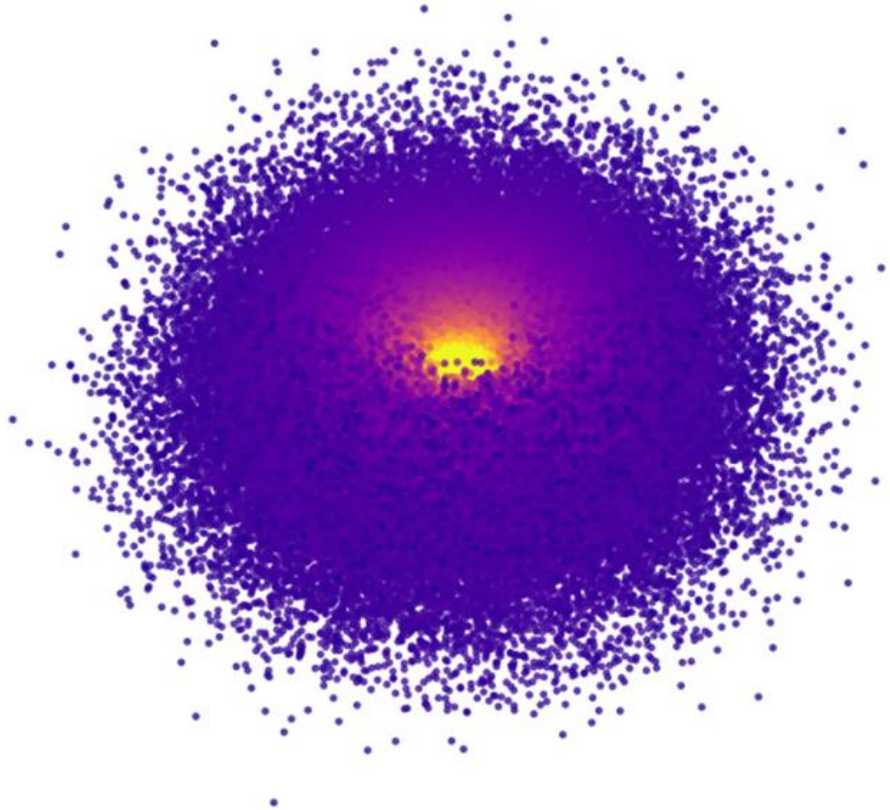

Figure 5. The result of the N-body simulation for $N = 128k$: 3D distribution of clouds after 1000 periods. The colour of clouds is chosen corresponding to $1/r$, where r is the distance from the SMBH.

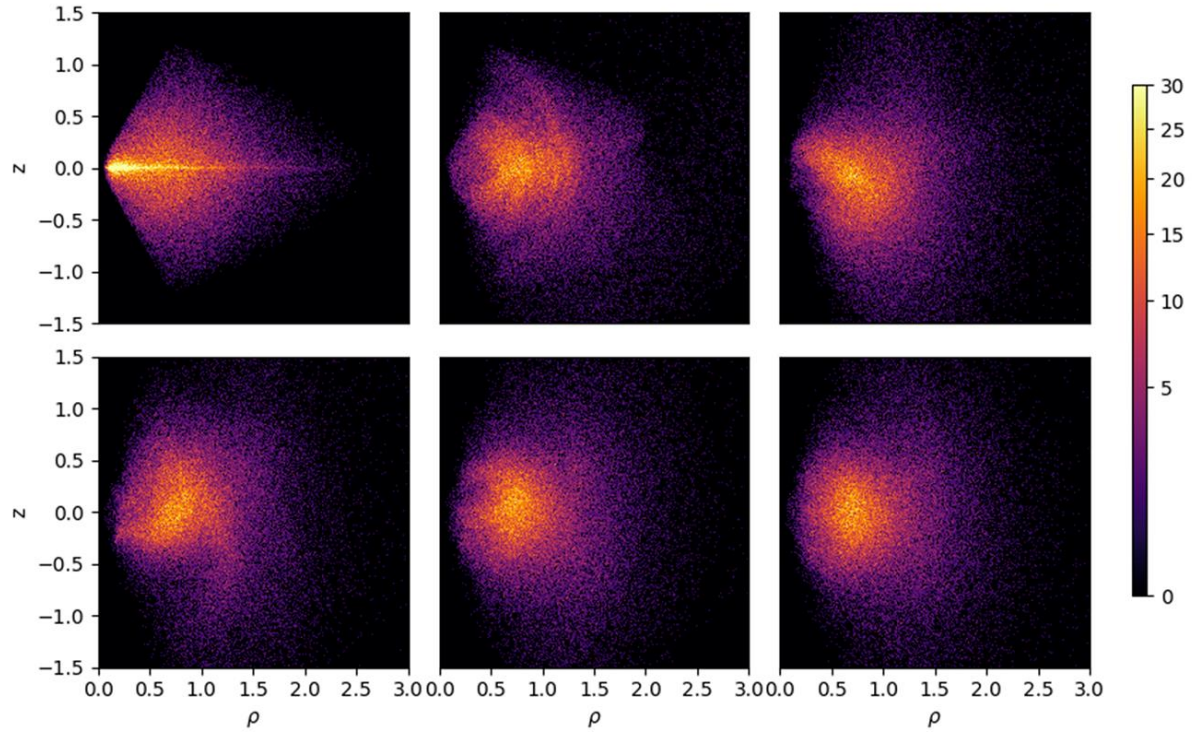

Figure 6. Density plots of the particles projected on to a meridian co-moving plane for $N = 128$k on $t = 0$, 2, 48, 115, 320, and 1000 periods with a scale that indicates the number density of the clouds per a cell, where the scale is normalized to square root. The SMBH is at (0,0).

Dynamical model of an obscuring clumpy torus in AGNs – I. Velocity and velocity dispersion maps for interpretation of ALMA observations

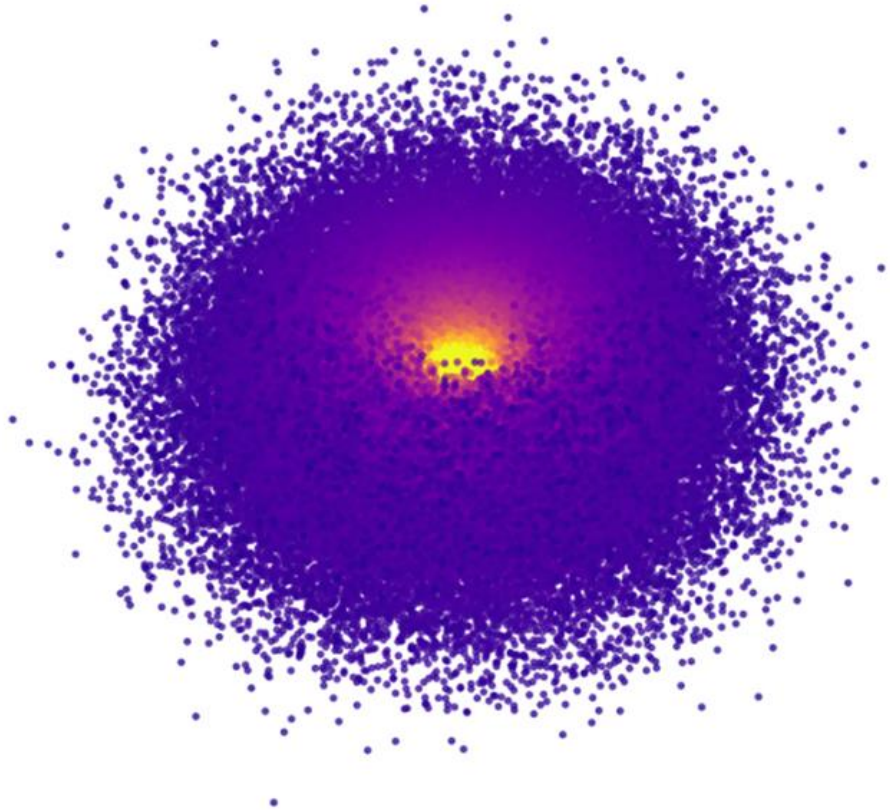

Figure 5. The result of the N-body simulation for $N = 128k$: 3D distribution of clouds after 1000 periods. The colour of clouds is chosen corresponding to $1/r$, where r is the distance from the SMBH.

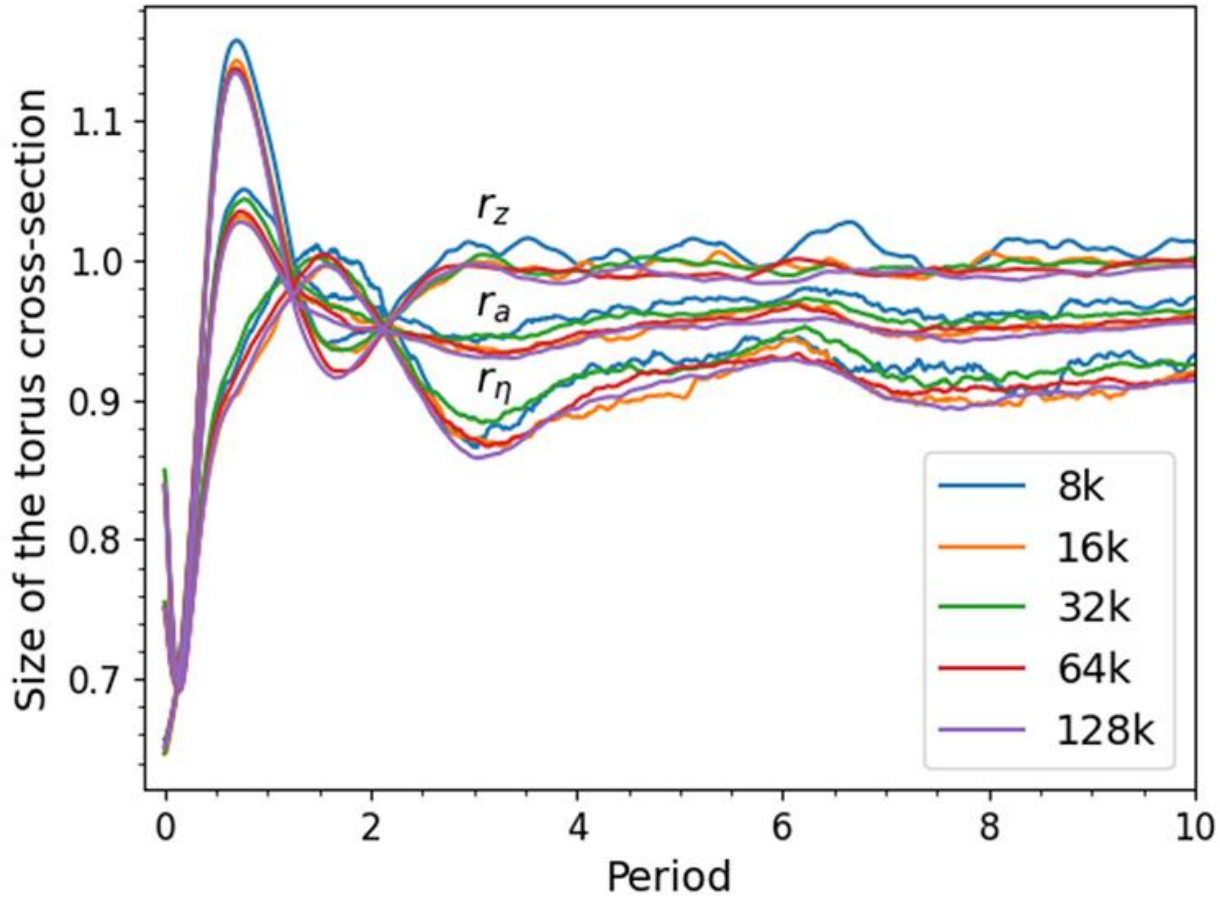

Figure 4. Evolution of the torus cross-section sizes during the first 10 periods.

Dynamical model of an obscuring clumpy torus in AGNs – I. Velocity and velocity dispersion maps for interpretation of ALMA observations

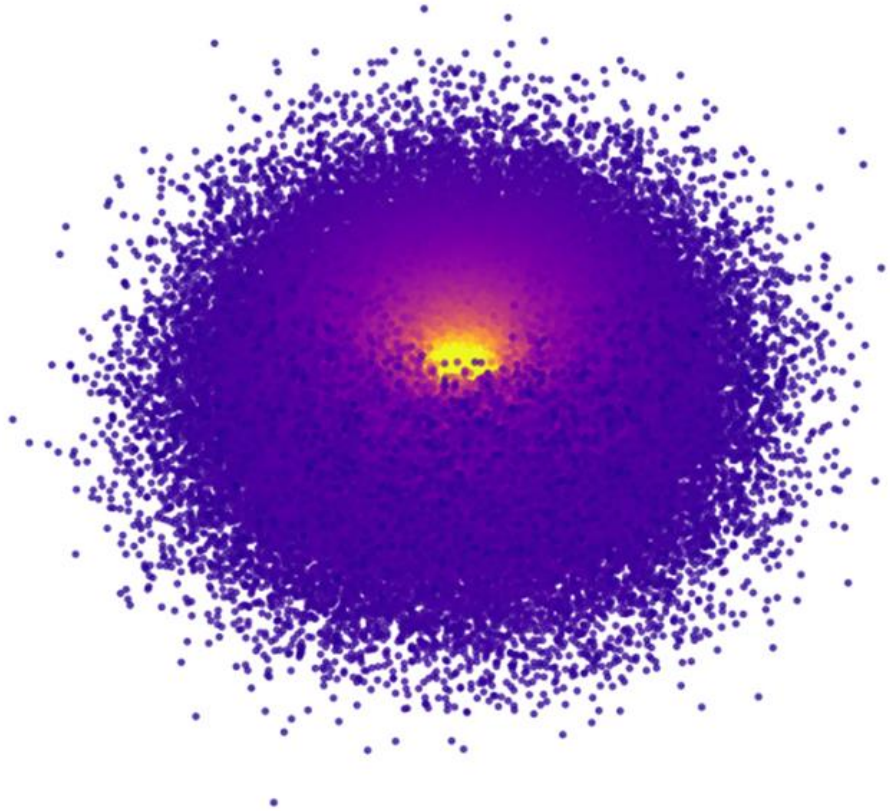

Figure 5. The result of the N-body simulation for $N = 128k$: 3D distribution of clouds after 1000 periods. The colour of clouds is chosen corresponding to $1/r$, where r is the distance from the SMBH.

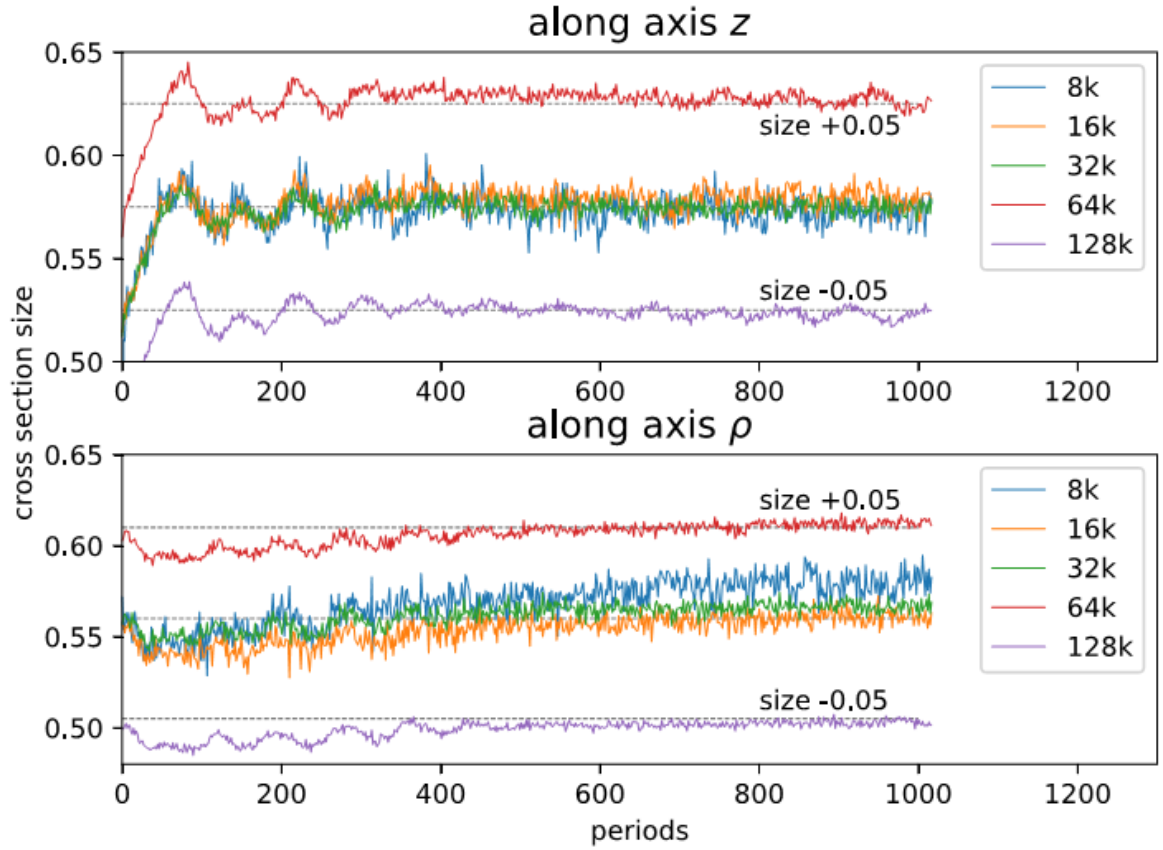

Figure 8. Evolution of the torus cross-section sizes over 1000 periods for 5 cases of particles numbers. For convenience, the trend of the cross-section sizes has been shifted by $+0.05$ units for $N = 64$k and by -0.05 units for $N = 128$k.

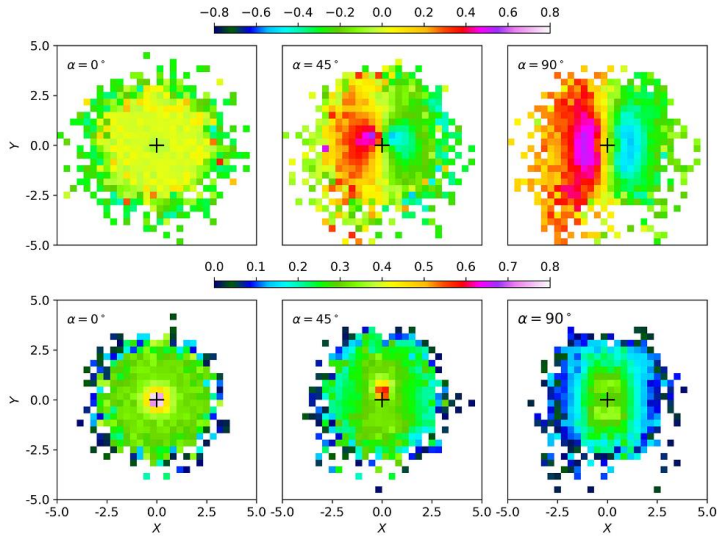

Figure 11. Line-of-sight velocity (*top*) and dispersion maps (*bottom*) of a clumpy torus for $N = 128$k clouds on $t = 1000$ periods with different inclination angles $\alpha = 0°$ (*left*), $\alpha = 45°$ (*middle*), and $\alpha = 90°$ (*right*) for a single relative cloud radius $\varepsilon_{\rm cl} = 0.01$ and an initial half-opening angle of the wind $\theta = 30°$.

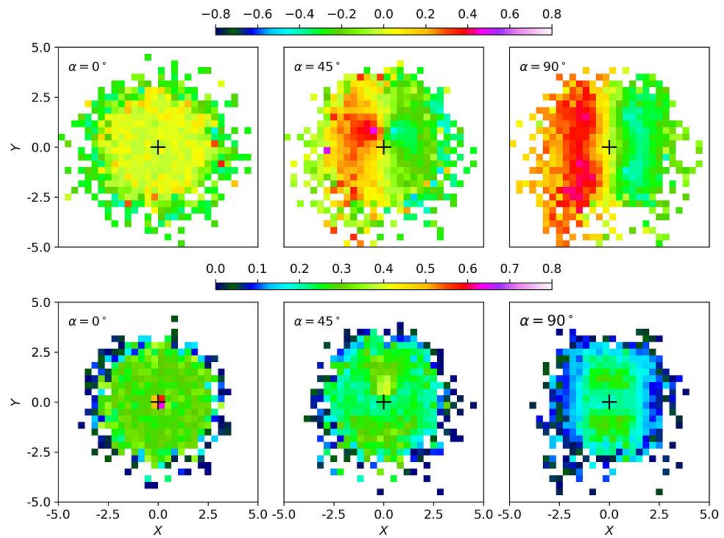

Figure 12. Same as Fig. 11 but for a single cloud radius $\varepsilon_{\rm cl} = 0.025$.

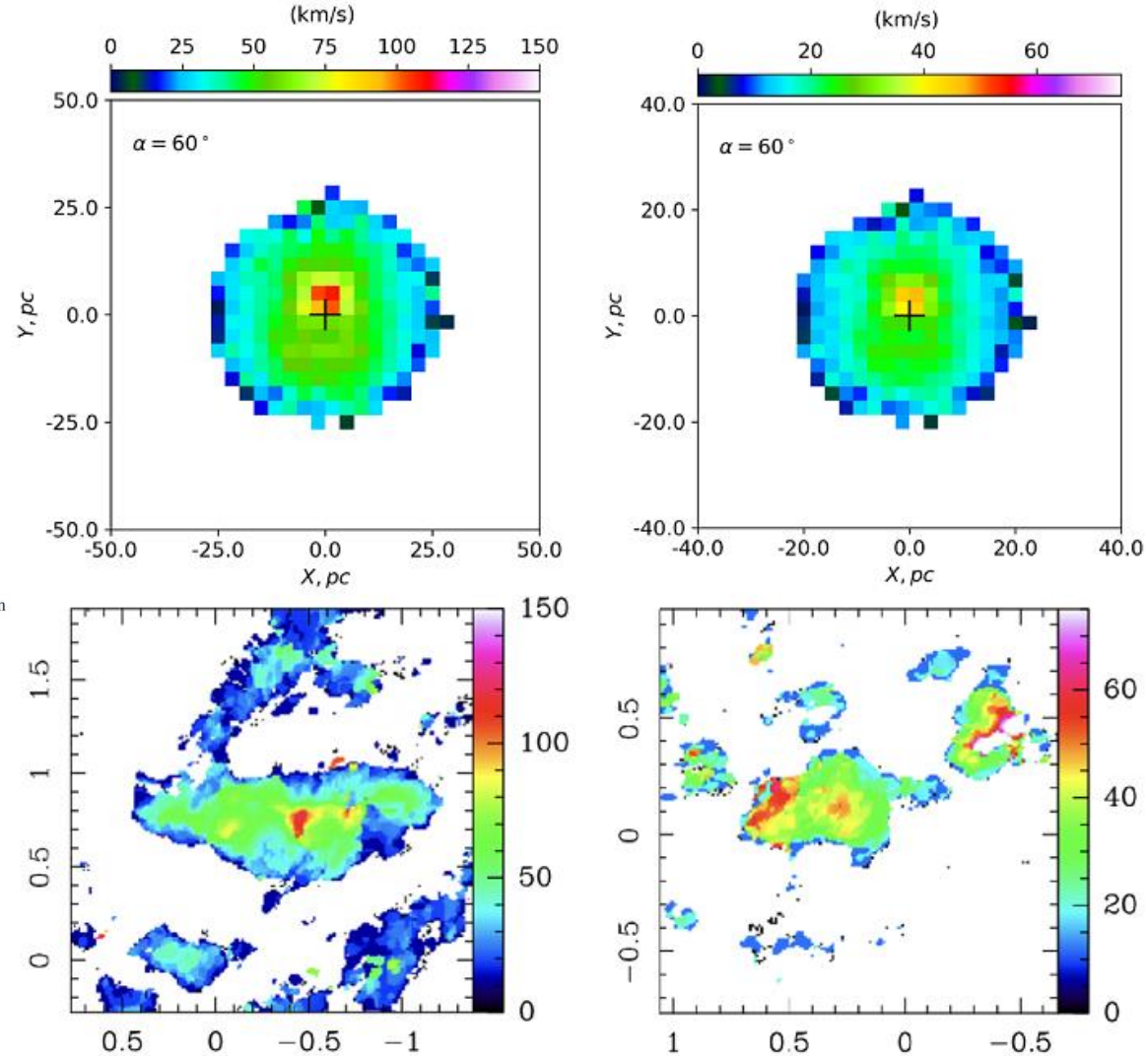

Figure 15. Our model velocity dispersion maps (*top*) and ALMA observational maps (*bottom*) of NGC 1672 (*left*) and NGC 1326 (*right*) in CO(3−2) line from Combes et al. (2019) with velocity dispersion scales in km s^{-1}, angular offsets in arcsec with respect to the phase centre.

Thank you for your attention…
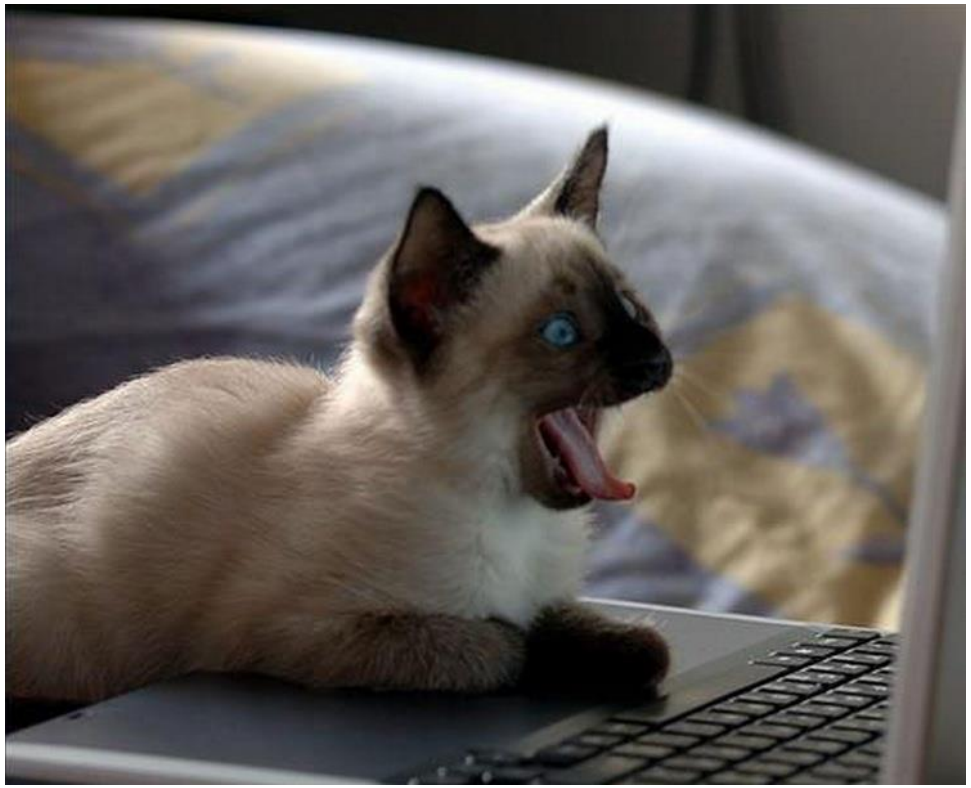
☺